

Biologically-inspired selective filters

by

Laura K. Maguire

B.S., Harvey Mudd College, 2013

A thesis submitted to the
Faculty of the Graduate School of the
University of Colorado in partial fulfillment
of the requirements for the degree of
Doctor of Philosophy
Department of Physics
2019

This thesis entitled:
Biologically-inspired selective filters
written by Laura K. Maguire
has been approved for the Department of Physics

Assistant Professor Loren Hough

Professor Meredith Betterton

Date _____

The final copy of this thesis has been examined by the signatories, and we find that both the content and the form meet acceptable presentation standards of scholarly work in the above mentioned discipline.

Maguire, Laura K. (Ph.D., Physics)

Biologically-inspired selective filters

Thesis directed by Assistant Professor Loren Hough

Placeholder text for abstract.

Contents

Chapter

1	Introduction	1
1.1	The nuclear pore complex is a unique selective filter	1
1.1.1	Intrinsically disordered proteins	2
1.1.2	Basics of nuclear transport	3
1.1.3	Models of nuclear transport	7
1.1.4	Artificial nuclear pore mimics	10
1.2	Other selective biofilters	10
1.2.1	Drug delivery through mucus barriers	11
1.2.2	Diffusion of DNA-binding proteins in the nucleus	13
1.2.3	Subcompartments in liquid droplets	14
1.3	Project goals and motivation	16
1.3.1	Model selective transport as simply as possible	16
1.3.2	Experimentally test bound-state diffusion in biomaterials	18
1.4	Biophysics is beautiful	20
2	Modeling bound-state diffusion in selective filters	22
2.1	Simplified model of nuclear transport	23
2.1.1	Linear appoximation and analytic solution	25
2.1.2	Effect of bound-state diffusion constant	26

2.1.3	Bound diffusion in the linear model	29
2.2	Mechanisms of bound transport factor mobility	32
2.3	Bound mobility through tethered diffusion	32
2.4	Bound mobility through inter-chain hopping	35
2.4.1	Diffusion in a potential well	37
2.4.2	Hopping probability	37
2.4.3	Mean-squared displacement and diffusion coefficient calculation	38
2.4.4	Bound diffusion and selectivity from hopping simulation	38
2.5	Fickian and anomalous diffusion	39
2.6	Bound diffusion in other biological systems	42
2.6.1	DNA damage repair protein recruitment in the nucleus	43
2.7	Conclusions	46
3	Hydrogel design for protein separation	47
3.1	Hydrogel fabrication	48
3.2	Flow chamber fabrication	53
3.3	Hydrogel geometries	57
3.4	FG Nup peptides	59
3.4.1	SSSG negative control	61
3.5	Transport factor constructs	62
3.5.1	Covalently-tethered NTF2 dimer	63
3.5.2	NTF2-GFP	64
3.5.3	Non-binding NTF2 F5R	64
3.5.4	Kap121 and NLS-GFP	66
3.6	Pore size	67
3.7	Porogens	69
3.7.1	Alginate nanospheres	71

3.7.2	Dextran/dextranase porogen system	73
3.8	Polymerization using confocal microscope	76
3.9	Dye-labeling and free dye	82
4	Bound diffusion measurements	86
4.1	Experimental parameters	87
4.1.1	Nup contour length and valency	87
4.1.2	Binding affinity of NTF2 and FSFG	87
4.1.3	Quantifying concentration of tethered Nups	89
4.1.4	Free diffusion constant	90
4.2	Experimental procedures	90
4.2.1	Hydrogel preparation	91
4.2.2	Influx of transport factor and inert protein	91
4.2.3	Fluorescence recovery after photobleaching	92
4.3	Steady-state hydrogel properties	94
4.3.1	Gel dimension estimates	94
4.3.2	Partition coefficients and fraction of time spent bound	96
4.3.3	Bound-diffusion calculation	97
4.4	Influx analysis	98
4.4.1	Profile analysis	100
4.4.2	Accumulation analysis	102
4.5	FRAP analysis	103
4.5.1	Accounting for photobleaching	103
4.5.2	No-exchange solution to diffusion equation	103
4.5.3	Fourier transform solution to diffusion equation	104
4.6	Results	112
4.7	Discussion	113

5	FG Nup aggregation under crowded conditions	116
5.1	Fluorescence time courses	117
5.1.1	Methods	117
5.1.2	Results	121
5.1.3	Discussion	126
5.2	NMR relaxation measurements	126
5.2.1	Methods	126
5.2.2	Results	126
5.2.3	Discussion	126
5.3	Fluorescence spectra	126
5.3.1	Methods	126
5.3.2	Results	127
5.3.3	Discussion	130
5.4	Conclusions	130
Bibliography		131
Appendix		
A	Predicted selectivity of nuclear pore mimics	143
B	Protein expression and purification	144
B.1	Purification of his-tagged protein with metal affinity column	144
B.2	Periplasmic matrix removal (PPMR)	147
B.3	Lyophilization	148
C	Calculation of PEG hydrogel pore size	149

D	Bis-labeling Nup fragments for incorporation into acrylamide hydrogels	151
D.1	Bis-labeling reaction protocol	151
D.2	Ellman's reagent assay protocol	152
E	Hydrogel precursor solutions	154
E.1	PEG hydrogel precursor recipes	154
E.2	Acrylamide hydrogel precursor recipes	155
F	Protein and peptide sequences	157
G	Dye-labeling protocols	161
G.1	Labeling NTF2 with fluorescein-NHS	161
G.2	Labeling NTF2 with Alexa Fluor 488 - SDP or FSFG with Alexa Fluor 647 - SDP .	162
G.3	Labeling NTF2-cys with Alexa Fluor 488 - maleimide	163
H	Hydrogel nuclear pore mimic dataset	165
I	FG124 aggregation condition p-values	168

Tables

Table

2.1	Comparison between flux measurements and model predictions.	29
5.1	Aggregation rate p-values for all crowding agents.	123
5.2	Lag time p-values for all crowding agents.	123
5.3	Aggregation rate p-values for PEG.	123
5.4	Lag time p-values for PEG.	123
5.5	Aggregation rate p-values for PVP.	123
5.6	Lag time p-values for PVP.	125
5.7	FG124 aggregation lifetime and lag time with varying pH. Each condition run with 6 replicates in PTB buffer. One-way ANOVAs show no statistically significant differences between conditions. Standard errors are shown.	125
A.1	Predicted selectivity of FG Nup hydrogels in previous work.	143
E.1	PEG hydrogel precursor stocks.	154
E.2	PEG hydrogel recipes.	155
E.3	Acrylamide hydrogel precursor stocks.	155
E.4	Acrylamide hydrogel recipes.	155
E.5	APS/TEMED crosslinking times.	156
F.1	FG Nup sequences	158

F.2	FG Nup sequences, continued.	159
F.3	Other sequences.	160
I.1	Aggregation rate p-values for all crowding agents.	168
I.2	Lag time p-values for all crowding agents.	168
I.3	Aggregation rate p-values for PEG.	168
I.4	Lag time p-values for PEG.	169
I.5	Aggregation rate p-values for PVP.	169
I.6	Lag time p-values for PVP.	169

Figures

Figure

1.1	Nuclear pore complex and FG Nups.	4
1.2	Two important models of nuclear transport.	8
1.3	Effective potential model of nuclear transport.	9
1.4	Nanoparticle drug delivery through a mucus barrier.	12
1.5	Phase-separated subcompartments of the nucleolus.	15
2.1	Schematics of the nuclear-pore complex and model.	24
2.2	Flux and selectivity as a function of bound mobility.	27
2.3	Selectivity in the linear approximation.	30
2.4	Dependence of selectivity on model parameters.	30
2.5	Dependence of absolute flux on model parameters.	31
2.6	Selectivity from tethered diffusion.	34
2.7	Nup contour length and concentration comparison.	35
2.8	Selectivity from inter-chain hopping.	36
2.9	Mean-squared displacement in the hopping simulation.	39
2.10	Effect of Nup contour length and hopping rate on selectivity.	40
2.11	Anomalous diffusion in the hopping simulation.	41
2.12	Bound diffusion in other systems.	42
2.13	Possible bound-diffusion mechanisms of PARP1.	44

3.1	Hydrogels for protein separation.	49
3.2	Monomers and crosslinkers for PEG and acrylamide hydrogels.	51
3.3	Photoinitiator properties.	52
3.4	Photopolymerization with and without photomasks.	54
3.5	Flow chamber design and geometries.	54
3.6	Microfluidic sticker fabrication.	56
3.7	Nup fragments used in nuclear pore mimic experiments.	60
3.8	SSSG as a nonbinding Nup.	62
3.9	NTF2 fusion proteins.	65
3.10	Kap121 and GFP-NLS cargo.	66
3.11	Partition coefficient as a function of molecular weight.	69
3.12	Alginate nanospheres as porogens.	70
3.13	Equilibration of hydrogels after digestion of dextran porogen.	74
3.14	Dextranase degradation of FSFG.	74
3.15	Protein accumulation within dextran/dextranase hyrogels.	75
3.16	Laser-written hydrogels.	77
3.17	Influx plots for confocal-crosslinked hydrogel ring.	78
3.18	NTF2 binding to confocal-crosslinked FSFG hydrogels.	79
3.19	Effect of dwell time and loop number on confocal-crosslinked hydrogels.	80
3.20	Quantifying free dye concentration.	83
3.21	Comparison of single and double exponential fits for free-dye analysis.	84
4.1	Isothermal titration calorimetry with NTF2 and FSFG.	88
4.2	Influx experiments images.	93
4.3	FRAP image series.	95
4.4	Hydrogel masks with radius and center calculations.	95
4.5	Partitioning of NTF2 and mCherry into FSFG hydrogel.	96

4.6	Intensity profiles and accumulation curve from influx experiments.	98
4.7	Geometry of profile and accumulation model.	99
4.8	Fits to concentration profiles at a fixed time.	101
4.9	Fits to concentration profiles at a fixed position.	101
4.10	Fits to accumulation curves.	102
4.11	Geometry for Fourier transform solution.	105
4.12	Reconstruction of initial concentration distribution.	110
4.13	Heatmap of mode coefficients.	110
4.14	Fits to recovery curves using Fourier transform solution.	111
4.15	Bright NTF2-F ring surrounding photobleach spot.	112
4.16	Partition coefficients and fraction of NTF2 bound.	113
4.17	Recovery curves.	114
4.18	Observed diffusion constants and NTF2 bound diffusion.	114
5.1	Sample sigmoid fit to FG124 sample with 13% w/v PEG. Burst phase and stationary phase are shown; lag phase took place before data collection began. Fit is to Eqn. 5.1.	118
5.2	(A) Aggregation lifetimes and (B) lag times for all crowding agents, normalized to the no-crowding condition. Crowder concentrations were 19% w/v serine, 13% PEG, 13% PVP, and 10 mg/mL cell lysate (lookup:check this). Error bars are standard error of the mean.	122
5.3	test	124
5.4	Emission scan of fresh and aggregated FG124 in crowded conditions. Data normalized by subtracting blank sample.	127
5.5	Emission scan of phenylalanine, FSFG, and FG124. Excited at 240 nm. Phe data is not mine, need to check reference. Data normalized to a maximum amplitude of 1. .	128
5.6	Emission scan of phenylalanine, FSFG, and FG124. Excited at 240 nm. Phe data is not mine, need to check reference. Data normalized to a maximum amplitude of 1. .	128

5.7 Absorbance of 5% PEG and PVP solutions in PTB. Normalized by subtracting PTB absorbance.	129
B.1 Buffers for metal affinity column purifications.	145
H.1 Parameters for predicted bound diffusion.	165
H.2 No-Nup hydrogel dataset.	166
H.3 FSFG concat-1 hydrogel dataset.	166
H.4 FSFG concat-2 hydrogel dataset.	167

Chapter 1

Introduction

Selective biofilters are found in all manner of living systems and control the motion of proteins, nucleic acids, and other macromolecules. While many operate by size exclusion, permitting only the passage of particles below a size cutoff, more sophisticated filters make use of binding interactions. Of particular interest are filters which require rapid motion or high flux of proteins that must still bind targets with high specificity. The two requirements would seem to be in direct competition, yet there are many examples of these systems. In this work, we investigate the mechanisms by which such filters function through both modeling and experiment, using the nuclear pore, a canonical example of selective transport, as inspiration.

1.1 The nuclear pore complex is a unique selective filter

The nuclear pore complex (NPC) is the filter that regulates all transport between the cell's nucleus and its cytoplasm (Fig. 1.1). Its unusual selective properties are apparent as it prevents significant flux of macromolecules larger than about 30 kDa (~ 5 nm) [1]. However, a class of proteins known as transport factors carry cargo molecules quite rapidly across the pore, although the complex of transport factor and cargo can be up to 40 nm in size. Far from being a typical size-exclusion filter, therefore, the nuclear pore complex is a highly specific selective barrier which the cell uses to tightly control passage in and out of the nucleus. While the important biochemical components of nuclear transport have been identified, the mechanism of selectivity is still not well

understood. Even though the precise mechanism is under debate, it is clear that the NPC is a fascinating example of the cell leveraging intrinsically disordered proteins to accomplish a unique task.

1.1.1 Intrinsically disordered proteins

It has been long-standing conventional wisdom among biologists that a protein’s folded shape determined its function. Most enzymes and other proteins that were studied had a stable folded configuration, the lowest point on a well-defined folding energy landscape. A protein’s conformation provided specific docking points through which it could interact with ligands or other proteins in a “lock-and-key” model.

However, a few decades ago, it began to become clear that not all proteins have a well-defined ternary or even secondary structure, but rather exist as extended polymer chains. These intrinsically disordered proteins (IDPs) were initially dismissed as nonfunctional, but evidence began to accumulate that they were in fact essential for cellular function, overturning the structure-function paradigm. Their roles and importance are still being understood, as are the unusual mechanisms by which they accomplish their functions without a well-defined structure.

Today, it is estimated that 30% of eukaryotic proteins are disordered or contain significant disordered regions [2]. While there is significant sequence heterogeneity among IDPs, they tend to contain a large proportion of hydrophilic residues, and often have long stretches of low-complexity regions where only a few amino acids are represented. They also often have high net charge.

Some IDPs fold (or partially fold) upon binding with an ordered partner, while others form “fuzzy” complex that remains disordered. Their advantages over folded proteins may include their plasticity, which enables them to bind many different binding partners. Multivalency, either as one-to-many or many-to-one binding, may also play a role. They may act as hubs that bring together larger complexes. Similarly, IDPs are often known for having high specificity at relatively weak binding strengths [3, 4].

While the normal functioning of IDPs is very important to the cell, IDPs are also prone to

aggregation and are at the root of pathologies such as Alzheimer’s disease, Parkinsons, and prion diseases [5]. Often, normally-disordered proteins aggregate into amyloid fibrils, a stable structure based on parallel beta-sheets.

IDPs are commonly involved in cell signaling and regulation [3]. Their disordered nature makes them useful as hubs that bring together many other proteins, and as scaffolds that many proteins can bind to at once. IDPs appear to be prevalent in transcriptional regulation, and they are playing increasingly apparent roles in liquid-liquid phase separation within cells [6]. One of the most fascinating examples of IDP function is in the nuclear pore complex (NPC), a unique selective barrier that regulates all transport between the nucleus and the cytoplasm. The link between disorder and selectivity is not well understood in this case.

1.1.2 Basics of nuclear transport

The nuclear pore complex (NPC) resides in the nuclear envelope of eukaryotes and regulates all macromolecular traffic between the nucleus and cytoplasm (Fig. 1.1). The NPC is one of the largest protein complexes in the cell, at about 60 MDa in yeast and 120 MDa in humans [7]. As the regulator of nucleocytoplasmic transport, the NPC must rapidly and specifically allow a wide array of macromolecules to pass: transcription factors into the nucleus, and RNA into the cytoplasm. It must also be robust to problems and able to accomodate mechanical strain as the nuclear envelope changes shape, as well as accomodating large cargo. These functions are accomplished through a structure with two main parts, both made of proteins known as nucleoporins, or Nups: the scaffold Nups, which form a ringlike complex, and the FG Nups, which are disordered and fill the central channel created by the scaffold Nups (Fig. 1.1).

The nuclear pore itself is formed of scaffold Nups, which are ordered proteins that form ringlike complexes with eightfold symmetry [7, 9]. The central channel of the pore is filled with disordered FG Nups. FG Nups typically consist of an ordered domain that anchors them to the wall of the channel, and an entirely disordered domain that extends into the channel. As with all Nups, FG Nups have eightfold symmetry in the pore, and some of them are present in much

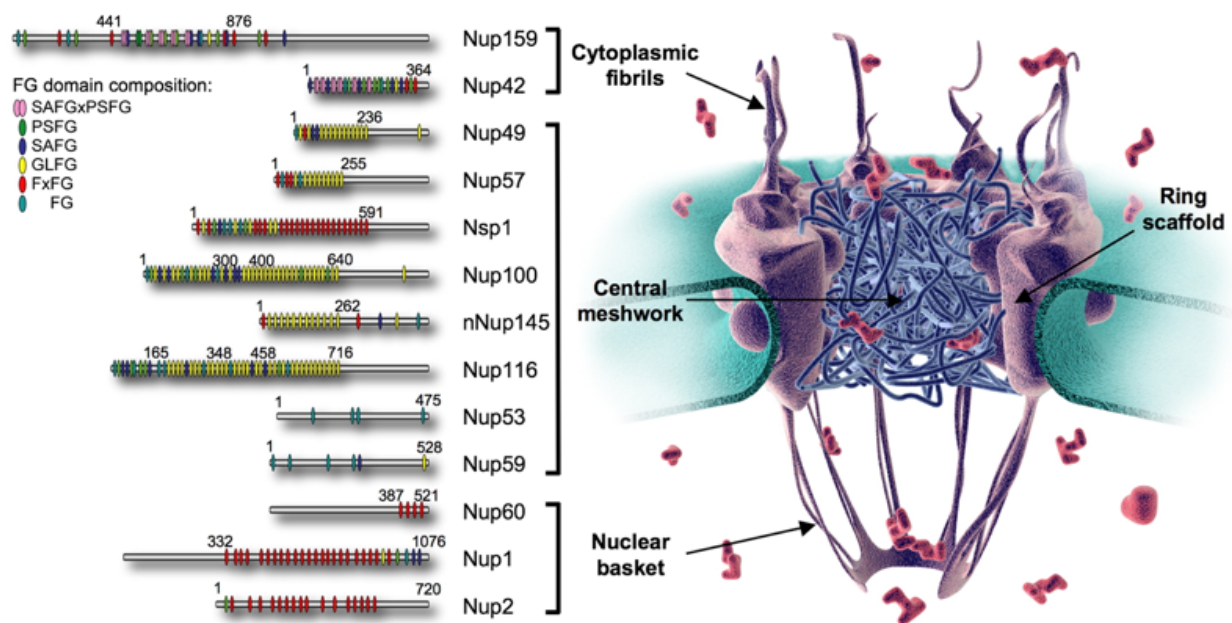


Figure 1.1: Nuclear pore complex and FG Nups. The cartoon shows the role of the FG Nups filling the central channel. The left panel shows a schematic of the sequence of important FG Nups and the locations of their FG motifs. Figure adapted from [8].

higher copy number. The disordered portion of every FG Nup contains phenylalanine- glycine (FG) motifs which bind to the hydrophobic binding pockets of transport factors. While there are multiple binding motifs, all are short sequences which incorporate an FG repeat; for instance, FSFG, GLFG, and others. Each FG Nup contains tens of FG repeats, leading to a high density of FG repeats within the pore [9, 10].

Since the FG Nups are disordered, most conventional visualization techniques, such as cryogenic electron microscopy and x-ray crystallography, are ineffective. When imaged over time or when several pores are imaged, the averaged results do not show the disordered portion of the FG Nups. Techniques such as NMR and atomic force microscopy (AFM) can help gain insight into their conformational ensembles, as can some superresolution microscopy techniques, though the time and length scales of transport are often prohibitive for any microscopy [11–13]. Early research suggested that the FG Nups formed a central plug or "transporter", but more recent work suggests that there is no central structure and the central channel is filled instead with highly dynamic disordered proteins [12, 14, 15]. There is some evidence from simulations that the density of the FG Nups, as well as their charge density and hydrophobic properties, are not uniform along either the radial or axial directions [16–18]. This may contribute to selective transport, although the pore still functions without the asymmetric FG Nups [19]. Indeed, the NPC is remarkably robust to FG Nup deletion. Over half of the mass of FG Nups can be removed without eliminating the selectivity barrier [19–22].

Transport factors (TFs) are ordered proteins that carry cargo through the NPC. While there are various types, they share several features in common, most notably the fact that all known transport factors have more than one hydrophobic binding pocket which binds to FG repeats. Binding affinities between TFs and FG Nups are surprisingly difficult to measure accurately. Values of the dissociation constant K_D measured outside of the cellular context are often in the low nanomolar range, implying a binding lifetime which is inconsistent with the experimentally-observed rapid translocation through the nuclear pore [23, 24]. Recent consensus is that binding is much weaker in the cellular environment, with K_D values between hundreds of micromolar and millimolar

[25–27]. The extreme binding multivalency of Nup - transport factor interactions adds a further layer of complexity to interpreting affinity data. It is increasingly accepted that the highly transient and multivalent binding of TFs to FG Nups is key to the combination of high specificity and rapid transport exhibited by the NPC [28].

The karyopherins (Kaps), also known as importins and exportins, are largest family of transport factors. The approximately twenty different Kaps are responsible for most nucleocytoplasmic transport [29]. Kaps typically consist of multiple HEAT repeats, a helical motif which conveys structural flexibility [30]. Most Kaps bind their cargo directly via a nuclear localization signal (NLS, for nuclear import) or nuclear export signal (NES, for nuclear export). NLS and NES are relatively short amino acid tags found on cargo [31]. However, sometimes the adaptor protein importin α is also needed. In general, Kaps are on the order of 100 kDa in size, well above the passive permeability limit [1]. As discussed below, there is evidence that the presence of Kaps contributes to the selectivity barrier [29, 32–34]. Many Kaps must be actively released from the nuclear pore and from their cargo after transit [35, 36].

Unlike the karyopherins, nuclear transport factor 2 (NTF2) does not transport a wide variety of cargo across the NPC. Instead, NFT2 maintains the Ran gradient needed for transport by carrying RanGDP across the pore [37, 38]. NTF2 is a homodimer whose monomers are 14 kDa and contain at least one FG binding site apiece. Although its small size of 28 kDa is near the 30 kDa cutoff for passive transit through the pore, its flux through the pore is still at least 30 times that of similarly-sized proteins that do not bind to FG Nups [39–41]. NTF2 does not require adaptor proteins or active release from the pore. We predominantly use NTF2 as a model transport factor in both the theoretical and experimental work discussed here, because of its simplicity as well as its ease of expression and purification from bacterial cells.

Selective transport requires an energy source, which in the case of the NPC is provided by the Ran cycle. When a TF-cargo complex passes from the cytoplasm into the nucleus, it encounters a RanGTP on the nuclear side which binds to the TF and displaces the cargo, actively releasing it. Then the TF-RanGTP complex can collect a cargo destined for nuclear export, and this ternary

complex can diffuse back through the NPC to the cytoplasm. The protein RanGAP then hydrolyzes the RanGTP to RanGDP, disrupting the complex into its three original pieces. Ultimately, the energy source for selective nuclear transport comes from the RanGTP-RanGDP gradient from the cytoplasm to the nucleus, a gradient which is maintained partially by NTF2, which carries RanGDP through the pore [28, 42]. From the perspective of transport, this means that the process of passing through the pore is itself passive and does not consume energy. The selectivity ultimately arises from concentration gradients maintained by the Ran cycle, but the selective mechanism is not itself active.

One surprising feature of nuclear transport is its sheer speed and volume. The high macromolecular traffic between nucleus and cytoplasm requires high flux through each NPC. Experiments with permeabilized cells estimate that the total molecular flow through the NPC could be as high as 10-20 MDa per pore per second, corresponding to roughly 1000 transport events per pore per second [39]. Experiments focusing particularly on NTF2 report fluxes between 50 and 250 molecules per pore per second [39–41]. Fluxes this high mean a continuously high occupancy of the NPC, estimated at around 100 karyopherins at once [43]. One reason that individual NPCs can accommodate such high flux is the rapidity with which molecules transit the pore. A wide range of transport factors and cargo have a dwell time of less than 10 ms in the pore [13, 44–46]. Typically, this is determined using single-molecule tracking with superresolution microscopy [13].

1.1.3 Models of nuclear transport

While the components of nuclear transport are well-understood, the mechanism behind its unusual selective properties is unclear. Broadly speaking, two of the most important theoretical frameworks are the hydrogel model and the entropic barrier model (Fig. 1.2). Both are supported by some experimental results and challenged by others, and they are not mutually exclusive. Both could contribute to selective transport.

The hydrogel model posits that the FG Nups within the nuclear pore are transiently crosslinked at their FG repeats into a hydrogel-like structure. Inert proteins are prevented from passing through

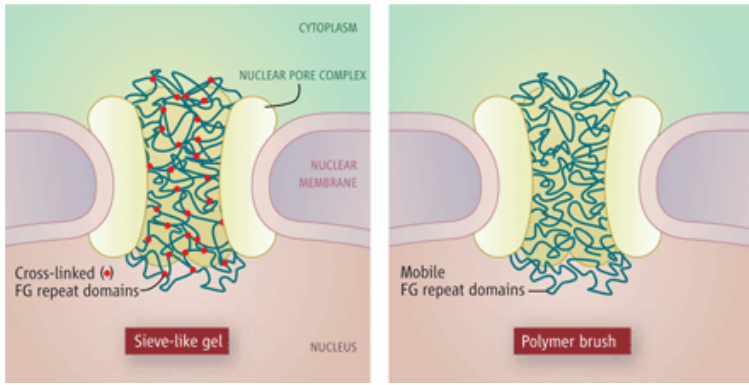


Figure 1.2: The two major models of the nuclear pore: the hydrogel (sieve-like gel) and entropic barrier (polymer brush) models. Figure from [47].

the pore due to the small mesh size, while transport factors carrying cargo can also bind to the FG repeats, disrupting the hydrogel and moving through the pore. This view of the nuclear pore is supported by experiments showing that the disordered domain of the essential FG Nup Nsp1 aggregates into a hydrogel when purified into buffer [48]. These hydrogels show strong selectivity for import of transport factors and their cargo over inert proteins, demonstrating binding between the aggregated FG Nups and the transport factors [49–51]. Theoretical models of diffusion through a transiently-crosslinked hydrogel show selective properties [39, 52, 53]. However, while nuclear pore mimics which consist of aggregated FG Nups display highly selective entry of transport factors, they do not permit the exit of transport factors over timescales consistent with transport [49, 50]. Furthermore, some Nups which aggregate in buffer remain disordered in the cellular environment [11].

Conversely, the entropic barrier model supposes that FG Nups instead act as polymer brushes within the pore. In this view, inert proteins are prevented from entering the pore due to the entropic penalty they would incur by restricting the possible conformations of the Nups. However, the decrease in free energy upon a transport factor binding to a Nup offsets the entropic penalty and allows transports and their cargo to pass [54, 55]. Evidence for this view comes from a number of studies in which single layers of FG Nups are grafted onto a surface and their extension monitored as transport factors are titrated on and off the surface [56–58]. Layer height tends to change non-monotonically as transport factors are added, suggesting that the presence of transport factors affects the selectivity of the nuclear pore.

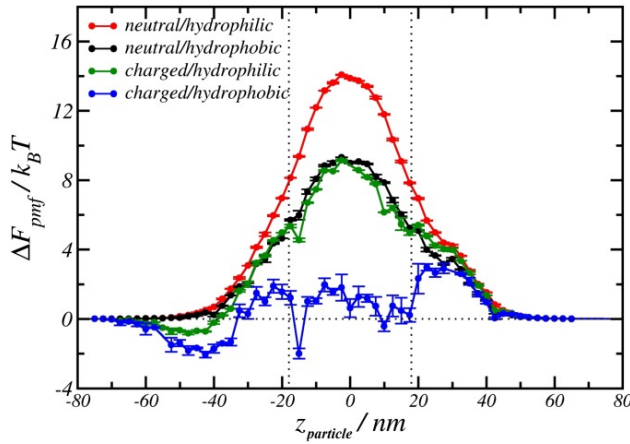


Figure 1.3: Example of effective-potential model of nuclear transport. Figure shows simulated free-energy landscape for a variety of possible transport factors as a function of position within the nuclear pore. Figure from [18].

More generally, FG Nups exist on a continuum of “cohesiveness,” ranging from Nups (or portions of Nups) which do not aggregate under any physiological conditions to ones which do so readily [11]. Nup cohesiveness depends on their charge, length, and hydrophobicity. Many simulations of the nuclear pore aim to understand the role of Nup cohesiveness in transport [18, 53, 59, 60]. There may be distinct regions of differing Nup properties within the nuclear pore. A relatively common method of modeling transport is to computationally reduce the problem to that of a transport factor diffusing in a one-dimensional effective potential representing its interactions with Nups (Fig 1.3) [1, 18, 61, 62]. These models predict selective transport while being highly dependent on the precise details of Nup composition and location within the nuclear pore. These models also do not presuppose that either the hydrogel or entropic brush model is fully correct, but allow for a mixture of cohesive and non-cohesive Nups.

Apart from the question of FG Nup conformation within the nuclear pore, the role of transport factors themselves in the permeability barrier has been under investigation [29, 32–34]. There is evidence that the presence of karyopherins in the nuclear pore increases its selectivity for transport factors, possibly by establishing “tight-binding” and “weak-binding” subpopulations of Kaps which compete for binding sites on the Nups [56]. Even non-specific competition may make the nuclear pore’s selectivity barrier more robust as well [63–66]. The precise role of crowding and competition in nuclear pore selectivity is fascinating but as yet unclear.

Relatively few non-computational, quantitative theories of nuclear transport exist. Reaction-

diffusion models have been proposed with varying degrees of complexity and different underlying assumptions but they do not take both binding kinetics and binding site saturation into account [61, 67].

1.1.4 Artificial nuclear pore mimics

Systems which mimic the selectivity of the nuclear pore have been attempted using a wide range of approaches, with mixed success. Some nuclear pore mimics recreate the nanopore geometry of the NPC [22, 68]. Several others are based on hydrogels, whether hydrogels composed of aggregated FG Nups [49–51] or inert hydrogels with tethered Nups or Nup-derived peptides [67, 69]. An interesting preliminary work demonstrated the use of DNA origami to mimic the scaffold of the nuclear pore, complete with multiple sites for FG Nup attachment [70]. While many of these mimics have shown selectivity to some extent, none have definitively shown a flux of transport factors into, through, and out of the mimic that matches that observed experimentally.

1.2 Other selective biofilters

Selective biofilters exist in many contexts outside of nuclear transport, and they frequently include a common set of elements that are exemplified by the nuclear pore. In particular, cells often need proteins to move rapidly within a cellular compartment but still possess high binding specificity. This is often accomplished with intrinsically disordered proteins that interact transiently and multivalently with their binding partners. In the crowded environment of the cell or extracellular matrix, nonspecific binding can immobilize proteins, hindering selective motion, unless those proteins are able to continue diffusing while bound, a feature which we argue is key to the selective transport of the NPC as well as the biofilters discussed here. The following section presents three particular examples of selectivity in biological systems, from widely disparate areas, which bear striking similarities to the selectivity of the nuclear pore. In the remainder of this work, we model selective transport using a minimal set of characteristics that, while inspired by the nuclear pore, apply to all of the systems here as well.

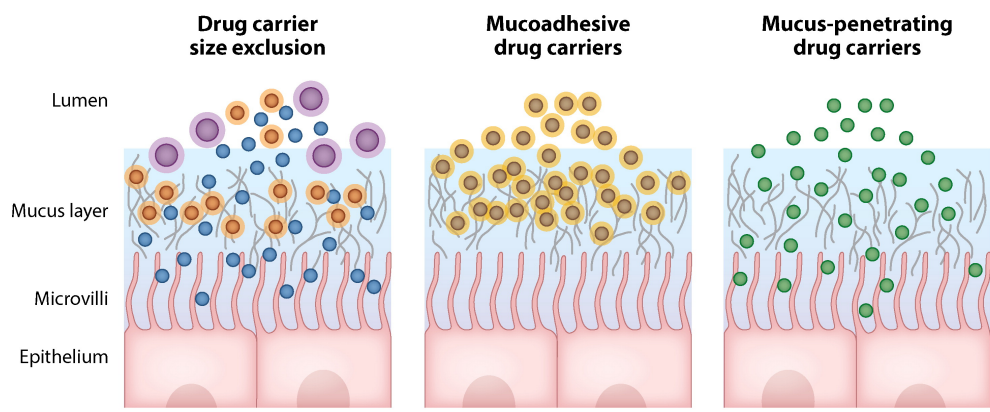
1.2.1 Drug delivery through mucus barriers

One medically-important selective biological barrier is the mucus which lines organs such as the lungs, nose, and stomach. In particular, lung mucus presents a barrier to delivery of inhaled medication. If nanoparticles containing drugs for lung diseases such as asthma and lung cancer could be inhaled and taken up by lung cells, doses could be lower, as the uptake would be more targeted [71, 72]. However, lungs are coated by a layer of mucus intended to prevent foreign objects from reaching the lung cells. In order to deliver nanoparticles to lung cells, they must be engineered to pass the selective mucus barrier.

Mucus consists predominantly of disordered glycoproteins known as mucins, though other components such as lipids are present as well [73]. These entangled mucins present multiple barriers to nanoparticles, as shown in Fig. 1.4. First, large particles are excluded due to the 150-350 nm average pore size of mucus gels [74, 75]. Second, even particles which are small enough to enter the mucus layer often bind to mucins. In fact, mucoadhesive particles (MAPs) have been specifically engineered on the principle that increasing the nanoparticle's lifetime within the mucus will lead to more efficient drug delivery [76]. However, diffusion of MAPs is often so slow that they do not penetrate beyond the edge of the mucus layer. Furthermore, mucus gradually replaces itself on clearing timescales which vary depending on the type of mucus. Nanoparticles in the outermost region will be cleared more rapidly than those which diffuse deeply into the mucus layer [77].

Currently, the best nanoparticle delivery through the lung mucus barrier is by small, inert particles which minimize nonspecific interactions with mucins. These mucus-penetration particles (MPPs) are typically coated in PEG or another inert polymer [72, 79]. MPPs can reach much higher diffusion constants in mucus than can MAPs [75, 80–82].

The selective barrier of lung mucus bears similarities to the selectivity of the nuclear pore in that it consists of disordered proteins which bind to particles impinging on the barrier. However, in the case of mucus, binding inhibits the flux of particles through the selective filter, while binding enhances the flux of transport factors through the nuclear pore. A better understanding of the role



 Carlson TL, et al. 2018.
Annu. Rev. Biomed. Eng. 20:197–220

Figure 1.4: Nanoparticle drug delivery through a mucus barrier. Particles which are too large cannot pass the size-exclusion barrier. Mucoadhesive particles penetrate the mucus layer but are trapped by binding interactions. Inert mucus-penetrating particles have a much higher diffusion constant in mucus. Figure adapted from [71, 78]

of binding and bound diffusion to a selective filter such as the nuclear pore could suggest novel strategies for nanoparticle delivery through lung mucus. Perhaps binding can be leveraged in a way that enhances nanoparticle flux over that of inert particles, improving drug delivery to the lungs.

1.2.2 Diffusion of DNA-binding proteins in the nucleus

The principles of selective filtering in the nuclear pore appear in biological systems beyond straightforward filtering. In particular, transient binding and bound-state diffusion are important to DNA targeting in the nucleus by transcription factors and DNA damage repair proteins. A protein diffusing in the cell’s nucleus has many of the same constraints and capabilities as a transport factor transiting the nuclear pore: it is surrounded by a high concentration of flexible tethers to which it binds transiently. Just as this situation leads, counterintuitively, to high flux of transport factors through the nuclear pore, DNA-targeting proteins find their specific targets much more rapidly than would be naively predicted [83].

Solutions to this “needle in the haystack” challenge resemble possible mechanisms of bound diffusion in the nuclear pore complex. In particular, it is widely accepted that the search for targets is made more rapid through facilitated diffusion, involving proteins sliding along strands of DNA. However, the optimal time spent in a one-dimensional search as opposed to a free three-dimensional search is unclear; as is the effectiveness of sliding as opposed to multiple, rapid binding and unbinding events [84]. This mechanism is reminiscent of both the sliding mechanism predicted in some transport factors and of the effect of diffusion while bound to a flexible tether [85]. Additionally, transfer of a multivalent transcription factor between two strands of chromatin, a mechanism known as intersegmental hopping, can increase the protein’s search space similarly to the multi-valent inter-Nup hopping that is available to transport factors [86, 87]. Finally, transient binding plays an important role in the search for DNA targets. This speed-stability paradox reflects the fact that, like in the nuclear pore, proteins must bind very weakly to their DNA tethers to avoid becoming immobile. Unlike nuclear transport, however, DNA-binding proteins must bind more tightly to their targets upon reaching them [88, 89].

A case in point, further discussed in Sec. 2.6.1, is that of poly(ADP-ribose) polymerase 1 (PARP1), a DNA damage repair protein which rapidly localizes to sites of DNA damage. PARP1 binds damaged DNA with low nanomolar affinities, and appears to bind undamaged DNA only a few orders of magnitude more weakly [90]. Given that there are up to 5 mM nonspecific DNA binding sites in the nucleus, the speed with which PARP1 diffuses (\sim 10 times slower than in buffer) is remarkable [88]. PARP1 contains multiple DNA-binding sites, and an inter-strand hopping mechanism has recently been demonstrated, which may explain its rapid diffusion [91]. However, removal of that mechanism only slightly slows the recruitment of PARP1 to sites of DNA damage, suggesting that a further mechanism of bound-state diffusion is necessary [92]. The principles of selective nuclear transport may help to explain the rapid motion of PARP1, along with other DNA damage repair proteins and transcription factors.

1.2.3 Subcompartments in liquid droplets

Features of nuclear transport such as highly-concentrated disordered proteins and bound-state diffusion also appear in liquid-liquid phase separated droplets. These membraneless organelles are rapidly gaining prominence as it becomes clear that many cellular functions are regulated through the phase separation of mixtures into phase rich in various proteins and other cellular components. Membraneless organelles include nucleoli, which aid in processing ribosomal DNA genes within the nucleus, and RNA granules, which help sort mRNA [6, 94].

Liquid-liquid phase separation typically occurs for mixtures containing IDPs with “sticker” and “spacer” regions, similar to the hydrophobic FG repeats and hydrophilic linker regions in FG Nups [95]. These phases are highly concentrated, but the proteins that comprise them remain mobile. Interestingly, evidence is developing for subcompartments of varying composition within some liquid droplets. Nucleoli contain multiple subcompartments which are thought to perform distinct functions (Fig. 1.5) [93, 96, 97], while RNA granules have recently also been shown to have a core-shell structure [94, 98].

The investigation of subcompartments in membraneless organelles is in its very early stages,

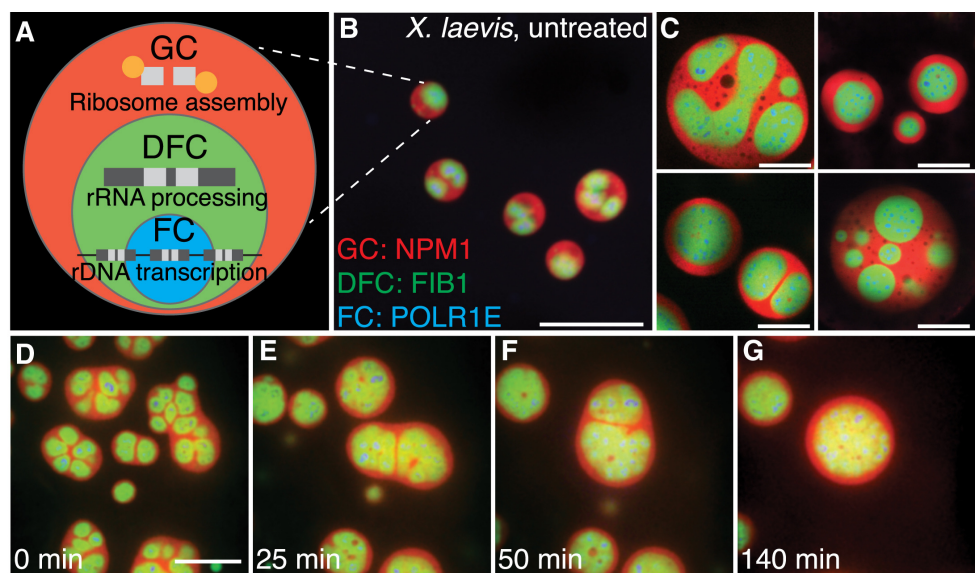


Figure 1.5: Phase-separated subcompartments of *Xenopus* nucleolus. (A) Schematic of subcompartments. (B)-(C) Fluorescence microscopy image of nucleoli with subcompartments in red, green, and blue. (D)-(G) Time-course showing dissolution of compartments after actin disruption. Figure adapted from [93].

with much of the current work going towards simply identifying the components of the compartments. Discussion of their purpose and mechanisms is still quite speculative. However, it seems plausible that one function of these compartments is to selectively concentrate enzymes or other proteins to increase reaction rates. RNA bodies in particular are known to sort and sequester mRNA [94]. As such, the presence of disordered, multivalent proteins may not simply be necessary for the formation of phase separated droplets, but could potentially assist in selectively filtering the components of the subcompartments. If nuclear transport is a guide, binding partners of the IDPs which form the outermost phase might have a higher flux into the inner compartments than nonbinding proteins. Additionally, in the context of bound-state diffusion, liquid droplets represent maximal bound diffusion, as binding to an IDP in solution will not appreciably slow the diffusion of the binding partner. While these possibilities will not be testable for some time, membraneless organelles may prove to be a fascinating application of selective biofiltering.

1.3 Project goals and motivation

All of the systems described above involve the rapid flux of proteins which still bind highly selectively to their environment. This apparent paradox further includes common features such as ultrafast, transient, multivalent binding and the presence of binding sites on flexible, dynamic tethers. The mechanism by which these features lead to such remarkable selective properties is not obvious. We approached the problem through both modeling and experiment and identified a common key parameter in the form of bound-state diffusion. While the theory and experimental setup were based on nuclear transport, both platforms are general enough to apply to a number of selective biofilters.

1.3.1 Model selective transport as simply as possible

Despite the complexity of nuclear transport, many components can be removed or approximated without eliminating its unusual selective properties. For example, Nups which are asymmetrically distributed along the axis of the nuclear pore can be removed, as can a large fraction of

Nups overall, without destroying selectivity [19–22]. And though many transport factors require active release from the pore, others, such as NTF2, do not; selectivity is not therefore dependent on active release. We decided to model the pore in order to answer the question: What are the minimum requirements for selective transport?

In the course of creating the model, we found that the minimum requirements are quite simple indeed. The model discussed in Chapter 2 not only dispenses with non-uniformly distributed Nups and facilitated release, but also with non-specific crowding, Kap-centric control of the nuclear pore, the Ran cycle, and even the nanopore geometry. Instead, the pore is treated as a bulk material of finite thickness with an artificially-imposed concentration gradient to drive flux across it. Competition for binding sites is retained in the form of binding site saturation, but even without this feature we see selective flux across the barrier. Our model fundamentally contains only diffusion and binding of transport factors to Nups - an extremely streamlined depiction of nuclear transport, and one that can even be treated semi-analytically.

The simplicity of our model made the key parameter clear: we could not reproduce the selectivity of the nuclear pore without allowing bound-state diffusion, that is, assuming that bound Nup - transport factor complexes were mobile within the pore. Bound diffusion provides a possible answer to the paradox of nuclear transport, resulting in a higher flux of transport factors, which bind to Nups, than inert proteins which do not. In our model, this straightforward mechanism alone gave rise to the decidedly unintuitive behavior of the nuclear pore.

Having identified bound-state diffusion as an important parameter for selective filters, we investigated possible methods of bound diffusion within the nuclear pore. Two possibilities arose from basic, well-accepted facts of nuclear transport: tethered diffusion arising from the disordered, flexible nature of the Nups, and inter-chain hopping of the transport factor due to its binding multivalency. Upon investigation, both mechanisms can plausibly provide the high bound diffusion constant needed to reproduce the selectivity of the nuclear pore.

While this model was inspired by nuclear transport, it ultimately relies on only a few key properties of the system. With this model, we predict selective transport will occur where there

is bound-state diffusion, which can be readily obtained if flexible IDPs are present for tethered diffusion, or if highly transient, multivalent binding allows for moving from one site to another while remaining bound. The systems described above in Sec. 1.2 fall into this category, as likely do many others. Furthermore, these principles might guide synthetic selective biofilters with novel rapid, highly-selective properties.

1.3.2 Experimentally test bound-state diffusion in biomaterials

After developing the minimal model of selectivity, we began developing a synthetic biofilter with which to experimentally probe the effect of bound-state diffusion on selectivity. The model itself is sufficiently general to apply to a wide range of filters, giving us some freedom in designing a material to test its predictions. We chose to use the nuclear pore as inspiration for this material because its key components are so well known, if not well understood. In order to capture the key features of selectivity, we designed hydrogels containing peptide tethers derived from FG Nups. The transport factor NTF2 served as a test protein whose diffusion we could compare with a similarly-size but nonbinding counterpart. These hydrogel nuclear pore mimics display the mechanisms that lead to selective transport in our model: flexible, dynamic tethers which can transiently bind to transport factors, along with multivalent transport factors which can “hop” between peptide chains without fully unbinding. We predict that these features will be sufficient for bound-state diffusion of the transport factor within the hydrogel.

As with the theoretical model, many of the NPC-specific details, such as the nanopore structure and Ran gradient, were omitted. A bulk material was used instead of nanopores because our model should apply equally well to both, and a macroscopic hydrogel is much easier to study. We quickly realized that hydrogels are a challenging system to use for protein separation. The nuclear pore mimics have a rigorous set of competing constraints: for example, the hydrogel should be in mechanical equilibrium and homogeneous, while still well-sealed to a flow chamber so that proteins cannot bypass the gel. Chapter 3 documents the design of the hydrogel nuclear pore mimics. Many modifications intended to improve the diffusion properties and reproducibility of the hydrogels

proved unsuitable for our needs. However, we eventually produced a biomaterial that can be used to measure bound diffusion, while also developing more general guidelines for designing hydrogels that are useful for protein separation.

The resulting bound-state diffusion measurements are presented in Chapter 4. Fluorescence recovery after photobleaching (FRAP) was used to determine the effective diffusion constants of both NTF2 and an inert protein, from which the bound diffusion constant was calculated. The data analysis ultimately required a two-dimensional Fourier series solution to the diffusion equation, resulting in a set of data-processing scripts which can be applied to any circular material undergoing equilibration with a fluorophore. We measured a non-zero bound diffusion constant that is consistent with the predictions of our model, and tested the effect of varying Nup length on bound-state diffusion. Our results indicate that these nuclear-pore-inspired hydrogels can be used to probe the effect of our model's parameters on bound diffusion.

While bound diffusion is a key parameter in our selectivity model, the aggregation state of the Nups could also affect selectivity. Aggregated Nups will be less dynamic and effectively act as shorter tethers, limiting bound diffusion. In Chapter 5, we probed the aggregation behavior of an FG-Nup-derived peptide in several crowded conditions. Using a fluorescent amyloid assay, we identified significant differences in the aggregation dynamics in the presence of different crowders, including between poly(ethylene glycol) (PEG) and polyvinylpyrrolidone (PVP), two inert polymers that are widely presumed to be interchangeable as crowders. We followed this aggregation assay with NMR and fluorimetry studies in order to investigate the nature of the changes. The results suggest that the presence of an aromatic ring in PVP may interact with the phenylalanines in the FG motifs of the peptide, changing its local chemical environment and therefore its aggregation behavior.

Although a true hydrogel-based selective biofilter proved challenging to design, our nuclear-pore-inspired material can be used to measure the bound-state diffusion of proteins. This parameter is likely important to a variety of problems involving rapid transit of highly-selective proteins. It is my hope that the model and biomaterials developed here can be used to investigate these systems

more generally in the future. This work suggests that bound-state diffusion, particularly when resulting from transient, multivalent binding, may explain a number of unusual biological filters.

1.4 Biophysics is beautiful

Even beyond the ample practical reasons to study nuclear transport, it is a fascinating process, full of counterintuitive results and apparent paradoxes. The nuclear pore is at once an incredibly intricate nano-machine and surprisingly robust to perturbation. Passage through the nuclear pore is carefully controlled by complex cellular processes, yet the mechanism of selectivity itself does not require energy input. Nuclear transport can enhance the flux of transport factors hundreds of times over that of inert proteins using a mechanism that conventionally *reduces* protein mobility.

Where the NPC is not apparently self-contradictory, it is a picture of extremes. FG Nups are not only disordered, many show virtually no signs of secondary structure whatsoever and do not order appreciably upon binding transport factors. Nup - transport factor binding is extreme on many axes: the affinity, likely in the millimolar range, is weak enough that most biochemists would characterize it as non-specific binding, yet it permits a high flux through the pore. At the same time, the on-rate is ultrafast, bounded by the physical diffusion limit rather than chemical considerations. Finally, with dozens of FG motifs along the length of each Nup, and multiple binding pockets on each transport factor, Nup - transport factor binding is dizzyingly multivalent. It is perhaps no wonder that measurements of the binding affinity have historically spanned six orders of magnitude; at this level of multivalency, even the notion of “binding affinity” itself becomes convoluted. In almost every respect, the binding interactions which underpin selective transport are as far removed as possible from textbook protein-protein interactions. The nuclear pore is a fundamentally *weird* system and deserves to be studied purely for the joy of discovering how something so unusual operates.

Furthermore, the details of nuclear transport are all but invisible even to the most cutting-edge biochemical techniques. The timescale of transport is too fast, the size too small, and the disordered Nups too dynamic to permit direct visualization of transport. This is a system which

practically demands to be studied using nontraditional, interdisciplinary methods.

There is value in approaching the nuclear pore specifically from the perspective of physics. Biophysics as a field experiences constant tension between the need to account for the incredible complexity of any living system and the drive to reduce it to its smallest, tidiest set of component parts. As a physicist, I take deep satisfaction from applying a broad and simple theory to a complicated system and still getting meaningful results. All of the messy intractable details are of course ultimately necessary for life to exist, but if a big, sweeping, absurdly simple, underlying principle can explain even 50% of a complex system, that's beautiful. Such opportunities abound in biophysics, from flies which right themselves after mid-flight perturbation, to the scaling of barbs in cat tongues, to how cucumber tendrils coil and overwind, to the nuclear pore complex and beyond [99–101]. Sometimes it's worthwhile to apply basic physical theories to ridiculously complicated things which they manifestly cannot fully explain - valuable practical advances frequently arise from surprisingly slender foundations.

Whether viewed through a practical, intellectual, or aesthetic lens, there is much to be gained from the study of nuclear transport and, more broadly, of binding and diffusion in selective biofilters. Certainly I have found that, despite the setbacks and disappointments which accompany all research, I have never been able to describe my work to others without becoming truly enthusiastic yet again.

Chapter 2

Modeling bound-state diffusion in selective filters

The nuclear pore is a clear example of a selective biofilter, but the precise mechanism of selectivity is not well understood. In particular, an apparent paradox arises from the fact that transport factors, which bind to FG Nups within the pore, have a much higher flux through the pore than inert, nonbinding proteins. This result is somewhat counterintuitive, given that binding must necessarily slow the passage of a transport factor through the pore. In addition to nuclear transport, binding and diffusion are important in many other biofilters as well, including drug delivery through a mucus layer liquid-liquid phase separation (Sec. 2.6) [6, 72, 73, 79, 80, 93]. We wanted to understand how binding increases flux through selective biofilters.

To that end, we developed a simple mathematical model of selective transport inspired by the nuclear pore. While the model is based on nuclear transport, it is general enough that it can be applied to a wide range of biological systems and synthetic biofilters. Unlike most existing theoretical models of nuclear transport, which reduce transport to diffusion in a single effective one-dimensional potential, this model does not require simulations or a precise accounting of the locations and composition of Nups along the pore axis [1, 18, 58, 62, 102]. It is equally applicable to a bulk material as to a nanopore. A few other first-principles models of the pore have been developed using similar differential equations but making different assumptions about boundary conditions and binding equilibrium [61, 67].

The primary surprising result of our model was the importance of bound-state diffusion for selectivity. No selective filtering was possible if the transport factor - Nup complex was immobile,

regardless of the other parameters. However, if bound diffusion within the pore was permitted, the selective flux of transport factor through the pore as compared to that of an inert protein approached that measured experimentally. These results suggest that bound-state diffusion is key to selective transport within the nuclear pore and perhaps to a number of other biofilters as well.

The work in this chapter was a close collaboration between myself, Mike Stefferson, and Loren Hough. Mike contributed significantly to developing the model and wrote the numerical simulations in both the linear and non-linear cases.

2.1 Simplified model of nuclear transport

Nuclear transport is highly complex, but its unusual selective properties can be modeled much more simply than can the entirety of transport. A major goal of our model was to reproduce the selectivity of the nuclear pore in most straightforward way possible. To that end, we made many simplifying assumptions. The nuclear pore was treated as a one-dimensional selective membrane uniformly filled with Nups. While the nuclear pore itself has a non-uniform, asymmetric distribution of Nups along its axis, as well as variation in the FG motif density along its radius, its selectivity remains intact when the asymmetric Nups are removed. In fact, a significant fraction of Nups can be removed without destroying selectivity [19–22]. Any possible wide capture area outside the pore is also neglected [103].

Many transport factors require active release from the pore and their cargo [24, 35, 60, 104]. To avoid the complications of facilitated release, we focused on the diffusion of Nuclear Transport Factor 2 (NTF2) through the selective barrier. NTF2 does not require active release from the pore, and, while it is at the cusp of the passive diffusion limit at 30 kDa, its flux through the pore is approximately 30 times higher than that of a similarly-sized non-binding protein [60, 61]. The small size of NTF2 is also a benefit in that it is significantly smaller (~ 5 nm) than the depth of the nuclear pore (~ 100 nm), meaning that our approximation of the pore as a bulk material is appropriate.

Our model also assumes that the rate-limiting step of nuclear transport is motion within the

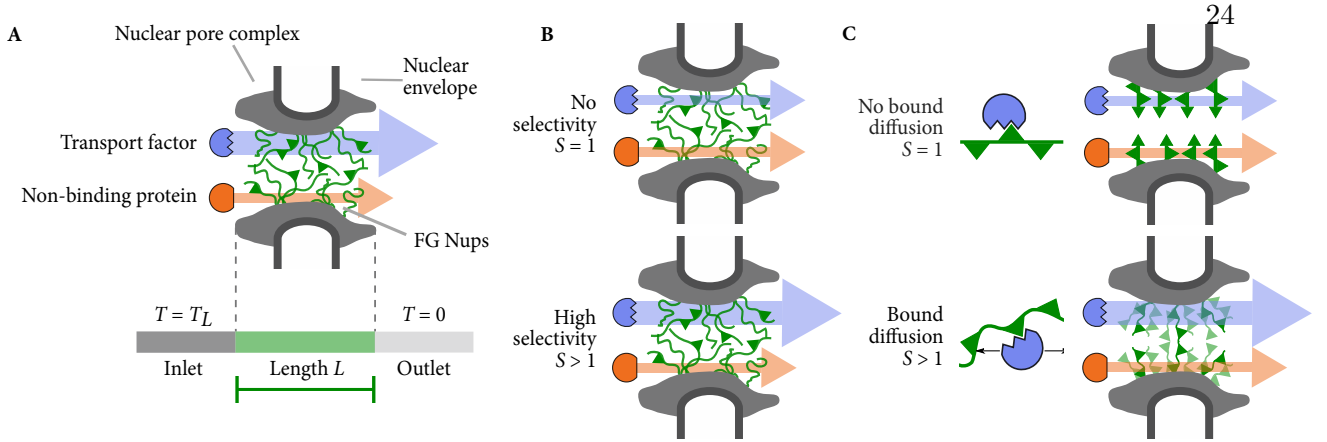


Figure 2.1: Schematics of the nuclear-pore complex and model. (A) The nuclear pore complex (gray) is filled with FG Nups (green polymers) that selectively passageway transport factors that bind to FG Nups (blue) while blocking non-binding proteins (red). The central channel of the pore has length L . Protein concentration is high on the left (inlet) and low on the right (outlet). (B) Selectivity quantifies the degree of selective transport through the pore. A non-selective pore with $S = 1$ has the same flux for a transport factor as for a non-binding protein (top). A selective pore with $S > 1$ has a larger flux for a transport factor than a non-binding protein (lower). (C) The bound diffusion coefficient quantifies the mobility of a bound transport factor. A transport factor may be immobile (top) or mobile (lower) when bound.

pore, not entry or exit. In single-molecule measurements, most of the transport time is spent in a random walk within the central channel [62, 105].

We consider a channel of length L filled homogeneously with Nups that separates two reservoirs Figure 2.1A. A concentration difference is imposed between the two reservoirs in order to drive flux. Within the channel are free transport factor (concentration T), free FG Nups (N), and bound TF-FG complex (C), with total Nup concentration $N_t = N + C$. TF diffusion within the channel ($0 < x < L$) is described by the reaction-diffusion equations

$$\frac{\partial T}{\partial t} = -k_{\text{on}}TN + k_{\text{off}}C + D_F \frac{\partial^2 T}{\partial x^2}, \quad (2.1)$$

$$\frac{\partial C}{\partial t} = k_{\text{on}}TN - k_{\text{off}}C + D_B \frac{\partial^2 C}{\partial x^2}. \quad (2.2)$$

TF-FG interaction has on-rate constant k_{on} , off-rate k_{off} , and dissociation constant $K_D = k_{\text{off}}/k_{\text{on}}$. We include competition between TFs for FG binding sites [1]. The diffusion constants of free (D_F) and bound (D_B) TFs are spatially constant. The fixed reservoir TF concentrations are T_L (inlet, left) and 0 (outlet, right).

The flux of transport factor out of the pore is $J = -D_F \partial T / \partial x|_{x=L}$. We defined a figure of

merit, selectivity, to describe the enhancement in transport factor flux at steady-state over that of a non-binding protein (Fig. 2.1B). Selectivity is defined as

$$S = \frac{J_{\text{binding}}(t \rightarrow \infty)}{J_{\text{non-binding}}(t \rightarrow \infty)}. \quad (2.3)$$

Mike Stefferson developed code that numerically integrated the full, nonlinear reaction-diffusion equations and calculated selectivity [106].

2.1.1 Linear appoximation and analytic solution

Experimental evidence suggests that the flux of transport factors within the pore is linearly related to their concentration [66, 107]. This would imply that few of the Nup binding motifs are occupied, so that $C \ll N$. In this case, the concentration N of un-bound Nups is approximately equal to the total Nup concentration N_t , a constant. Letting $N \approx N_t$ linearizes the reaction-diffusion equations Eqns. 2.2, at which point they can be solved analytically. The solution was developed by Loren Hough and is presented here. The full nonlinear numerical model was used in all other sections unless noted otherwise.

The analytical solution for flux can be directly derived in the linear case. For ease of calculation, we reverse the concentration gradient used in the nonlinear model, so that $T(0) = 0$ and $T(L) = T_L$, allowing us to calculate flux at $x = 0$. The reaction-diffusion equations (2.1, 2.2) at steady state in the linear limit $N \approx N_t$ are

$$0 = -k_{\text{on}}N_tT + k_{\text{off}}C + D_F \frac{\partial^2 T}{\partial x^2}, \quad (2.4)$$

$$0 = k_{\text{on}}N_tT - k_{\text{off}}C + D_B \frac{\partial^2 C}{\partial x^2}. \quad (2.5)$$

The change of variables $C = C_x + N_t K_A T$ ($K_A = k_{\text{on}}/k_{\text{off}} = 1/K_D$) yields

$$0 = k_{\text{off}}C_x + D_F \frac{\partial^2 T}{\partial x^2} \quad (2.6)$$

$$0 = -k_{\text{off}}C_x + D_B \frac{\partial^2 C_x}{\partial x^2} + N_t K_A D_B \frac{\partial^2 T}{\partial x^2}. \quad (2.7)$$

Substituting $C_x(x) = -\frac{D_F}{k_{\text{off}}} \frac{\partial^2 T}{\partial x^2}$ makes equation (2.7) a fourth-order ODE

$$\lambda^2 \frac{\partial^2 T}{\partial x^2} = \frac{\partial^4 T}{\partial x^4}, \quad (2.8)$$

where $\lambda^2 = k_{\text{off}}(D_F + N_t K_A D_B)/(D_F D_B)$. Solutions to this equation have the form $T(x) = b + mx + fe^{\lambda x} + ge^{-\lambda x}$, where b , m , f and g are constants fixed by four boundary conditions: free TF concentration is fixed at the edges of the pore, with $T(0) = 0$, $T(L) = T_L$. No flux of bound TF into or out of the pore occurs, giving $\partial C/\partial x|_{x=0} = 0$, $\partial C/\partial x|_{x=L} = 0$. The constants of integration are

$$b = -(f + g), \quad (2.9)$$

$$m = \frac{T_L \lambda (\zeta - (D_F/k_{\text{off}})\lambda^2) (e^{L\lambda} + 1)}{2\zeta - 2\zeta e^{L\lambda} + L\zeta\lambda - (D_F/k_{\text{off}})L\lambda^3 - (D_F/k_{\text{off}})L\lambda^3 e^{L\lambda} + L\zeta\lambda e^{L\lambda}}, \quad (2.10)$$

$$f = -\frac{\zeta m}{\lambda (\zeta - (D_F/k_{\text{off}})\lambda^2) (e^{L\lambda} + 1)}, \quad (2.11)$$

$$g = \frac{\zeta m + f\zeta\lambda - (D_F/k_{\text{off}})f\lambda^3}{\zeta\lambda - (D_F/k_{\text{off}})\lambda^3}. \quad (2.12)$$

where $\zeta = N_t/K_D$. This leads to a concentration profile of bound TFs

$$C(x) = \zeta \left(b + mx + fe^{\lambda x} + ge^{-\lambda x} \right) - (D_F\lambda^2/k_{\text{off}}) \left(ge^{-\lambda x} + fe^{\lambda x} \right). \quad (2.13)$$

To determine the selectivity, we calculate the steady-state flux out of the pore $J = -D_F \partial T / \partial x|_{x=0}$, giving

$$J = -D_F(m + \lambda f - \lambda g) \quad (2.14)$$

$$J = \frac{T_L(D_F^2/k_{\text{off}})\lambda^3 (e^{L\lambda} + 1)}{2\zeta - 2\zeta e^{L\lambda} + L\zeta\lambda - (D_F/k_{\text{off}})L\lambda^3 - (D_F/k_{\text{off}})L\lambda^3 e^{L\lambda} + L\zeta\lambda e^{L\lambda}} \quad (2.15)$$

For a non-binding particle, $C(x) = 0$, $T = T_L x/L$, and

$$J_n = -\frac{D_F T_L}{L}. \quad (2.16)$$

The selectivity J/J_n is then independent of T_L in the linear approximation.

2.1.2 Effect of bound-state diffusion constant

When the selectivity is calculated for the full nonlinear equations, bound-state mobility is immediately obvious as the key parameter. We were unable to create a selective material if the bound diffusion constant D_B was set to zero, i.e. if the Nup-transport factor complex was immobile

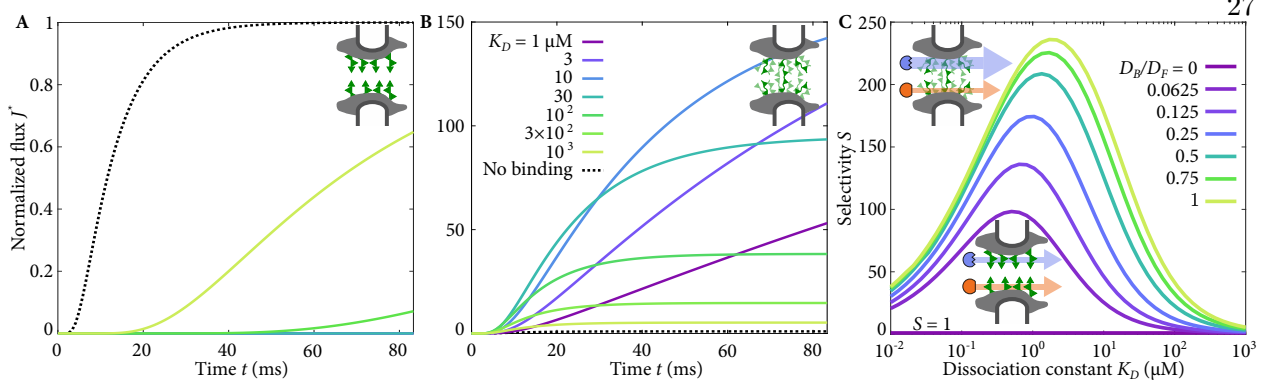


Figure 2.2: Flux through the pore and selectivity for TFs with varying bound mobility. (A) Flux as a function of time when TFs are immobile while bound, with varying binding affinity as in (B). (B) Flux as a function of time when TFs are mobile while bound with $D_B = D_F$, with varying binding affinity. (C) Selectivity as a function of dissociation constant with varying bound diffusion coefficient.

while bound. In those cases, the steady-state flux of transport factor and inert protein was identical regardless of the values chosen for k_{on} or k_{off} giving a selectivity of $S = 1$. The transient flux ratio did depend on binding kinetics, as shown in Figure 2.2A and B. As would be expected, the transient flux of transport factor out of the material was suppressed relative to that of the inert protein, as a population of the transport factor filled binding sites throughout the material. Once binding equilibrium has been established, however, the immobile population of bound transport factors cannot contribute to the flux out of the pore, and the steady-state flux of binding and non-binding proteins is identical.

However, when bound-state mobility is allowed and $D_B > 0$, the system's selectivity can greatly increase, as shown in Figure 2.2C. The transient response is dramatically different as well. Now transport factor flux very rapidly outpaces that of inert protein. It should be noted that the timescale for equilibration is similar to that observed experimentally for NTF2, approximately 10 ms.

In order to create these plots, we used the FG-filled pore length $L = 100$ nm [108, 109]. Total FG Nup concentration was determined from an estimate of the number of TF binding sites (800), and the volume of a cylinder of diameter 60 nm and length L . Finally, an estimate of the free diffusion constant of NTF2 moving within the nuclear pore is needed. This value has not

been directly measured, but it was estimated at $D_F = 0.12 \mu\text{m}^2/\text{s}$ using a similar value for a non-binding protein [39]. As would be expected, this diffusion constant is smaller than that of a karyopherin in the nucleus, which has been estimated at $D_F = 1 \mu\text{m}^2/\text{s}$ [110]. In order to estimate the concentration gradient between nucleus and cytoplasm, we need to know the concentration of transport factor just inside the cytoplasmic side of the nuclear pore. There will be an energy barrier to any protein entering the pore because of the entropic penalty of the Nups. We estimate this barrier is approximately $1.5 k_B T$ for an NTF2 sized molecule [1]. We estimate the cytoplasmic concentration of NTF2 is $5 \mu\text{M}$. Then $T_L = 5 \times e^{-1.5} \mu\text{M} = 1 \mu\text{M}$.

Experimental evidence suggests that the on-rate constant of Nup-transport factor binding is diffusion-limited, with $k_{\text{on}} = 10^{-3} \mu\text{M}^{-1} \mu\text{s}^{-1}$ [11, 26]. The off-rate constant is given by $k_{\text{off}} = k_{\text{on}} K_D$. Measured values of the dissociation constant K_D span several orders of magnitude, between approximately between 10 nM and $100 \mu\text{M}$ [1, 23–27, 58]; therefore the off-rate constant is not well-determined. Figure 2.6B and C show the bound diffusion coefficient and selectivity for a range of K_D values spanning those measured experimentally, with a fixed, diffusion-limited on-rate. Throughout this work, we consider a wide range of dissociation constants.

This model provides a straightforward method of predicting the selectivity of various other hydrogel nuclear pore mimics [49–51, 111]. A table of predicted selectivity is provided in Appendix A.

Allowing the bound diffusion constant to approach the free diffusion constant, using the above parameters, selectivity can approach the values seen in experimental measurements (Table 2.1). The interplay between binding kinetics and diffusion leads to an optimal dissociation constant near $1 \mu\text{M}$ for maximum selectivity (Figure 2.2C). Selectivity decreases for high K_D because binding is too weak to significantly increase TF concentration in the pore. For low K_D , tight binding causes the concentration of bound complexes to become approximately constant across the pore, eliminating the concentration gradient needed to provide flux across the pore.

2.1.3 Bound diffusion in the linear model

In the linear approximation described in Sec. 2.1.1, bound diffusion plays a similar role as in the full nonlinear model. By definition, the Nup binding sites don't saturate in the linear model. This leads to a plateau in the selectivity at tighter binding, rather than a peak (Fig 2.3). However, the linear model becomes non-physical for $K_D < N_t$, denoted by the dotted line in Fig. 2.3C.

The role of individual parameters can be more easily investigated using the linear approximation. Figure 2.4 illustrates the effect on selectivity of varying the on-rate constant, total FG Nup concentration, free diffusion constant, and pore length. Figure 2.5 does the same for the absolute flux of transport factor through the pore. These results show that increasing the on-rate constant or the total Nup concentration results in both higher selectivity and transport factor flux, a conclusion which is supported by the fact that these values are maximized within the nuclear pore [11,26]. However, there is a trade-off between selectivity and flux for the pore length and free diffusion constant. Increasing pore length or decreasing free diffusion constant make the pore more selective but lower the absolute flux of transport factor.

Table 2.1: Comparison between experimental results for NTF2 and GFP (a similarly-sized non-binding protein) and model predictions. Flux measured in units of molecules per pore per second.

Method	Cell type	Species	Flux	Selectivity	Notes
OSTR	<i>Xenopus</i>	NTF2	91–123	24–37	[40]
		GFP	3.3–3.8		
OSTR	<i>Xenopus</i>	NTF2	47.3	43	[41]
		GFP	1.1		
Permeabilized cells	HeLa	NTF2	250	125	[39]
		GFP	2		
Model	–	Binding	2–480	1–240	This work
		Non-binding	2		

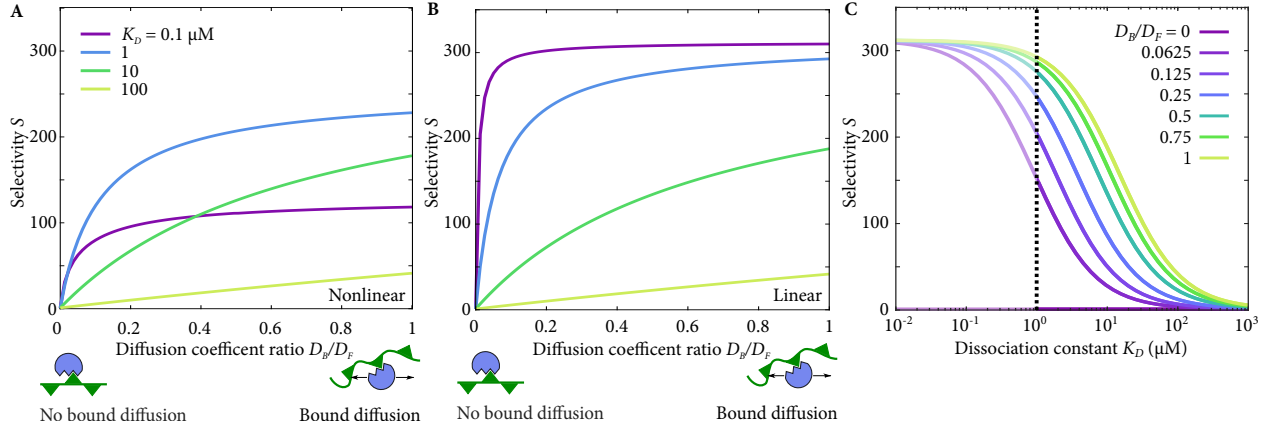


Figure 2.3: (a, b) Selectivity as a function of diffusion coefficient ratio, with varying dissociation constant, in the full nonlinear model (a) or in the linear approximation (b). (c) Selectivity as a function of dissociation constant, with varying diffusion coefficient ratio, in the linear approximation. The region to the left of the dotted line is non-physical; the full nonlinear solution should be used.

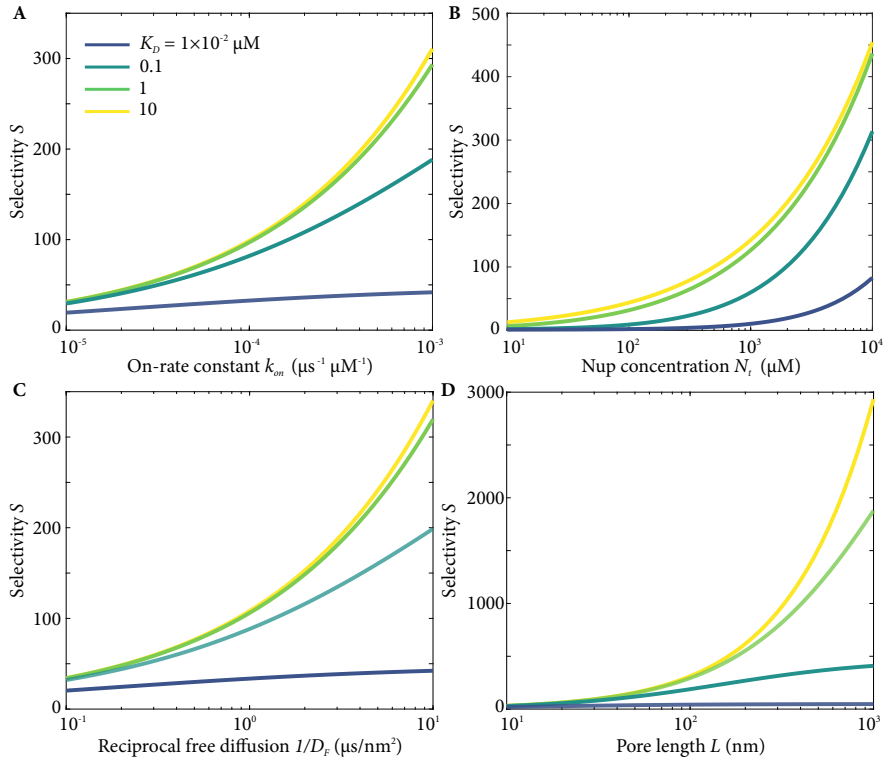


Figure 2.4: Dependence of selectivity on variation of individual parameters: (a) on-rate constant, (b) total FG Nup concentration, (c) inverse of the free diffusion coefficient, and (d) pore length, with varying dissociation constant. All values calculated using the linear solution to the binding-diffusion equations. Bound diffusion coefficient $D_B = 0.1D_F$. Other parameters fixed at values from the NPC parameters section.

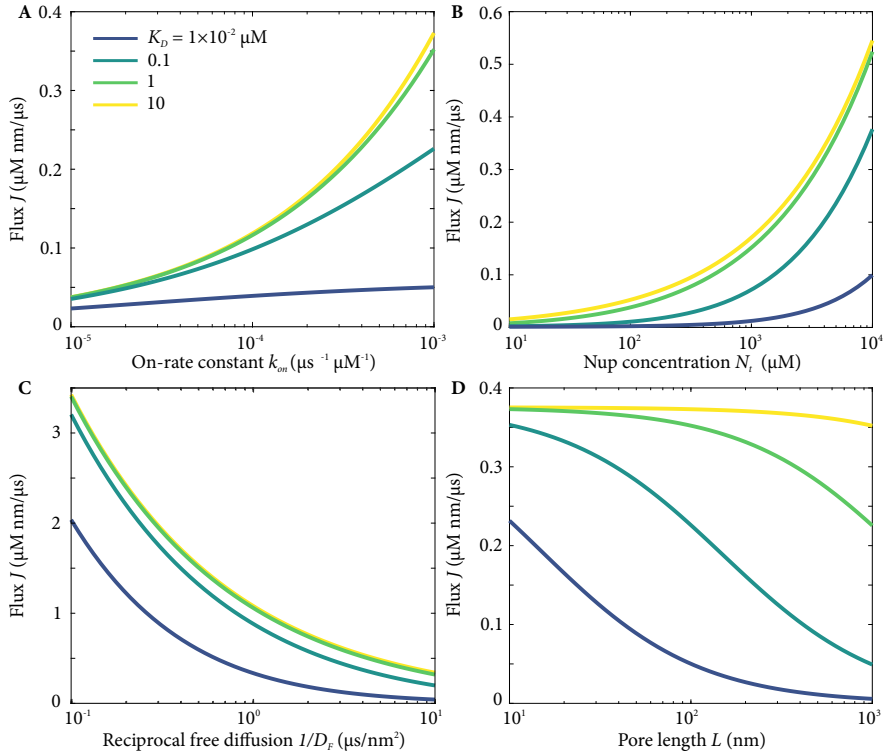


Figure 2.5: Dependence of flux on variation of individual parameters: (a) on-rate constant, (b) total FT Nup concentration N_t , (c) inverse of the free diffusion coefficient, and (d) pore length, with varying dissociation constant. All values calculated using the linear solution to the binding-diffusion equations. Bound diffusion coefficient $D_B = 0.1D_F$. Other parameters fixed at values from the NPC parameters section.

2.2 Mechanisms of bound transport factor mobility

The importance of bound diffusion to selectivity in our model raises the question of how transport factor- Nup complexes might diffuse within the pore. The following sections describe two possible mechanisms of bound-state diffusion within the nuclear pore: tethered diffusion and inter-chain hopping due to binding multivalency. Both mechanisms are appealing because they rely only on well-established properties of Nups and transport factors. Our results suggest that each mechanism could contribute significant selectivity.

2.3 Bound mobility through tethered diffusion

One possible mechanism of bound-state diffusion within the nuclear pore is tethered diffusion. FG Nups, as disordered proteins, are flexible and highly dynamic [8, 11, 112, 113]. It is not clear whether they form polymer brushes or crosslinked hydrogels within the nuclear pore, but in either case tethered diffusion remains a viable mechanism of bound diffusion. In the case of a polymer brush, one end of an FG Nup is anchored to the NPC scaffold, but the other end is free, affording mobility to a bound transport factor. If FG Nups are crosslinked, the effective length of the flexible tether will be shorter, but the same principle of tethered diffusion will apply.

Flexible polymers behave as entropic springs [114] if they are not highly stretched. Therefore, a bound TF diffuses while attached to a spring-like tether, which can be represented as diffusion in a harmonic potential well Figure 2.6A. The width of the harmonic well is related to the length of the flexible domain. The effective length is the full FG Nup length if the FG Nups are not crosslinked, while the effective length is reduced if they are crosslinked or entangled [39].

In order to calculate the bound diffusion coefficient of the TFs, an averaging procedure is followed. The diffusion is assumed to be Fickian, which is a reasonably good though not perfect assumption. (See discussion in Sec. 2.5.) In the Fickian diffusion case, the diffusion coefficient is proportional to a mean-squared displacement (MSD) divided by time. We calculate the mean binding lifetime τ and the MSD corresponding to this “typical” binding event and divide them.

To begin, note that the duration of a binding event follows the exponential distribution

$$\rho(t) = \exp(-t/\tau)/\tau, \quad (2.17)$$

where $\tau = 1/k_{\text{off}}$ is the mean binding lifetime.

Next, the positional probability density of a bound TF is

$$P(x, t) = e^{-\frac{x^2}{2\alpha(t)}} / \sqrt{2\pi\alpha(t)}, \quad (2.18)$$

$$\alpha(t) = (1 - e^{-2kD_F\beta t})/(k\beta) \quad (2.19)$$

where k is the spring constant of FG Nup tethering and $1/\beta = k_B T$ is the thermal energy [115].

The center of the well is set at $x = 0$.

The mean-squared displacement (MSD) of the TF as a function of time is calculated, as any expected value, with the integral

$$\langle x^2(t) \rangle = \int_{-\infty}^{\infty} P(x, t)x^2 dx = \alpha(t). \quad (2.20)$$

Finally, the typical TF MSD during a binding event can be determined by evaluating

$$\overline{\langle x^2 \rangle} = \int_0^{\infty} \rho(t') \langle x^2(t') \rangle dt' = \frac{2D_F L_c \ell_p}{L_c \ell_p k_{\text{off}} + 3D_F}. \quad (2.21)$$

Here we assume that the spring constant is that of a worm-like chain polymer $k = 3/(2\beta L_c \ell_p)$, where L_c is the contour length and ℓ_p the persistence length [114].

Combining these results, the one-dimensional bound diffusion coefficient is

$$D_B \approx \frac{\overline{\langle x^2 \rangle}}{2\tau} = \frac{D_F L_c \ell_p k_{\text{off}}}{L_c \ell_p k_{\text{off}} + 3D_F} = \frac{D_F}{1 + 3\frac{D_F}{D_P}}. \quad (2.22)$$

Here $D_P = L_c \ell_p k_{\text{off}}$ controls the bound-state diffusion coefficient: higher D_P corresponds to a lower constraint of the TF by the tether and greater bound mobility. Bound mobility increases with increasing chain length and persistence length, or decreasing binding lifetime. When D_P is large ($D_F/D_P \ll 1$), D_B approaches D_F , since the long chains barely affect TF motion during the short binding event. For small D_P ($D_F/D_P \gg 1$), TF motion is inhibited by a short tether, giving $D_B \approx D_P/3 \ll D_F$.

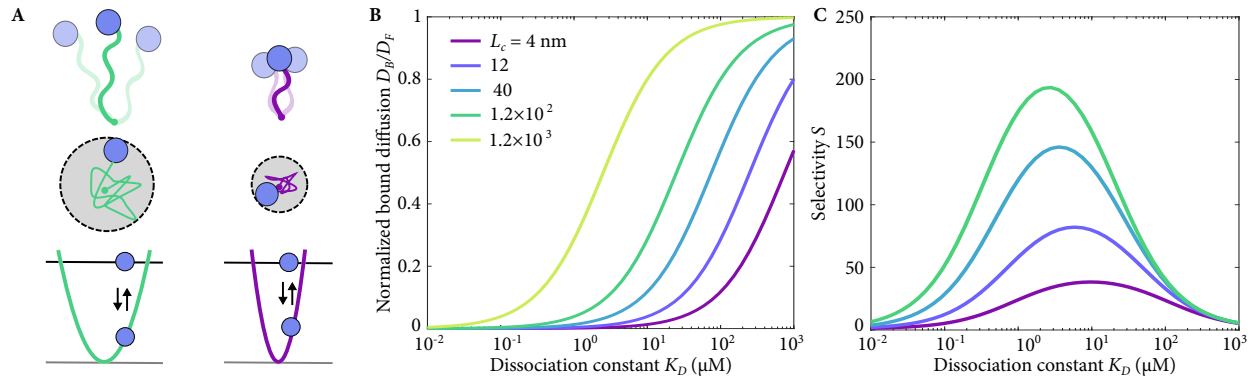


Figure 2.6: (A) Schematic of the flexible tether model of bound-state diffusion. FG Nups are treated as entropic springs that constrain the motion of TFs more (top and center left, longer FG Nup) or less (top and center right, shorter Nup), which corresponds to changing width of the harmonic potential well (lower). (B) Ratio of bound to free diffusion coefficient as a function of dissociation constant, with varying polymer length in the tethered-diffusion model. (C) Selectivity as a function of K_D , with varying polymer length in the tethered-diffusion model. Selectivity calculated by Mike Stefferson.

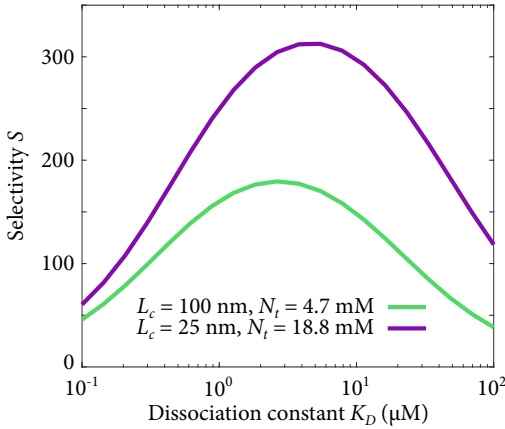


Figure 2.7: Selectivity as a function of dissociation constant in the tethered diffusion model, varying Nup contour length L_c and total Nup concentration N_t . The product $L_c N_t$ is held constant.

Physiological values can be estimated for all of the relevant parameters. Disordered proteins are relatively flexible, with persistence lengths around $\ell_p \approx 1 \text{ nm}$ [116]. The contour lengths of the disordered regions of FG Nups are in the range $L_c \approx 100\text{--}280 \text{ nm}$ (250–700 amino acids long [8] with a contour length per amino acid $\approx 0.4 \text{ nm}$).

Using these parameters, along with those described in earlier sections, Mike Stefferson calculated the selectivity due to tethered diffusion for several tether lengths (Fig. 2.6C). Selectivity was also calculated for two values of the total Nup concentration N_t , mimicking the possible effect of Nup crosslinking within the pore (Fig 2.7. The produce of contour length and Nup concentration $L_c N_t$ was held constant, and selectivity calculated for a long Nup length of 100 nm as well as a shorter length of 25 nm, reflecting the possibility of crosslinking. Corresponding total Nup concentrations of 4.7 and 18.8 nm, respectively, were determined from an estimate of the number of TF binding sites (800), and the volume of a cylinder of diameter 60 nm and length $L = 100 \text{ nm}$.

Using these realistic parameters, selectivity can reach 200–300, a large flux enhancement for TFs over nonbinding proteins.

2.4 Bound mobility through inter-chain hopping

Another possible mechanism of bound-state diffusion is inter-chain hopping enabled by multivalent binding interactions. All known transport factors have at least two hydrophobic binding pockets which bind to FG motifs, and some have many more [56]. FG Nups in turn each pos-

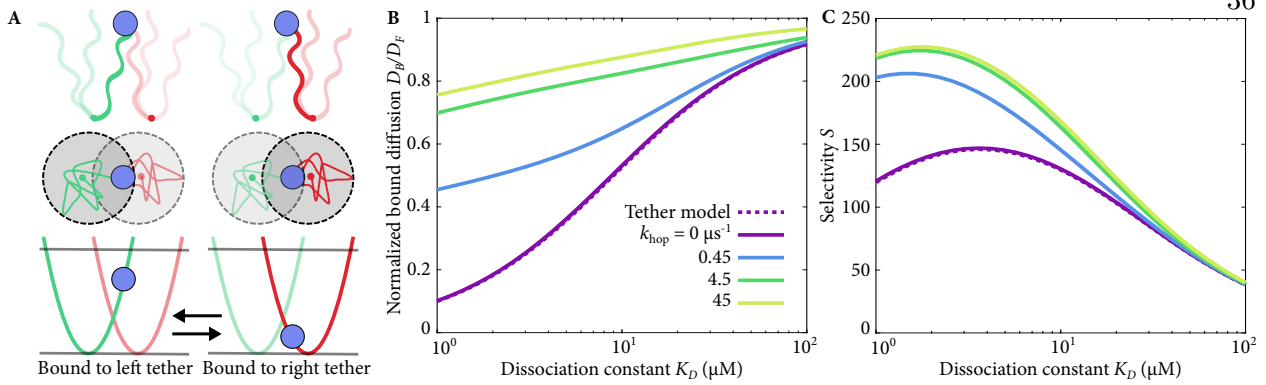


Figure 2.8: (A) Schematic of the inter-chain hopping model of bound-state diffusion. FG Nups are treated as entropic springs that constrain the motion of TFs, and inter-chain hopping allows a TF to move from one FG Nup (top and center left, green Nup) to another (top and center right, red Nup) without unbinding, which corresponds to switching from one harmonic potential well to another (lower). (B) Ratio of bound to free diffusion coefficient as a function of dissociation constant, with varying hopping rate in the inter-chain hopping model. (C) Selectivity as a function of K_D with varying hopping rate. FG Nup contour length $L_c = 40 \text{ nm}$ in (B, C).

sess many FG motifs, leading to a highly multivalent binding interaction. This feature allows a transport factor to bind to multiple Nups at once, moving between them with a hand-over-hand or sliding motion without ever fully unbinding [63, 85]. While binding to multiple FG motifs on the same Nup will not lead to bound diffusion, inter-chain hopping will cause the origin site of tethered transport factor diffusion to change over time. In order to understand the effect of hopping on the overall bound diffusion constant, we model a TF that undergoes tethered diffusion when bound to an FG Nup and hops between neighboring, randomly distributed tethers Figure 2.8.

In our simulation of TF motion with hopping between FG Nups while bound, we represented each FG Nup as an entropic spring (i.e. as a harmonic potential well). Well positions were randomly chosen from a uniform distribution, with the exception that we always placed one well at the starting position of the TF. The particle (the TF) started the simulation bound to this FG Nup, and remained bound throughout the simulation. While bound to one FG Nup, the TF diffused within the harmonic well representing that FG Nup. We recorded the position and mean-squared displacement of the TF from its starting location, which we then used to determine a bound diffusion coefficient, as described in more detail below. The TF could hop between tethers by changing which well it moved in.

The source code of the hopping simulation is available at <https://github.com/LauraMaguire/hoppingSim>.

2.4.1 Diffusion in a potential well

The TF moved in the harmonic potential of the FG Nup according to Brownian dynamics. At each timestep, the TF position was updated using a force-dependent diffusive step [117].

$$x(t + \delta t) = x(t) + \frac{F}{\Gamma} \delta t + \delta x, \quad (2.23)$$

where F is the force acting on the particle, Γ is the drag coefficient, δt is the timestep, and δx is a random Brownian step drawn from a Gaussian distribution with variance $\sigma^2 = 2D\delta t$. The drag coefficient of a spherical particle at low Reynolds number is given by Stokes' Law as $\Gamma = 6\pi\eta r$, where η is the fluid's viscosity and r is the sphere's radius. This result can be combined with the Einstein relation $D = k_B T / (6\pi\eta r)$ to give

$$\Gamma = \frac{k_B T}{D}. \quad (2.24)$$

The force $F = -k\Delta x$, where k is the spring constant of the FG Nup and Δx is the displacement of the particle from the Nup attachment point. We model the FG Nup as a worm-like-chain at small extension, so that $k = 3k_B T / (2\ell_p L_c)$, where ℓ_p is the tether persistence length and L_c is the contour length. Then

$$x(t + \delta t) = x(t) - \frac{3D\Delta x \delta t}{2\ell_p L_c} + \delta x = x(t) - DK\Delta x \delta t + \delta x, \quad (2.25)$$

where K is the normalized spring constant $K = k/k_B T = 3/(2\ell_p L_c)$.

2.4.2 Hopping probability

We designed the hopping probability P_{hop} in order to satisfy the principle of detailed balance. During every iteration of the simulation, we picked an FG Nup at random from a list of the M Nups near enough to have a reasonable probability of hopping. TF hopping to the new FG Nup

was attempted with success probability

$$P_{\text{hop}} = r_{\text{hop}} M \delta t e^{-\Delta G/2}. \quad (2.26)$$

Here the base hopping rate r_{hop} is a dimensionless input parameter, and the change in free energy (in units of $k_B T$) between the current Nup and the proposed new Nup is

$$\Delta G = \frac{1}{2} K(x - x_{\text{new}})^2 - \frac{1}{2} K(x - x_{\text{cur}})^2, \quad (2.27)$$

where K is the normalized spring constant, x is the particle's current position, x_{cur} is the anchor location of the Nup to which the particle is currently bound, and x_{new} is the anchor location of the proposed new Nup. Note that when a hop succeeds, the energy landscape changes to that of the new Nup, but the TF's position does not change during the hop. There is no upper bound on P_{hop} , but we adjusted the timestep to ensure that P_{hop} was greater than unity no more than 0.5% of the time that a hop was attempted.

2.4.3 Mean-squared displacement and diffusion coefficient calculation

We ran each simulation for 10^7 time steps with $\delta t = 0.01 \mu\text{s}$, and recorded the particle's position every 100 time steps. We calculated the mean-squared displacement $\langle x^2 \rangle$ (MSD) of the TF and averaged it over 100 runs Figure 2.9A. We then computed

$$\rho_{\text{MSD}}(t) = \langle x^2(t) \rangle \rho(k_{\text{off}}, t) = k_{\text{off}} \langle x^2(t) \rangle e^{-k_{\text{off}} t}, \quad (2.28)$$

as shown in fig. 2.9B, and numerically integrated the distribution in time. We determined the bound diffusion coefficient from the typical MSD-per-binding-event $\overline{\langle x^2 \rangle}$ using

$$D_B = \frac{k_{\text{off}} \overline{\langle x^2 \rangle}}{2}. \quad (2.29)$$

Here, the factor of 1/2 is appropriate because we consider a one-dimensional random walk.

2.4.4 Bound diffusion and selectivity from hopping simulation

Upon calculating the bound diffusion constant using the hopping simulation described above, it was clear that inter-chain hopping could lead to relatively large bound diffusion constant, with

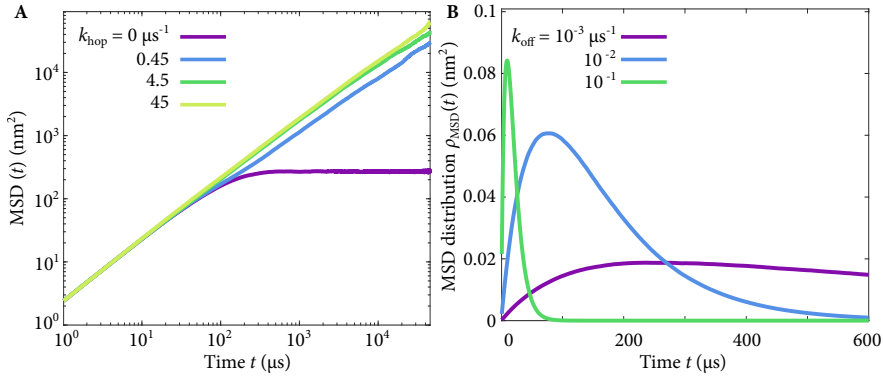


Figure 2.9: (A) Examples of mean-squared displacement (MSD) of a simulated TF in the inter-chain hopping model, with varying hopping rate. (B) Examples of MSD distributions $\rho_{\text{MSD}}(t)$ used in estimating the diffusion coefficient, with varying unbinding rate. Tethers have 40 nm contour length; other parameters are as discussed in the text.

a corresponding increase in selectivity (Figs. 2.8, 2.10). In the limit of a hopping rate of zero, the tethered-diffusion-only result is recovered, as anticipated. Hopping most enhances selectivity when the Nup length or dissociation constant are small. This is the regime where tethered diffusion is limited, corresponding to crosslinked Nups within the nuclear pore. If the pore is highly crosslinked, binding multivalency may be essential to selectivity.

2.5 Fickian and anomalous diffusion

A particle whose mean-squared displacement is proportional to time ($\langle x^2(t) \rangle \propto t$) is said to be undergoing normal or Fickian diffusion. This is generally the case for a freely-diffusion particle with no driving forces acting upon it. Anomalous diffusion is the more general case where $\langle x^2(t) \rangle \propto t^\alpha$. When $\alpha > 1$, the motion is superdiffusive; $\alpha < 1$ is the subdiffusive regime, typically caused by confined diffusion or binding.

Throughout this analysis, we have assumed that all proteins are experiencing Fickian diffusion. For inert, nonbinding proteins, this is true provided we neglect any steric confinement from the presence of the FG Nups. Additionally, transport factors should show normal diffusion over timescales much longer than their binding lifetime. However, binding interactions will result in slightly subdiffusive motion on shorter timescales.

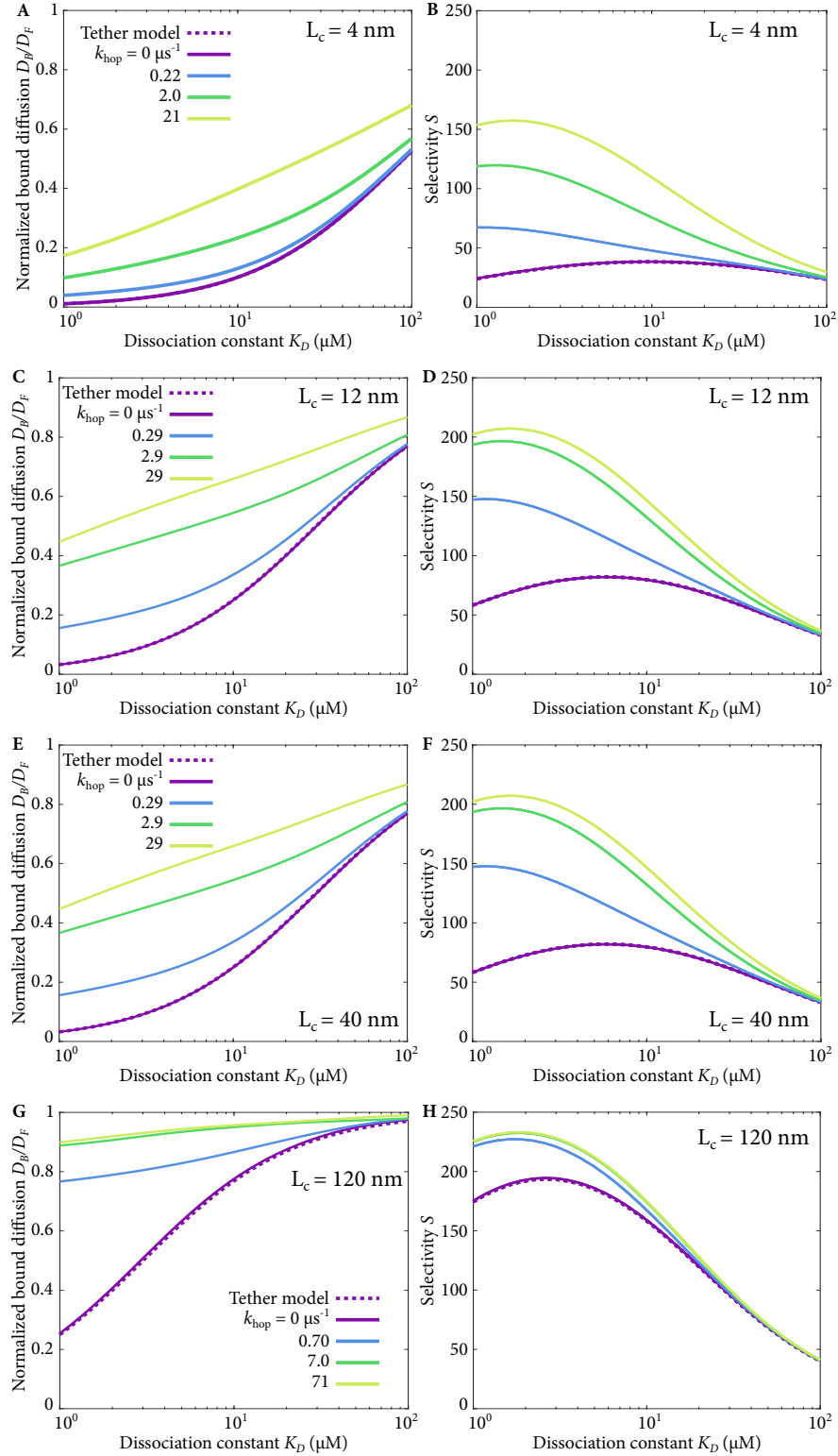


Figure 2.10: Bound diffusion and selectivity as a function of dissociation constant, with varying hopping rate for FG Nups with (A,B) $L_c = 4 \text{ nm}$; (C,D) $L_c = 12 \text{ nm}$; (E,F) $L_c = 40 \text{ nm}$; (G,H) $L_c = 120 \text{ nm}$.

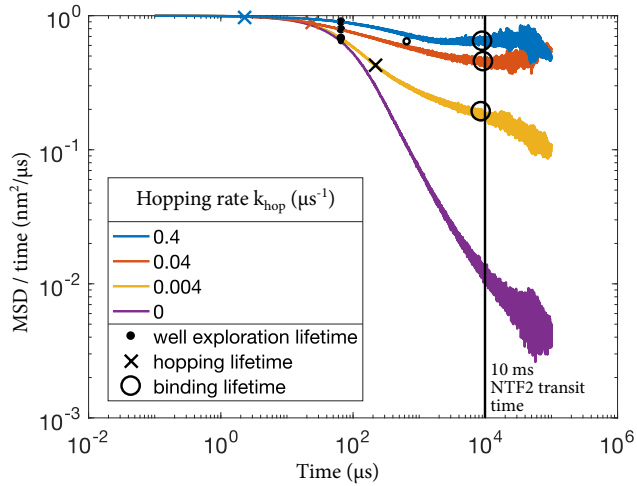


Figure 2.11: Anomalous diffusion of transport factors at several hopping rates. The hopping, binding, and well-exploration lifetimes are also shown where applicable. NTF2 transit time (10 ms) is indicated with a vertical line.

In order to quantify the extent of anomalous diffusion, we ran a modified version of the hopping simulation described in Sec. 2.4 in which the transport factor was not solely limited to hopping but also able to entirely unbind from and rebind to Nups with rates k_{off} and k_{on} respectively.

In order to quantify the extent of anomalous diffusion, we ran the same simulations described above but allowed total unbinding and rebinding to occur, not just hopping while bound. The resulting MSD $\langle x^2(t) \rangle$ can then be used to investigate anomalous diffusion. Figure 2.11 is a log-log plot of $\langle x^2(t) \rangle / t$ vs time t , generated using a script created by Mike Stefferson [106]. In such a plot, a horizontal asymptote indicates Fickian diffusion, while a non-zero slope m indicates anomalous diffusion with $m = \alpha - 1$.

Figure 2.11 shows several hopping rates. When the transport factor is not able to hop between Nups, diffusion remains anomalous until well past the binding lifetime $1/k_{\text{off}}$ (not shown). Larger hopping rates cause diffusion to become Fickian over shorter timescales. The hopping lifetime $1/k_{\text{hop}}$ is shown for each nonzero hopping rate, as well as the binding lifetime ($k_{\text{off}} = 10^{-4} \mu\text{s}$ in all cases). The time to explore the potential well caused by binding to Nups is also shown. The vertical line marks the experimentally-measured time for NTF2 to pass through the nuclear pore, $t_{\text{NTF2}} = 10 \text{ ms}$.

The anomalous diffusion plot indicates that the diffusion of transport factors is not entirely Fickian, but that shorter binding lifetimes and higher hopping rates lead to less anomalous diffusion.

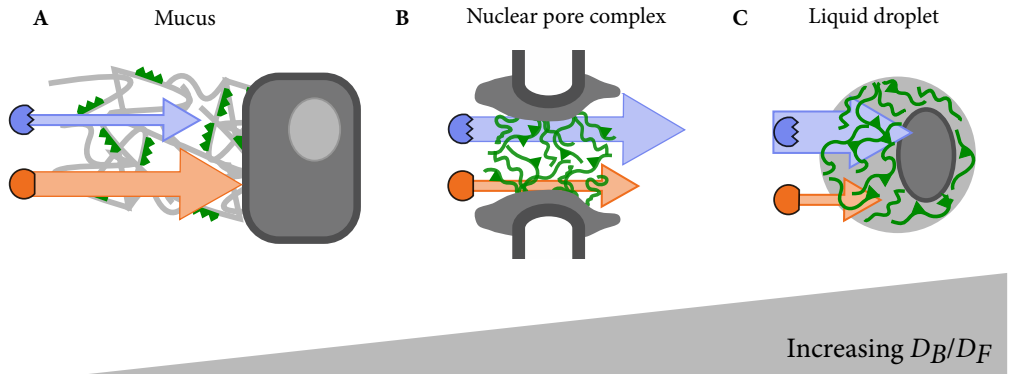


Figure 2.12: Possible effect of bound diffusion on other biological systems.

2.6 Bound diffusion in other biological systems

While the above model was inspired by nuclear transport, it is sufficiently general that it can be applied to other biological systems as well. A variety of selective filters exist *in vivo*, and bound-state diffusion could be relevant to many of them. Our model predicts that higher bound diffusion will lead to higher selectivity in biofilters.

Figure 2.12 shows three biofilters ordered by increasing bound-to-free diffusion ratio (D_B/D_F). Mucus, such as the mucus which lines the lungs, permits very little bound diffusion of particles that bind to it. Research in targeted drug delivery to lung cells has observed that inert nanoparticles are more effective at penetrating the mucus barrier than binding particles [73]. This observation agrees with the prediction that binding will only enhance transport if bound diffusion occurs. On the other hand, Fig 2.12C depicts a system with maximal bound-state diffusion: a phase-separated liquid droplet. Such a droplet, consisting of a phase rich in an intrinsically disordered protein, may be used in order to concentrate binding partners and speed up reactions within the cell [6, 93]. In this case, complexes of IDPs and their binding partners would have approximately the same diffusion constant as free binding partners ($D_B/D_F \approx 1$), leading to high selectivity for binding partners to pass to the center of the droplet.

Systems other than filters may make use of principles found in our model as well. For example, the bacteria *Staphylococcus aureus*, responsible for many antibiotic-resistant infections in hospitals,

can exhibit resistance to the antibiotic vancomycin by constantly building and shedding its cell wall, to which vancomycin binds [118]. Our model predicts that such a strategy should keep the vancomycin flux through the cell wall from reaching steady-state, in the transient regime where the flux of a binding molecule is suppressed (Fig. 2.2). The targeting of the DNA damage repair protein PARP1 to appropriate sites in the nucleus, described below, is another potential application of binding and diffusion principles.

2.6.1 DNA damage repair protein recruitment in the nucleus

Poly(ADP-ribose) polymerase 1 (PARP1) is a protein which assists in DNA damage repair. Within the nucleus, it rapidly diffuses to and tightly binds damaged DNA, despite the presence of large amounts of undamaged DNA, for which PARP1 also has a measurable affinity [90, 91]. Very little free PARP1 is believed to exist within the nucleus. Therefore, the rapid migration of PARP1 to damaged DNA must be dependent on bound-state mobility.

Both mechanisms discussed here for the nuclear pore could potentially apply to PARP1 as well. Johannes Rudolph, Jyothi Mahadevan, and Karolin Lugar have demonstrated the existence a multivalent “monkey-bar” mechanism equivalent to inter-chain hopping between DNA strands [91]. However, disruption of this mechanism reduces PARP1 diffusion by approximately 10% only, indicating that there are more methods of bound diffusion available to PARP1 [92]

Either tethered diffusion or additional hopping might provide the missing bound-state mobility. To begin, assume that tethered diffusion is the only additional mechanism of bound diffusion. The predicted off-rate k_{off} of PARP1 from undamaged DNA can then be calculated assuming that the effective diffusion constant of PARP1 observed in the nucleus is $D_{\text{obs}} = p_b D_B + (1 - p_b) D_F$, a weighted average of free and bound diffusion constants where p_b is the fraction of PARP1 bound. If bound diffusion comes only from tethered motion, then D_B is given by Eqn. 2.22. The fraction of PARP1 bound in chemical equilibrium is

$$p_B = \frac{1}{1 + \frac{K_D}{N_T}} \quad (2.30)$$

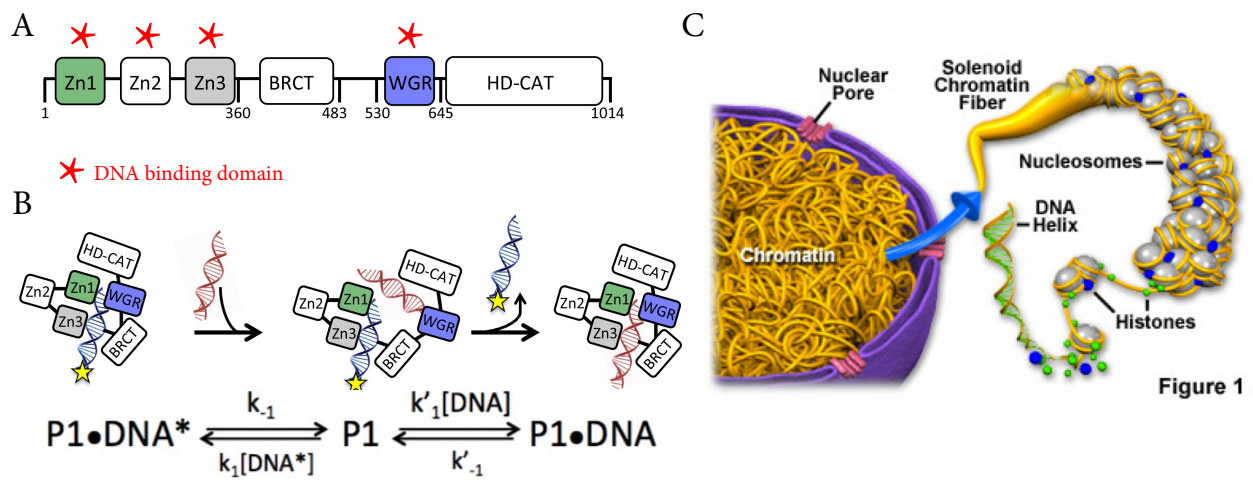


Figure 2.13: PARP1 and its possible mechanisms of bound diffusion. (A) Schematic of PARP1 structure showing its four DNA-binding domains [91]. (B) “Monkey-bar” inter-strand hopping mechanism cartoon and reaction showing on- and off- rates for binding two subsequent DNA strands [91]. (C) Flexible tether structure of chromatin within the nucleus. (Image from Florida State University.)

where $K_D = k_{\text{off}}/k_{\text{on}}$ is the dissociation constant and N_T is the total concentration of PARP1 binding sites on undamaged chromatin (assuming low occupancy by PARP1).

The polymer properties of chromatin are estimated from single-molecule force spectroscopy as $L_c \ell_p = 2.5 \times 10^{-4} \mu\text{m} - 1.2 \times 10^{-5} \mu\text{m}$ [119, 120]. Johannes Rudolph estimates a diffusion-limited on-rate of $k_{\text{on}} = 10^9 \text{ M}^{-1} \text{ s}^{-1}$ and a total binding site concentration of up to 1 mM. Finally, measurements of PARP1 diffusion in the nucleus and in buffer give $D_{\text{obs}} \approx 3 \mu\text{m/s}^2$ and an upper bound of $D_F = 9D_{\text{obs}}$ [92]. Using these parameters, we predict that an off-rate between 1.2×10^2 and $1.2 \times 10^3 \text{ s}^{-1}$ would account for the observed diffusion. This off-rate is larger than the commonly accepted range, but not absurd [91].

Apart from tethered diffusion, there could be a second mechanism of inter-strand hopping at work. PARP1 contains four DNA binding domains (Fig. 2.13A), and though some may work in tandem, it is possible that additional multivalent interactions are taking place beyond the monkey-bar mechanism. Analytic models of hopping are more complicated [67], but a highly-simplified model can be used to estimate the maximum expected contribution to bound diffusion from hopping. Using the reaction scheme described in Fig. 2.13B, assume that every time a second strand of DNA binds, PARP1 takes a “step” of approximately its own size. The bound diffusion constant would then be on the order of $D_B \sim R^2 k_{\text{on}} N_T$ where R is the size of PARP1. Using the parameters above, and taking $R \approx 5 \text{ nm}$, we have $D_B \approx 1 \mu\text{m}^2/\text{s}$. However, given the high concentration of chromatin in the nucleus, the upper bound on bound-state diffusion from hopping can be estimated assuming that there is always a second strand of DNA “within reach” of PARP1, i.e. that the binding-site number density is $\rho \approx 1 \text{ molecule}/(5 \text{ nm})^3$. This assumption leads to a molar concentration [DNA] = 13 mM and a bound diffusion constant $D_B \approx 100 \mu\text{m}^2/\text{s}$.

Using these order-of-magnitude calculations, either tethered diffusion or hopping could provide enough bound-state mobility to explain the rapid diffusion of PARP1 to sites of DNA damage within the nucleus.

2.7 Conclusions

In the above chapter, we have developed a simple model of selective nuclear transport which may apply more broadly to other biofilters as well. Remarkably, this simple model can reproduce the high selectivity shown experimentally by the nuclear pore for proteins which can bind to the filter. The diffusion coefficient of the bound complex proved to be the most important factor in predicting selectivity. In order to test the predictions of our model, we next began developing nuclear-pore-inspired biofilters to investigate the effect of bound-state diffusion on protein separation *in vitro*.

Chapter 3

Hydrogel design for protein separation

In order to test the predictions of our bound-state diffusion model of selectivity, we needed to develop a biomaterial that could support bound diffusion and be used to test selectivity. There are several biological examples which show selectivity that could be explained by bound-state diffusion, including nucleocytoplasmic transport, liquid-liquid phase separated droplets, diffusion of DNA-damage-repair proteins in the nucleus, and passage through mucus [73, 91, 121, 122]. We decided to focus on making a material that mimics the environment of the nuclear pore.

One of the attractions of the bound-state diffusion model is that it does not rely on the geometry of the selective material. As long as the dimensions of the material are significantly larger than the protein diffusing through it, there is no practical difference between a nanoscale cylindrical pore and a macroscale bulk material. For ease of fabrication and testing, we opted to design a bulk material for protein separation.

A hydrogel substrate was chosen as the basis of the nuclear pore mimic and protein fragments taken from FG Nups anchored into it. Hydrogels are versatile materials, many of which are biocompatible, many of whose properties can be easily tuned. We used a hydrogel substrate to provide an inert scaffold to which fragments of FG Nups were conjugated. These Nups were conjugated to the hydrogel at one end and free at the other, mimicking the arrangement found in the nuclear pore and providing a mechanism of tethered bound diffusion. The properties of these Nups, such as their length, number of transport factor binding motifs, and propensity towards aggregation, can be easily varied in order to test how these properties impact bound-state diffusion and thus

protein selectivity.

This hydrogel model is therefore the simplest way to make a material to explore the effects of bound diffusion on protein separation. While it is inspired by the nuclear pore, the goal is not to directly reproduce the mechanism of nucleocytoplasmic transport. Instead, we hoped to show that bound-state diffusion was measurable and controllable in a biomaterial, paving the way for molecular filters that might make use of this principle.

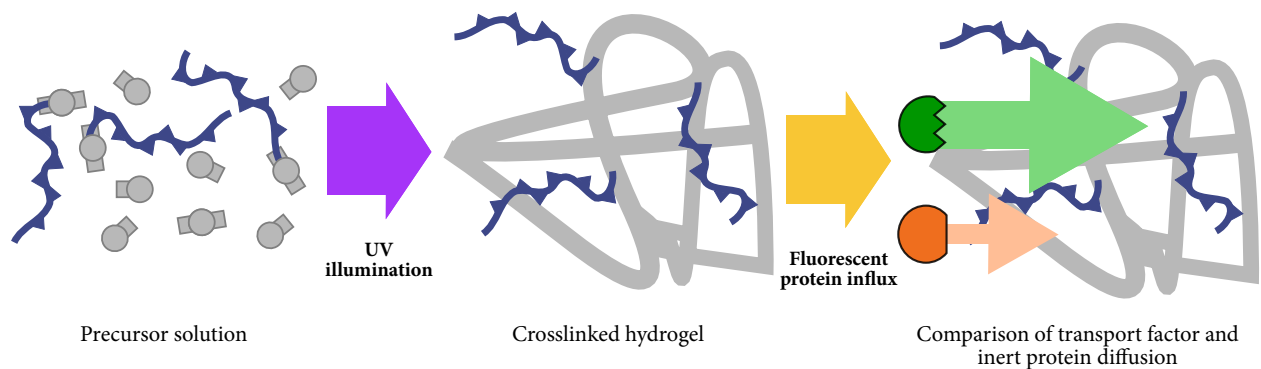
Over the course of making these materials, we ran into several significant roadblocks. Although hydrogels with a wide range of properties have been well-studied, gels suitable for protein separation are harder to come by. They require an intermediate pore size, large enough that the diffusion of a protein is not significantly hindered by the presence of the hydrogel meshwork, but small enough that the Nup peptides can easily reach the protein as it diffuses. This average pore size of 5-20 nm is difficult to find, though much smaller and much larger pores are easy to make. The problem of pore size is made more difficult by the need to create a well-sealed hydrogel barrier in order to separate proteins; such a barrier must necessarily be confined and therefore unable to swell to its equilibrium size. The creation of a hydrogel for selective protein separation poses many stringent requirements, often in competition with each other. This chapter describes the setbacks we faced and the progress we have made towards creating a hydrogel-based biomaterial suitable for selective separation of proteins.

3.1 Hydrogel fabrication

A wide range of hydrogels systems have been well-studied. Many are not suitable for the addition of proteins, but both PEG and acrylamide hydrogels, among others, can be crosslinked in an aqueous solution that does not harm proteins. We used both PEG and acrylamide hydrogels in our diffusion experiments. Thanks to Stephanie Bryant, Sadhana Sharma, Christopher Bowman, Danielle Konetski, and Benjamin Fairbanks for their help as we learned to make these hydrogels.

Whether using PEG or acrylamide, the basic hydrogel fabrication procedure was the same (Fig. 3.1). First, a precursor solution was mixed, which contained the hydrogel monomer, a

Figure 3.1: Overview of hydrogel fabrication and fluorescent protein influx. A precursor solution is mixed, containing hydrogel monomers, crosslinkers, a photoinitiator, and the Nup fragment. Upon exposure to UV light, the precursor solution crosslinks, and one end of each Nup is conjugated to the hydrogel. The diffusion of a fluorescently-tagged transport factor can then be compared to that of a similarly-sized inert fluorescent protein.



crosslinker, a radical generator, and the Nup fragment, labeled with a reactive group at one end that would conjugate it to the hydrogel. The radical generator was almost always a photoinitiator, which caused the precursor solution to crosslink when exposed to UV illumination. In a few cases, a chemical initiator was used, in which case the precursor solution crosslinked 10-30 minutes after mixing. By the end of the crosslinking process, the hydrogel contained Nup fragments tethered to the gel at one end, mimicking the arrangement of Nups in the nuclear pore and providing a mechanism of tethered bound diffusion for transport factors but not for non-binding inert proteins. The diffusion of both types of protein within the hydrogel could then be quantified using fluorescence microscopy. Detailed protocols and precursor solution recipes are reported in Appendix E.

There were four major components to the precursor solution: monomers, crosslinkers, initiators, and Nup fragments. To an extent, these components can be tuned independently of each other. Bisacrylamide or PEG-diacrylate crosslinkers must be used with acrylamide monomers, and PEG-dithiol crosslinkers with PEG-norbornene monomers, but the initiators and Nup fragments can be varied. There are many variations on crosslinker length as well, leading to a wide variety of possible hydrogels even using a relatively small set of components.

The PEG hydrogels made use of 20-kD 8-armed PEG-norbornene monomers (synthesized by the Bryant lab and Nathan Crossette) and either a 1-kD or 8-kD PEG-dithiol crosslinker (Sigma) (Fig. 3.2). To conjugate the Nup fragment to the PEG hydrogels, a C-terminal cysteine was added to the peptide. Both the crosslinker and Nup fragment made use of Michael-thiol “click” chemistry [123] [124].

The acrylamide hydrogels used an acrylamide monomer and bisacrylamide crosslinker (Bio-Rad) (Fig. 3.2). An additional step was needed to prepare the Nup fragment for tethering to the hydrogel: either bisacrylamide or 700-Da PEG-diacrylate (Sigma) was conjugated to the terminal cysteine (see Appendix D).

Regardless of the monomers and crosslinkers used, a radical generator is needed to initiate polymerization. We used either a photoinitiator, activated by UV light, or a chemical initiator system which began polymerization upon its addition to the precursor solution. Both systems have

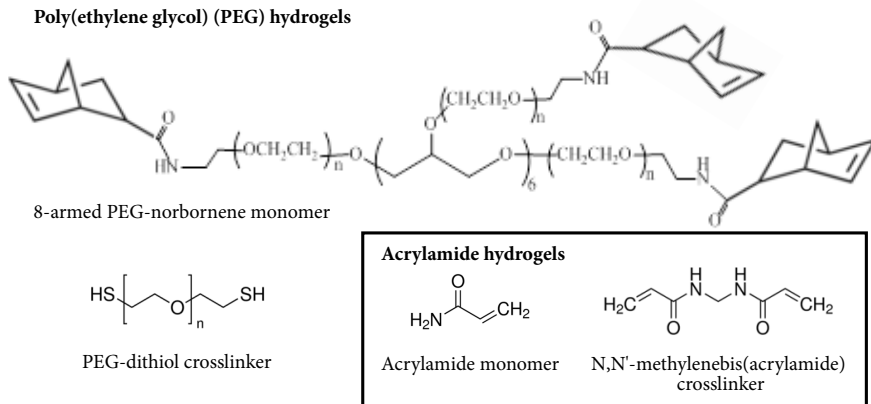


Figure 3.2: Chemical structures of monomers and crosslinkers for PEG and acrylamide hydrogels. The total molecular weight of the 8-armed PEG-norbornene was 20 kD, and either a 1-kD or 8-kD PEG dithiol crosslinker was used. Structures from Sigma and CreativePEG-Works.

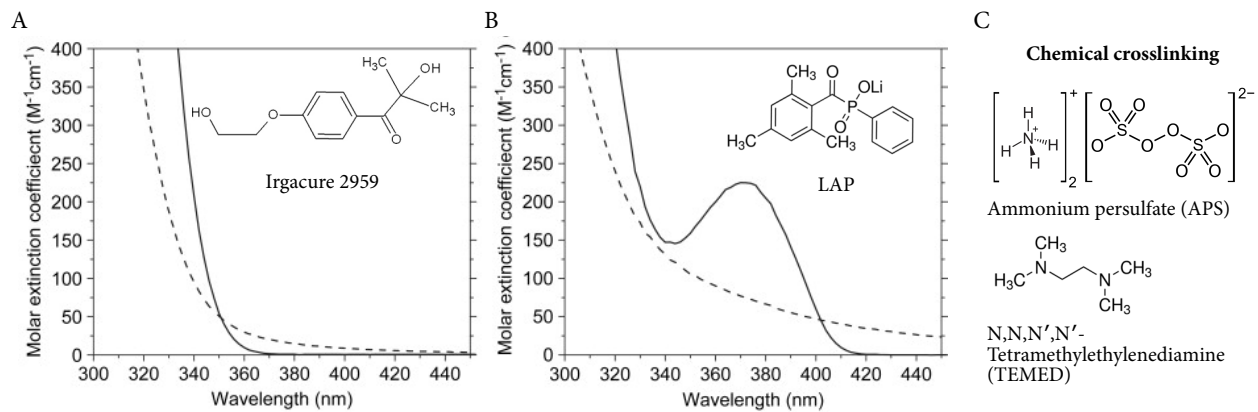
advantages: Photoinitiators are useful for patterned polymerization using photomasks and allow the precursor to be mixed prior to polymerization, while chemical crosslinkers do not require careful protection from light. We nearly always used a photoinitiator.

Two photoinitiators were tested: 1-[4-(2-hydroxyethoxy)-phenyl]-2-hydroxy-2-methyl-1-propane-1-one (commercially known as Irgacure 2959) and lithium phenyl-2,4,6-trimethylbenzoylphosphinate (LAP). Figure 3.3 (A) and (B) shows the absorption spectra of each photoinitiator and that of its cleavage products [125]. LAP has an absorbance peak in the near-IR / violet range, is highly water-soluble, and is more effective at crosslinking, so it was used most of the time. However, due to its absorbance into the visible range, care must be taken to protect solutions containing LAP from ambient light wherever possible. Our LAP was synthesized by the Bryant lab, but it is now commercially available from Sigma as well.

An APS/TEMED chemical crosslinking system was occasionally used in place of the photoinitiator. Large numbers of hydrogels can be polymerized at once in this way, without the need for a large area of uniform UV illumination. Figure 3.3 (C) gives the chemical structure of ammonium persulfate (APS) and N,N,N,N-tetramethylethylenediamine (TEMED). APS is the radical generator, and TEMED accelerates the radical formation. The time to polymerize can be controlled by adjusting the concentration of both components (Appendix E).

It should be noted that the presence of oxygen inhibits all the initiators discussed above. Precursor solutions were degassed for 10 minutes before use in a vacuum desiccator and polymerized

Figure 3.3: Absorption spectra of (A) Irgacure 2959 and (B) LAP (solid lines) and with that of their cleavage products (dotted lines) [125]. (C) Chemical structures of the APS/TEMED crosslinking system. Structures from Sigma.



no more than 10 minutes after degassing.

When a photoinitiator was used, the hydrogels were polymerized using UV illumination at either 365 nm (ThorLabs M365LP1 mounted LED) or 405 nm (laser on Nikon A1R confocal microscope) inside flow chambers as described in Sec. 3.2. The typical intensity of the LED was 220 mW/cm² and the typical crosslinking time 30 s. Depending on the situation, photomasks were used to selectively expose regions of precursor to UV, or entire droplets of precursor solution were polymerized in an otherwise-empty chamber (Fig. 3.4). After crosslinking, hydrogels were rinsed with 10-100 times their volume with buffer and allowed to soak in fresh buffer solution overnight at 4°C in order to approach swelling equilibrium and remove any remaining precursor solution.

Following the buffer soak, typically a fluorescent solution of proteins was added to the gels. Usually this consisted of a transport factor (typically NTF2) and a similarly-sized inert protein (typically the red fluorescent protein mCherry). A typical experiment consisted of a video at 4x or 10x magnification of the hydrogel, reservoir chamber, and (if applicable) an outlet/inner reservoir which slowly accumulated protein as it passed through the gel. Experiments ranged from 1-24 hours, with 2 hours being the most common. Typical data produced was a plot of accumulation in the inner reservoir or hydrogel over the course of the experiment, as well as a concentration profile through the gel and inner reservoir. Experiments are described in greater detail in Chapter 4.

3.2 Flow chamber fabrication

The hydrogels were usually crosslinked in microfluidic flow chambers as shown in Fig. 3.5 (A). The thin chambers ensured that the top and bottom of the gel were sealed, so that transport factors and inert proteins could enter the gel only by diffusing into it. The small chamber size also reduced the quantity of transport factor and inert protein solution needed. Finally, the chambers were designed to be easily mounted on a microscope stage for recording experiments.

The basic flow chamber design consisted of an acrylic slide, patterned spacer or gasket, and coverslip, stacked and sealed together. Ports were almost always drilled in the plastic slide before chamber assembly, in order to allow the chamber to be filled and emptied. Several methods of

Figure 3.4: Procedure for photopolymerization with (A) or without (B) a photomask. (A) A flow chamber is filled with precursor solution. The photomask is placed to hide all areas that should not be crosslinked, and the chamber is exposed to UV illumination. Excess precursor solution is removed with a buffer rinse. (B) Microliter droplets of precursor solution are pipetted onto the slide surface before the chamber is assembled. After assembly, the chamber is exposed to UV illumination. The chamber is then filled with buffer.

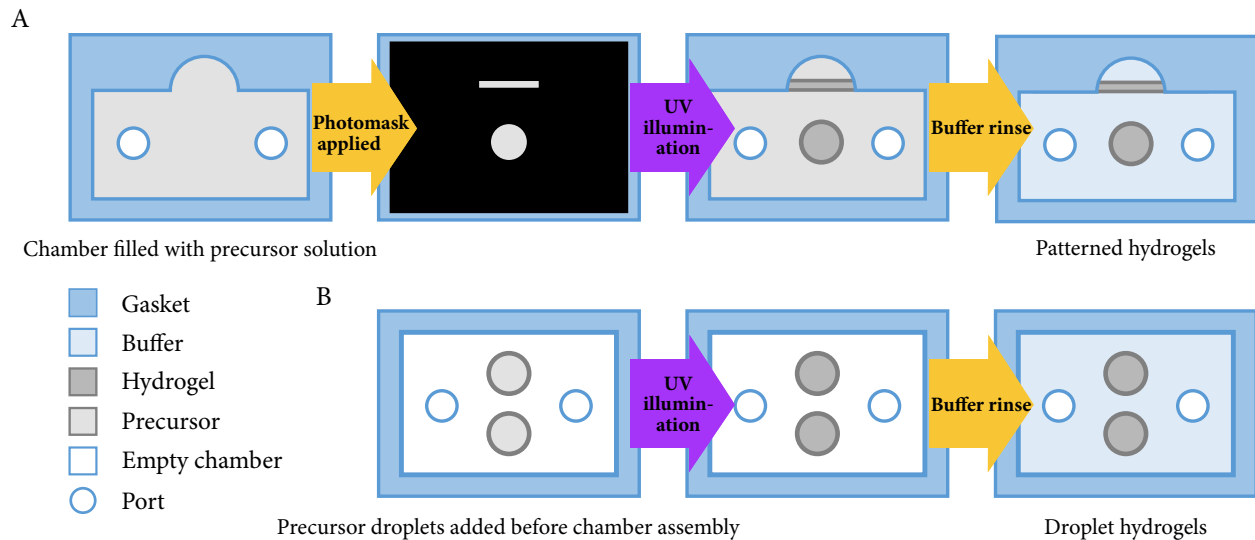
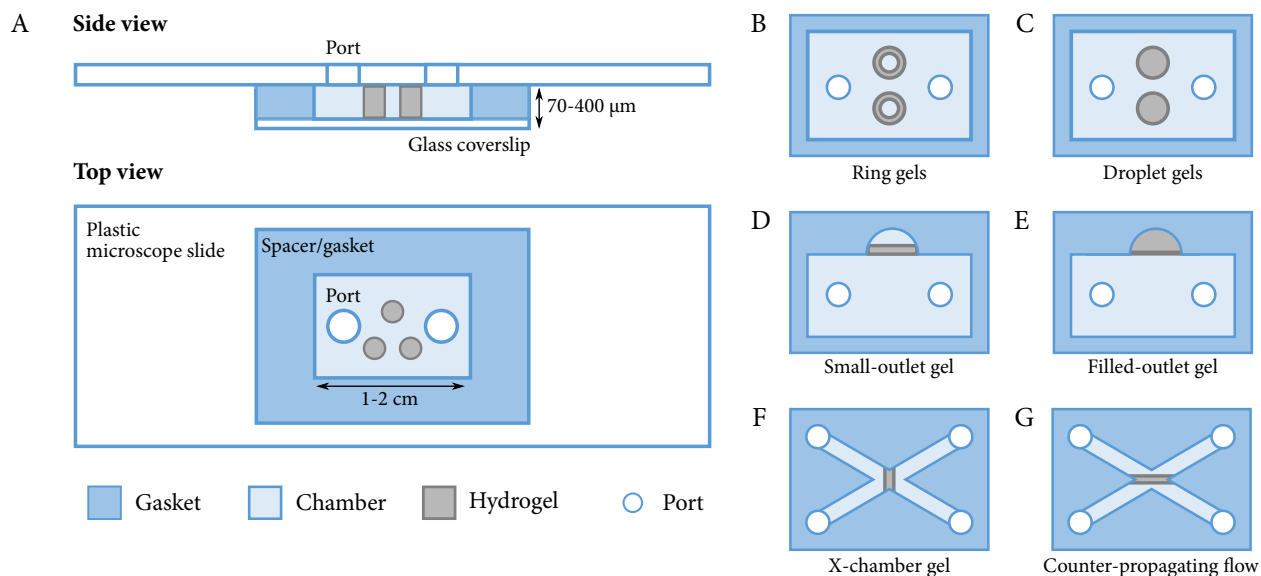


Figure 3.5: Flow chamber design and geometries. (A) Schematic of the most common flow chamber, showing slide, coverslip, gasket, ports, and hydrogels. (B)-(F) Common hydrogel geometries. Those in the left-hand column are suitable for selectivity measurements as well as diffusion measurements, while the right-hand column cannot be used to measure selectivity.



fabricating the gaskets and ports were tested in order to optimize the watertightness and longevity of the chambers as well as the ease of fabrication and re-use.

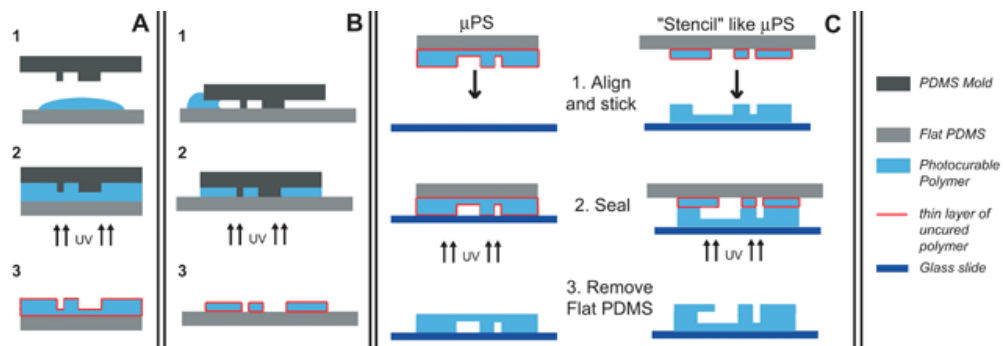
In particular, several materials were attempted for the gasket that determined the height and shape of the chamber. The simplest was double-stick tape, which could be used as a single width or cut into shape with a razor. The double-stick tape chambers were thin ($70\ \mu\text{m}$ per tape layer), of reliable thickness, and quick to make. However, they often leaked or dried over the course of several hours. Since many experiments take several days from preparation to finish, double-stick tape chambers were not usually not sufficient.

Norland Optical Adhesive (NOA), a liquid adhesive which cures upon exposure to UV, was used in another style of flow chamber. Thin semi-cured NOA layers can be molded and used as “stickers” to build flow chambers [126, 127]. This procedure is outlined in Fig. 3.6 and relies on the inhibition of curing by oxygen. A droplet of NOA is sandwiched between a glass coverslip and a PDMS mold, which is permeable to oxygen. The NOA is briefly (approximately 3 seconds at $220\ \text{mW/cm}^2$) cured, though a thin layer remains uncured due to the presence of oxygen at the adhesive’s surface. The PDMS mold is carefully peeled away, and the coverslip with NOA sticker is attached to the slide and sealed. The NOA is then fully cured and the chamber rinsed with ethanol to remove any uncured NOA remaining. Rather than applying NOA directly to the mold, as shown in Fig. 3.6 (A), it is also possible to seal the mold to the coverslip and wick NOA into the hollows (Fig. 3.6 (B)). This method is more error-prone and time-consuming but results in a flow chamber with glass on the top surface instead of NOA. Proteins are often less inclined to stick to the glass surface than to NOA.

PDMS molds for the NOA stickers were made with 0.5-mm resolution using a Silhouette Cameo craft cutter. After creating a template with the craft cutter’s software, the design was cut into a layer of packing tape that had been carefully applied to a large glass slide. The unwanted tape was peeled away using a razor and tweezers, leaving a depression where the chamber would eventually sit, and the slide used as the reverse-mold for a PDMS mold.

NOA-chambers are much more resistant to drying than double-stick-tape chambers, and can

Figure 3.6: Microfluidic sticker fabrication from [126]. (A) A PDMS mold is used to shape an NOA droplet on a flat slide. The NOA is briefly cured but retains a sticky surface. (B) NOA can also be wicked into a PDMS mold. (C) The NOA sticker is placed onto a permanent surface, sealed, and cured entirely.



withstand the largest pressure and most rapid flow. On the other hand, they are significantly more difficult to make and cannot be re-used. For most experiments, where rapid flow is not necessary, PDMS gaskets were the most useful. Chambers made with PDMS gaskets are thicker (100-400 μm) than the other varieties and their thickness is not as reproducible, but they are easy to reuse, often can last several days without drying out, and are quick to assemble.

PDMS gaskets were made by preparing the volume of PDMS mixture needed to create a layer of a given thickness in a standard Petri dish. Once the PDMS had been thoroughly mixed, degassed, and spread evenly across the dish, it was cured for an hour at 70° and cut into shape with a razor. Measurement with a micrometer indicated that the nominally 400- μm -thick PDMS film had an error of no more than 10%. This thickness proved to be optimal for sealing to both the acrylic slide and glass coverslip, as well as easily re-usable after thorough cleaning with ethanol.

While plasma-bonding the PDMS to the glass was tested, it proved unreliable. As long as the chamber was not subjected to high pressures, an adequate seal formed without additional treatment if all materials were cleaned with ethanol and dried with house air before use. Likewise, we attempted to silanate the glass in order to bond the hydrogel more securely to the top and bottom chamber surfaces, but it was not needed. The gels sealed well to the chamber as long as they were in contact with the surfaces while crosslinking. However, crosslinking the hydrogels on PDMS and then transferring them to the chamber resulted in a poor seal. In consequence, almost

all experiments were run using gels that had been crosslinked inside a chamber.

The ports were another point of concern for the watertightness of the chambers. If liquid needed to be flowed through a chamber at an appreciable speed, short lengths of PEEK tubing were superglued into the ports and fitted with Tygon tubing, which was then attached to a blunt-tipped syringe. For sufficiently gentle flows, however, ports were left simply as holes in the plastic slide and the chamber filled by pipette. After the chamber was filled, PEEK tubing ports were sealed with parafilm, and holes were sealed with a flat slab of clean PDMS.

Finally, portless thin chambers were used occasionally, such as for attempting fluorescence recovery after photobleaching (FRAP) using a confocal microscope. To make these chambers, microliter or smaller droplets of precursor solution containing 6- μm glass spacer beads were placed on glass slides and covered with a coverslip. The hydrogel was crosslinked and fluorescent protein solution wicked into the chamber. The chamber was sealed with valap (a 1:1:1 ratio of vaseline, lanolin, and paraffin which easily melts over a burner and re-solidifies rapidly). Such chambers last several hours on the microscope without drying but should not be used for longer experiments.

3.3 Hydrogel geometries

Our ultimate goal was testing protein separation by monitoring their passage into and through a selective material. In order to truly measure selectivity, the accumulation of proteins in an outlet reservoir beyond the test material must be measured, not just influx into the material. Many hydrogel and flow chamber geometries were tested in search of a setup that would allow selectivity, as well as free and bound diffusion, to be directly observed.

The limiting factors were the resolution of patterned hydrogel features, the size and accessibility of the outlets, and the equilibrium swelling of the hydrogels. Attempts to improve one of these factors typically led to worse outcomes for the others. Two major classes of hydrogel geometry emerged: those with an outlet reservoir, and those without. The hydrogels without an outlet reservoir cannot be used to directly measure the gels' selectivity, but diffusion constants for the inert protein and transport factors can still be determined. Chapter 4 details the results of

bound-state-diffusion experiments using no-outlet hydrogels.

The hydrogel geometries that contained an outlet reservoir are shown in Fig. 3.5 (B), (D), and (F). Ring-shaped gels (B) provide a small outlet reservoir, which is quick to equilibrate. They were fabricated using a confocal microscope (Sec. 3.8) or using PDMS molds 1-5 mm in diameter. While these rings would have been ideal for selectivity measurements, we were never able to work out a procedure that would result in artifact-free, well-sealed rings.

Fig. 3.5 (D) features a portless outlet reservoir which is much smaller than the inlet. As with the ring gels, these outlets are quick to equilibrate and their precise volume can be calculated, as the entire outlet is in the field of view of a 4x objective. A thin hydrogel bar was polymerized using a photomask, separating the inlet and outlet reservoirs. Without ports in the outlet, the chamber was soaked in buffer for 24 hours to remove the remaining precursor solution from the outlet. The inlet could then be filled with a fluorescent protein solution and accumulation in the outlet measured over time. Unfortunately, it's likely that the outlet itself was lightly crosslinked, no matter how carefully we used the photomask. See Sec. 3.8 for more evidence of stray crosslinking. Additionally, the hydrogel bars were of irreproducible thickness (50-200 μm) and swelled or buckled unpredictably. Ultimately, the lack of reproducibility between replicates made this geometry unusable.

Finally, Fig. 3.5 (F) shows an x-shaped chamber with four ports. A thin bar of hydrogel was polymerized at the junction of the arms using a photomask. The inlet and outlet reservoirs are approximately the same size, leading to slow equilibration in the outlet. The precise volume of the outlet is impossible to determine, as the arms are usually partly filled. Additionally, these chambers must be made using NOA stickers, which are difficult to use, and they tend to dry rapidly. The x-chamber geometry is therefore not useful except in specialized situations. A slightly more helpful version is the counter-propagating flow chamber shown in Fig. 3.5 (G). In this version, the hydrogel bar is as long as possible, creating a "hydrogel window" that separates the two arms of the chamber. While this setup was never used to test protein selectivity, in principle a counter-propagating flow can be established using syringe pumps in order to simulate constant concentration in infinite inlet and outlet reservoirs while using a limited amount of material. A similar setup is demonstrated

in [127].

The no-outlet hydrogel geometries shown in Fig 3.5 (C) and (E) are much simpler to make but do not allow for measurement of protein selectivity. Panel (E) shows a variation on the small-outlet chamber in which the outlet is filled with hydrogel and crosslinked using a photomask. Finally, the droplet gels in panel (C) were added to the chamber before assembly and crosslinked without a mask (Fig. 3.4 (B)). These are the only hydrogels which were made without a mask, which greatly reduced the irreproducible edge effects (also seen in Sec. 3.8). Droplet gels have volumes of 0.5-2 μL and equilibrate 30-kDa proteins in 24-48 hours. While these gels cannot be used to monitor selective transport through and exit from the gel, we can use them to measure the diffusion constants of proteins within the gel and the selective influx of transport factors. Chapter 4 focuses entirely on droplet hydrogels made in 400- μm -thick PDMS gasket chambers with two PEEK-less ports.

3.4 FG Nup peptides

The remaining components of the nuclear pore mimics are the FG Nup fragments which are tethered to the hydrogel scaffold. There are a wide range of FG Nups, many of which can be deleted without apparently impacting nuclear transport [19,20]. We chose to use Nsp1, an essential FG Nup for selective transport, as the basis for our Nup peptides. Like all FG Nups, Nsp1 has an ordered domain which anchors it to the channel wall, and a disordered region containing many FG motifs. As a whole, the disordered region aggregates when isolated in buffer [48,49].

As shown in Fig. 3.7, we make use of two distinct fragments of Nsp1, denoted FSFG and FG124 [11]. Each are entirely disordered, are approximately 120 amino acids (14 kDa) in length, and contain multiple FG motifs. FSFG is so called because it possesses six FSFG repeats. It is extremely stable and unlikely to aggregate, remaining unaggregated throughout a wide range of buffers, pH values, concentrations, and crowding conditions. As an additional advantage, FSFG can easily be expressed and purified. The other Nup fragment, FG124, contains 8 FG motifs. If not kept in 7M guanidine hydrochloride, FG124 will aggregate over the course of several hours. However, FG124 does not aggregate in the cellular environment, suggesting that Nsp1 itself may

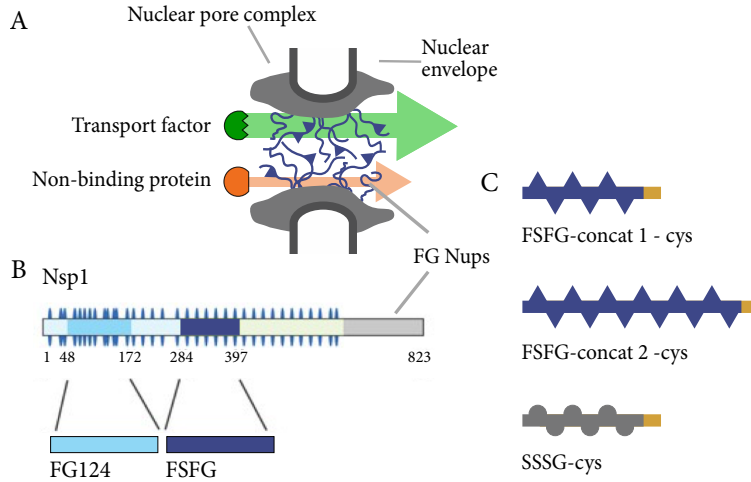


Figure 3.7: Nup fragments used in nuclear pore mimic experiments. (A) The nuclear pore with FG Nups filling the central channel. (B) The essential FG Nup Nsp1 shown as a schematic sequence, with FG124 and FSFG fragments noted. (C) Variants of FSFG: FSFG concat 1-cys with 6 FSFG motifs and a C-terminal cysteine; FSFG concat 2-cys, as above but twice as long; SSSG-cys, like FSFG concat 1-cys with the F's mutated to nonbinding S's.

not be aggregated in the nuclear pore [11].

Both FSFG and FG124 are expressed in Bl21 DE3 Gold cells in the pRSF plasmid, which is Kan resistant. Each has a C-terminus 6xhis tag and are purified using a metal affinity column as described in Appendix B. They are unharmed by lyophilization and resuspension.

We have access to a wide library of FSFG and FG124 variants, few of which I helped to create. Many originate in the Rout lab at Rockefeller University, and others were created by Andrea Egan, Nick Bax, Eric Verbeke, and myself. Appendix F provides the sequence of the most commonly-used Nup variants.

In order to test the effect of Nup length and number of FG motifs, FSFG also exists in concatenated versions: FSFG concat-2 (twice as long as FSFG) and FSFG concat-3 (three times as long). Although both have been expressed and purified, I was only able to express FSFG concat-2. All of these FSFG variants, as well as FG124 and the nonbinding negative control SSSG (Sec. 3.4.1), exist with one or both terminal cysteines as well. The C-terminal cysteine version is the most commonly used, as a cysteine is necessary to tether the Nup fragment to a hydrogel (Sec. 3.1 and Appendix D). It should be noted that ybbR FSFG cys is most commonly used in the nuclear pore mimics. The ybbR tag is intended for site-specific labeling with a fluorophore or other tag but almost always goes unused in the context of FSFG hydrogels [128].

The cysteines in all of the above Nup variants form disulfide bonds very rapidly (within

minutes) after being removed from reducing agents. In addition, the Bradford assay is unreliable for these Nup variants due to the relative lack of aromatic residues. A BCA assay should be used instead to quantify protein concentration.

In addition to the commonly-used Nup variants in Table F.1, we have access to several other Nup fragments and mutants. These include shortened versions of FSFG with two or four FSFG motifs, FSFG variants with most but not all binding motifs removed (FSFG mutated to FSYG), the full FG domain of Nsp1, and full-length Nsp1.

3.4.1 SSSG negative control

The obvious negative control for a Nup-filled hydrogel is a hydrogel containing no Nups. However, it is possible that the presence of FSFG in the precursor solution changes the final gel properties such as pore size, or that non-specific interactions between the Nup peptide and test proteins alter the behavior of the test proteins. To account for these possibilities, we designed a negative control peptide which is identical to FSFG except that the phenylalanine residues have been mutated to serine (i.e. FSFG goes to SSSG). This mutant does not bind NTF2, as demonstrated by the lack of NTF2 accumulation in hydrogels containing tethered SSSG. Figure 3.8 compares the intensity profile of a 10 wt% PEG hydrogel containing a nominal 10 mg/mL SSSG to that of a hydrogel with no nups. There is no dramatic difference between the two profiles, suggesting that the presence of peptide in the hydrogel does not itself alter the diffusion of NTF2 and mCherry. Following the initial tests, SSSG gels were used periodically to confirm that no-Nup gels served well as negative controls, but they were not used regularly as controls.

The SSSG peptide was prepared in an identical manner to FSFG: SSSG-cys was his-tagged, inserted into pRSF, and expressed in BL21-DE3 Gold cells. It was purified using a metal affinity column using the same procedure as FSFG variants and had a high yield. As with FSFG, SSSG is stable and non-aggregating over a wide range of conditions.

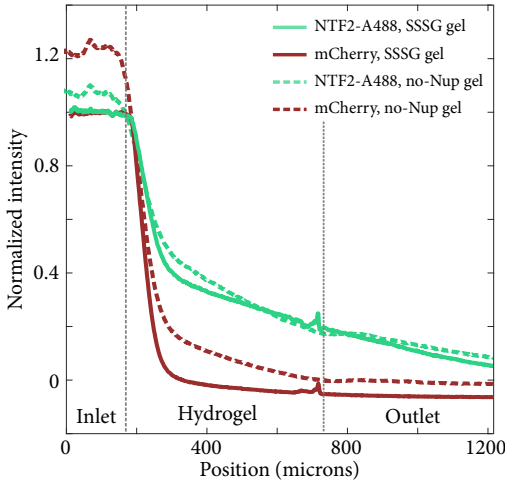


Figure 3.8: Comparison of intensity profiles for SSSG and no-nup (control) gels. Both hydrogels were 10% wt PEG with a 1-kDa PEG dithiol linker. The SSSG gel nominally contained 10 mg/mL SSSG. Inlet reservoir contained 20 μ M NTF2-A488 and mCherry in PTB. As expected, no binding is seen in either gel.

3.5 Transport factor constructs

A wide variety of transport factors exist, specialized for the import and export of particular cargo. Almost all protein separation experiments we performed made use of Nuclear Transport Factor 2 (NTF2). This transport factor is relatively small (28 kDa dimer) and, unlike most other transport factors, does not require active release of cargo after transport. NTF2 transports RanGDP as part of a mechanism which maintains a high RanGTP concentration in the nucleus, necessary for the active release of other protein cargos [37]. The choice to focus on NTF2 was made for a number of reasons: the lack of facilitated release makes it a simple first choice to study, it is small enough to move reasonably quickly through hydrogels, and it is readily expressed in bacteria and purified.

His-tagged yeast NTF2 in the Kan-resistant plasmid pRSF was expressed in BL21 DE3 Gold cells and purified using the procedure described in Appendix B. When necessary, NTF2 was covalently labeled with fluorescent dyes as described in Appendix G. In addition to wild-type yeast NTF2, several variants were created in order to address shortcomings of NTF2 in the experimental setup. In particular, efforts were made to prevent the presence of any NTF2 monomers and to eliminate the need for dye labeling. Finally, a point mutant of NTF2 was created with the intent of disrupting the binding pocket and providing another non-binding negative control protein to complement mCherry.

Beyond NTF2, we briefly tested the influx of Kap121, a member of the well-studied karyopherin family of transport factors, into hydrogels. Although the Kap121 and its fluorescent cargo protein clearly bound to the FSFG in the hydrogel, the pore size remained too small for significant import into the gel.

The remainder of this section provides an overview of the transport factor constructs we created. Much of the cloning work was done by Eric Verbeke and Scott Tilden.

3.5.1 Covalently-tethered NTF2 dimer

Despite the work done to increase the hydrogel's average pore size, we often observed that NTF2 and mCherry equilibrate to different extents and on different timescales even in hydrogels containing no Nups or nonbinding Nups. As these proteins are nominally the same size, this implies that they may be interacting differently with the hydrogel substrate, or that they may not be the same size after all. NTF2 is a 28 kDa homodimer whose monomers are 14 kDa. If there exists an appreciable population of NTF2 monomers within the hydrogel, these will equilibrate more rapidly and to a higher concentration than the larger mCherry. The dissociation constant K_D of mammalian NTF2 is about 1 μM [129]. Assuming this is approximately true for yeast NTF2 as well, there should be very little monomeric NTF2 present at our typical reservoir concentration of 20 μM .

However, we designed a covalently-tethered version of NTF2 to eliminate the possibility of monomerization. This consisted of two NTF2 monomers connected by a flexible amino-acid tether (Fig. 3.9 (A)). Several trial tethers with their length and composition are shown below:

10aa – linker :	TSGSGSGSPG
15aa – linker :	TSGSPRGSSGSGSPG
18aa – linker :	TSPGLVSRGSGSGSGSPG

Eric Verbeke and Scott Tilden successfully cloned covalently-tethered NTF2 with all three

tethers. Unfortunately, no binding was seen when the NTF2 was introduced to an FSFG hydrogel. It is likely that the tether interferes with the binding pockets or dimerization interface.

3.5.2 NTF2-GFP

In addition to the potential problem of NTF2 monomerization, the fluorophores that labeled NTF2 were prone to hydrolysis, leaving an unknown amount of free dye in the reservoir mixture. Free dye is indistinguishable from labeled NTF2 in the influx and selectivity experiments, and it is important that not be present in appreciable amounts. This problem is addressed through data processing in Sec. 3.9, but we also approached it by engineering a GFP-NTF2 fusion protein. Such a protein would eliminate the need for dye-labeling the NTF2 and therefore eliminate free dye in the chamber entirely.

However, as GFP is also approximately 30 kDa, the fusion protein is much larger than NTF2 alone. To mitigate this problem, a GFP-NTF2-NTF2 version was also created (Fig. 3.9 (A)). While this is still larger than an NTF2 dimer, it contains only one copy of GFP. Both constructs are in the pET21 plasmid, his-tagged, and expressed in BL21-DE3 Gold cells. They were purified using a cobalt affinity column in PTB and 1:1000 PIC and eluted with 250 mM imidazole, yielding ample protein with moderate degradation products.

Figure 3.9 (B) and (C) show that neither construct is able to bind to FSFG PEG hydrogels. Again, the binding pockets or dimerization interface may be disrupted by the tethers, or the fusion protein may simply be too large.

3.5.3 Non-binding NTF2 F5R

Although mCherry is a similar size as the NTF2 dimer and makes an acceptable negative-control inert protein, it may well interact differently with the hydrogel scaffold than NTF2 does. A better control would be a non-binding mutant form of NTF2. A W7A point mutant in mammalian NTF2 reduced its affinity for FG Nups [38, 56]. A corresponding mutant in yeast NTF2 is F5R. This mutant was cloned by myself and Scott Tilden, expressed, and purified. Further tests, such

Figure 3.9: Attempts to create functional NTF2 fusion proteins. (A) Cartoon of various NTF2 constructs: wild-type NTF2 dimer, covalently-tethered NTF2-NTF2, GFP-NTF2, GFP-NTF2-NTF2 (B) Intensity profile for GFP-NTF2 dimer showing no binding to FSFG hydrogel. Hydrogel contained a nominal 10 mg/mL FSFG; reservoir solution contained 20 μ M GFP-NTF2 and mCherry in PTB. (C) Similar experiment as (B) for GFP-NTF2-NTF2.

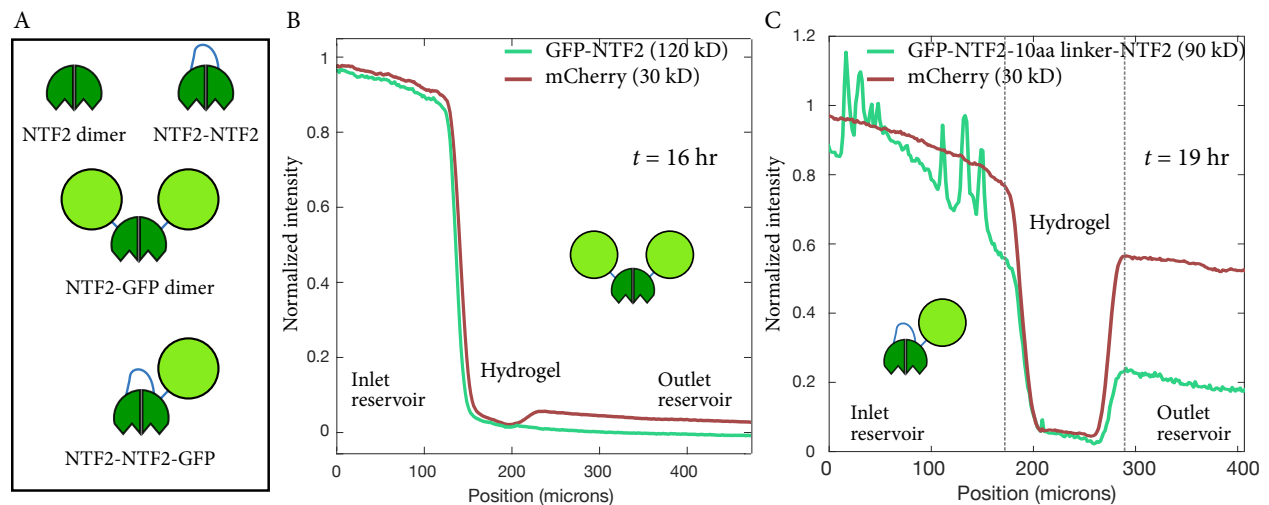
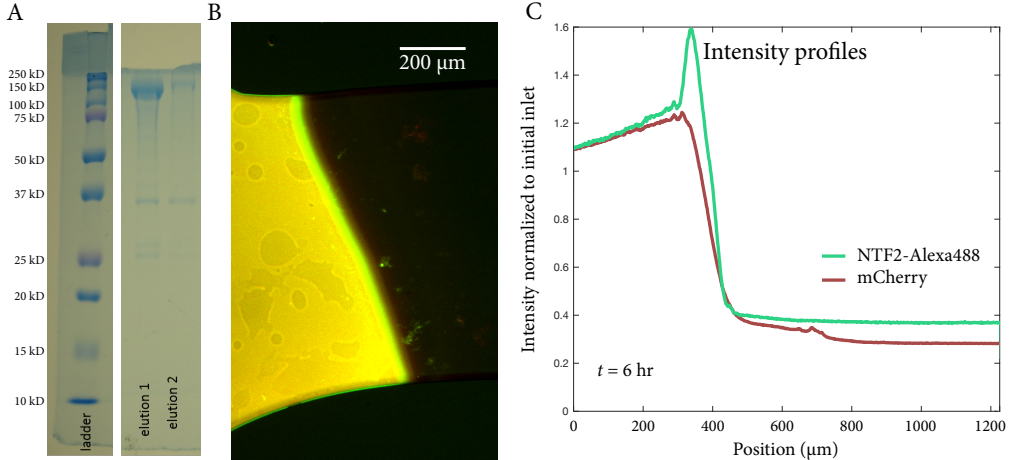


Figure 3.10: SDS-PAGE showing Kap121 purification (purified by Chris Lawton), picture of influx, intensity profiles



as NMR, are needed to verify its binding affinity for FSFG.

3.5.4 Kap121 and NLS-GFP

The karyopherins (Kaps) are a canonical class of transport factors. They transport proteins tagged with nuclear localization signals (NLS) through the nuclear pore. We were interested in testing Kaps because they are widely studied and much larger than NTF2, so selective transport would be more apparent. Eric Verbeke engineered two GFP-NLS constructs: GFP-Spo12 and GFP-Pho4 (Appendix F). These constructs were his-tagged, inserted into pET21b, expressed in BL21-DE3 Gold cells, and purified using a cobalt affinity column. Kap121-GST was expressed and purified following [63] and the GST subsequently cleaved with thrombin resin (Fig. 3.10 a).

Kap121 binding and influx was tested using a hydrogel made from precursor solution containing 0.05 wt% Irgacure2959, 110 mg/mL 20kD 8-armed PEG-norbornene, 11 mg/mL 1kD PEG-dithiol, and 1 mM TCEP in PTB, crosslinked for 2 minutes under the UV LED. After soaking in PTB overnight, 5 μM Kap121, 10 μM GFP-Pho4, and 100 μM mCherry in PTB were added to the inlet reservoir. Selective influx of the Kap121/GFP-Pho4 complex was evident, since the complex accumulated at the edge of the hydrogel (Fig. 3.10 b and c). The bright band demonstrates binding of FSFG to Kap121 as well as of Kap121 to GFP-Pho4. Over the course of several hours, the GFP

front remained localized at the edge of the gel, likely indicating that the pore size of the hydrogel was too small to accomodate the Kap121/GFP-Pho4 complex. Given the large size of this complex, the pore size was never increased sufficiently for influx into the hydrogels.

3.6 Pore size

The perennial difficulty with our hydrogel nuclear pore mimics has been the pore size of the hydrogels. While hydrogels with an average pore size between 10 and 100 μm are well-studied [130], as well as hydrogels with pores under 5 nm, the intermediate-porosity regime which would allow for separation of proteins in the size range 30-150 kDa (typically 5-10 nm) is difficult to reach. We wanted to be confident that any differences in the behavior of transport factor and inert protein were due to their interactions with the Nups, not slight differences in size or interactions with the hydrogel. At the same time, we wanted the anchored Nups to fill a significant portion of the pore. Much of our work on hydrogel design was with the aim of achieving a suitable pore size.

Hydrogel swelling in particular has been an obstacle in our search for protein-separating hydrogels. When polymerized from a precursor solution, hydrogels are almost never in mechanical equilibrium. They must be soaked in an aqueous solution until they have swelled and taken up enough water to reach equilibrium. Common methods of estimating pore size rely on the swelling ratio of the gel, i.e. the ratio of the wet to dry gel weight. However, our gels are small enough to make that method impractical, and it is unclear whether a Nup-filled hydrogel that is allowed to swell to equilibrium in buffer will have the same properties as one that is polymerized inside a confined flow chamber. In fact, repeated but unpredictable buckling and swelling of hydrogels within the flow chambers indicates that our hydrogels do not reach mechanical equilibrium. Despite efforts to improve the swelling ability of our hydrogels, the lack of equilibrium swelling likely contributes to the smaller-than-ideal pore size as well as inconsistency between replicate experiments.

Of the two hydrogel substrates tested, acrylamide gels appear to have a better pore size distribution than PEG gels. An order-of-magnitude calculation estimated 1 nm as the average mesh size of a 10 wt % PEG hydrogel, comparable to or smaller than the 5-nm size of NTF2

(Appendix C). We were not able to lower the weight percent of PEG and still achieve gelation. Overall, 6% w/v acrylamide gels are more mechanically stable and yield more reproducible results than 10% w/v PEG gels, the lowest stable percent weight PEG gel we were able to attain. Before settling on acrylamide hydrogels, we considered several alternative crosslinkers in hopes of creating more mechanically-stable PEG hydrogels that would support larger pores. Most notably, we moved from a 1-kDa PEG dithiol linker to an 8-kDa linker. This change did increase the pore size of the resulting PEG gel, but it was mechanically weak and required proportionately more swelling to reach equilibrium, an impossibility inside the flow chamber. DNA oligomers, coiled-coil rationally-designed proteins, and FSFG with both terminal cysteines were also considered as crosslinkers, but none were able to support gelation [131, 132]. Therefore, we turned our attention to acrylamide hydrogels.

Figure 3.11 shows the partition coefficient of equilibrated fluorescent macromolecules as a function of molecular weight for 6% acrylamide gels containing no Nups. The partition coefficient is the ratio of equilibrium concentration within the hydrogel to that in the reservoir outside; a partition coefficient of 1 indicates that the macromolecule's diffusion and equilibration is not impeded at all by the presence of the gel. Although 250 kDa dextran has a low partition coefficient, 30 kDa transport factors and fluorescent proteins have similar partition coefficients around $\gamma = 0.7$. The partition coefficient of inert proteins decreases when Nups are tethered to the hydrogel, as they further impede diffusion and equilibration.

The no-Nup hydrogel dataset used in Chapter 4, containing 17 experiments in total, provides another measurement of partition coefficient and diffusion. In this later dataset, both the NTF2 and mCherry partition coefficients are equal to 0.48 ± 0.03 , statistically indistinguishable. It is unclear why this value is lower than that measured in Fig. 3.11. On the other hand, the mean diffusion constant of NTF2 was $59 \pm 5 \mu\text{m}^2/\text{s}$, as opposed to $44 \pm 4 \mu\text{m}^2/\text{s}$ for mCherry. The two values are different with a p-value of $p = 0.02$ using a two-tailed t-test. These results indicate that NTF2 and mCherry do not behave identically within the hydrogel, but that they equilibrate to similar values, suggesting overall a small interaction with the hydrogel scaffold. We deemed this

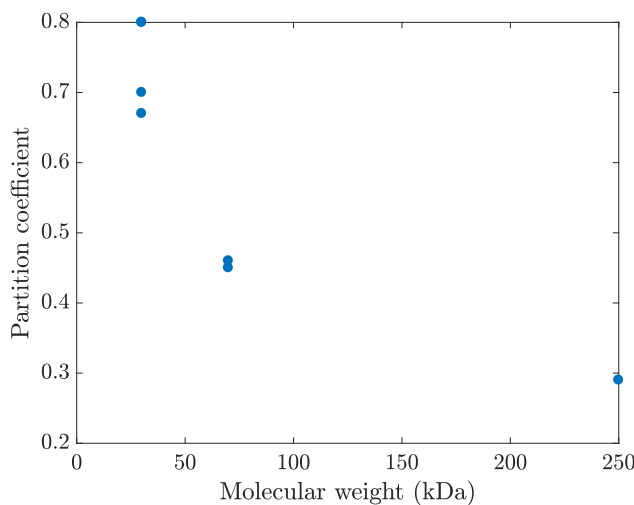


Figure 3.11: Equilibrium partition coefficient as a function of macromolecule molecular weight for 6% acrylamide no-Nup hydrogels. NTF2, mCherry and GFP were used as 30-kDa test proteins along with 70-kDa dextran-rhodamine and 250-kDa dextran-fluorescein.

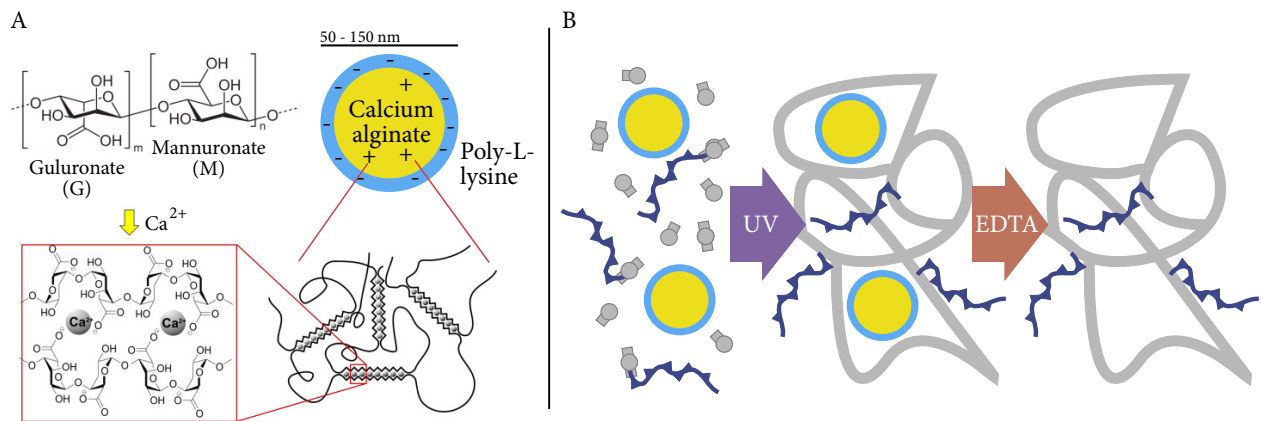
to be acceptable for the NTF2-mCherry pair but were not comfortable comparing the diffusion of larger proteins using acrylamide gels.

3.7 Porogens

Given the difficulties of increasing the average pore size by changing the hydrogel composition, we investigated the possibility of introducing a porogen into the precursor solution. To be useful, the porogen would need to be a macromolecule or particle 10-100 nm in diameter that could be evenly distributed throughout the precursor solution and then hydrogel without disrupting polymerization. The porogen would then be digested, dissolved, or otherwise removed from the hydrogel, as it would be too large to passively diffuse from the gel on a reasonable timescale. The pores left behind would then increase the overall pore size of the gel as well as potentially allowing the hydrogel network to swell to equilibrium even while confined in a chamber.

Two possible porogens were tried: Alginate nanospheres and high-molecular-weight dextran. Alginate can be polymerized and depolymerized through the addition or removal of calcium ions, and dextran can be digested by dextranase. Although both showed promise, neither was ultimately well-suited to increasing a hydrogel's pore size.

Figure 3.12: Alginate crosslinking from [133]. (A) Alginate is composed of alternating guluronate (G) and mannuronate (M) blocks. Addition of calcium ions leads to an “egg-box” crosslinked structure. Calcium alginate nanospheres are coated with poly-L-lysine [134]. (B) Alginate nanospheres should act as a porogen when added to a hydrogel precursor solution. Removal of the spheres with EDTA should leave larger pores in the crosslinked hydrogel.



3.7.1 Alginate nanospheres

Alginate is a polysaccharide derived from algae which polymerizes upon addition of calcium ions (Fig. 3.12 (A)). It can be depolymerized by adding EDTA or another chelator to remove the calcium. Alginate salts are available in a number of molecular weights and viscosities, making it a promising candidate for a porogen. If alginate nanospheres could be polymerized and added to the hydrogel precursor solution, they could later be removed with EDTA, leaving larger pores than would otherwise be present (Fig. 3.12 (B)).

A number of protocols exist for creating alginate microspheres, but fewer are appropriate for nanospheres, which is the scale that we would need in order to use them as a porogen. I made nanospheres following the method described in [134].

I prepared 10 mL of 0.6 mg/mL alginic acid sodium salt (Sigma, low-viscosity, product number A0628) in water. Even a small amount of sodium alginate added to water creates a viscous solution that takes a lot of time and stirring to dissolve. I used a sonicator with microtip to sonicate the sodium alginate solution while adding 2 mL of 0.67 mg/mL calcium chloride in water drop-by-drop. I then stirred the solution on a magnetic stir plate for 30 minutes before adding 2 mL of 0.3 mg/mL poly-L-lysine in water. The solution was then stirred 30 more minutes.

I tested several methods of preparing the nanospheres for addition to the hydrogel precursor solution. First, the nanospheres were left in the solution in which they were made. Second, the nanospheres were spun down out of that solution at 14400g for 10 minutes and immediately resuspended in deionized water. (The pellet becomes more difficult to resuspend if it is not immediately resuspended.) Finally, the nanospheres were lyophilized and resuspended in water. The resuspended solution remained cloudy even after several days, and so I didn't pursue lyophilizing the nanospheres.

The radius and diffusion coefficients of the both the non-spun and spun nanospheres were determined using a Titan DynaPro dynamic light scattering (DLS) system. The non-spun nanospheres had an average radius of 170 ± 10 nm, with an estimated diffusion constant of $1.1 \pm 0.1 \mu\text{m}^2/\text{s}$. The

nanospheres that had been spun and resuspended had two populations: almost entirely particles of radius 210 ± 10 nm and diffusion constant $1.05 \pm 0.06 \mu\text{m}^2/\text{s}$, and a small number of very large particles. The large particles are probably aggregates from centrifugation.

After measuring the size distribution of the two samples, I added EDTA in an effort to depolymerize the nanospheres. The maximum final EDTA concentration was 25 mM, and the samples were left to sit up to 30 minutes. Re-running the DLS data gave inconclusive results as to the presence or size of remaining particles. The fits did not change much, although the large aggregates appeared to have vanished from the spun sample. It appeared that at least some nanospheres remained.

Next, the nanospheres were added to hydrogel precursor solution, which was then crosslinked. Several nanosphere concentrations were tested before a condition was found in which the nanospheres appeared by eye to resuspend. An approximately 2 μL nanosphere pellet (spun down from 10 mL of solution) was resuspended in a final concentration of 0.11 mg/mL PEG-ene, 0.09 mg/mL 8K PEG dithiol linker, and 5 mM LAP, all in 50 mM MOPS buffer pH 7.4. The MOPS buffer was chosen because it has no divalent cations (and thus will not interfere with the alginate nanospheres). The isoelectric point of poly-L-lysine is at about pH 5, and the nanospheres should be kept above that pH so their coating remains intact.

However, even these gels were clearly inhomogeneous under 4x magnification. In an attempt to depolymerize the nanospheres, the resulting hydrogels were rinsed with PTB pH 5 (to remove any possible poly-L-lysine coating) and then soaked in 100 mM EDTA for two days. No change was observed under 4x magnification. For comparison, a macroscopic alginate droplet dissolved after 20 minutes in 100 mM EDTA and vortexing. New gels were made and soaked in a pH 5 buffer (to remove any poly-L-lysine coating) and then in a solution containing 100 mM EDTA and 200 mM sodium citrate. Gels remained cloudy and no change was observed.

Given the difficulty in resuspending and depolymerizing the alginate nanospheres, our focus shifted to developing a dextran/dextranase porogen system.

3.7.2 Dextran/dextranase porogen system

Following the alginate nanospheres attempt, we tried creating nanopores using high-molecular-weight (high-MW) dextran. Dextran is a branched, inert polymer that is commercially available at molecular weights up to 250 kD. We used two sizes as porogens, 70 kD ($R_H \approx 10$ nm) and 250 kD ($R_H \approx 15$ nm) [135].

As a proof of concept, I made and crosslinked precursor solutions containing 100 μ M 70 kD dextran-rhodamine or 250 kD dextran-fluorescein. The precursor contained 12% acrylamide and 3.3% bisacrylamide in 50 mM sodium acetate (NaOAc) buffer pH 5 as well as 2 mM LAP. The precursor solution was crosslinked as 1- μ L hydrogels in a 400- μ m tall PDMS gasket chamber for 20 s using the UV LED. After rinsing with NaOAc buffer, the chamber was filled with a freshly-made solution of 20 mg/mL dextranase (Sigma, D5884, dextranase from *Penicillium sp.*) in NaOAc buffer. Chamber was immediately placed in the Olympus widefield's environmental chamber, held at 37°C, and imaged overnight. The fluorescence intensity in the dextranase-treated gels decreased significantly more rapidly than that of gels which contained dextran but were not treated with dextranase (Fig. 3.13). In the case of 70 kD dextran, the fluorescence reached a steady value (equilibrated, same as that in the reservoir) in approximately 100 minutes, while the non-treated case wasn't equilibrated after an overnight incubation. For the 250 kD dextran, both the treated and non-treated gels reached an equilibrium in approximately the same amount of time, but the treated gel equilibrated much closer to the reservoir level than the non-treated gel. Both sets of gels indicate that dextranase is able to digest the dextran within the hydrogels, allowing a significant amount of dextran and digest products to leave the gel, as expected.

The next step in attempting this porogen system was recreating the effect in FSFG gels. Unfortunately, it became clear that the dextranase was digesting the FSFG as well as the dextran (Fig. 3.14). At this point, we stopped trying to use the dextran-dextranase porogen system for FSFG gels. However, we did investigate the effect of dextran-dextranase treatment on the pore size in acrylamide hydrogels without anchored proteins. Contrary to expectations, dextran-dextranase

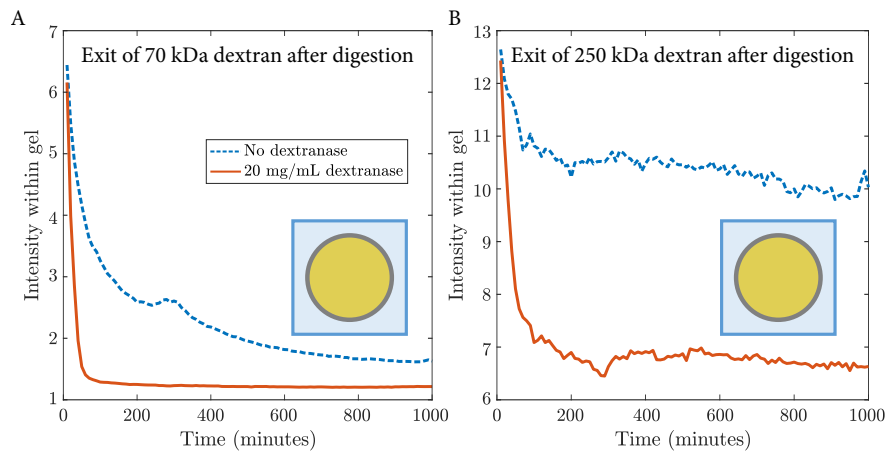


Figure 3.13: Exit of fluorescent dextran from hydrogels after digestion with dextranase. Each hydrogel originally contained 100 μM dextran and was treated with 20 mg/mL dextranase as described in the text. The total fluorescence intensity within the gel was monitored as a function of time as it approached equilibrium with the buffer in the reservoir. Intensity was normalized to initial gel fluorescence.

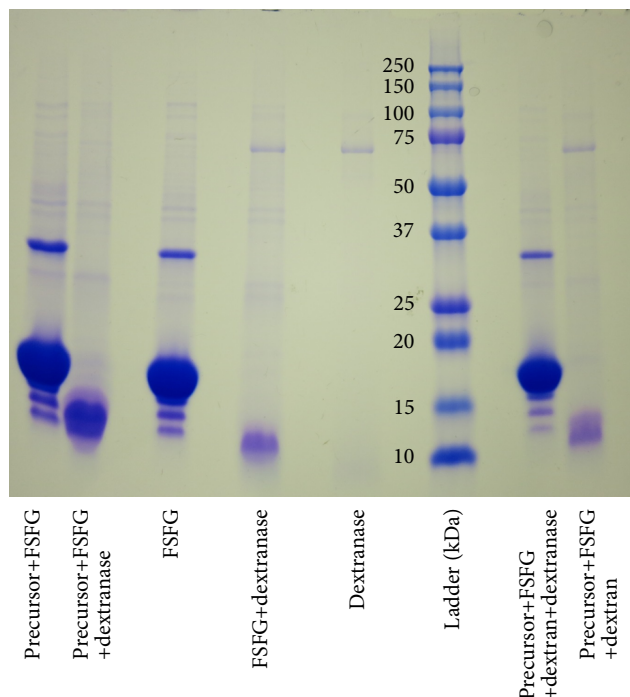


Figure 3.14: SDS-PAGE gel demonstrating dextranase digestion of FSFG. Three conditions are shown, with and without dextranase: precursor solution with FSFG, FSFG only, and precursor with FSFG and dextran. In each case, addition of dextranase destroys the FSFG band at 15 kDa and produces bands of smaller degradation products. Dextranase alone is shown for reference. AnyKd PAGE gel (BioRad), 100 V, 80 minutes.

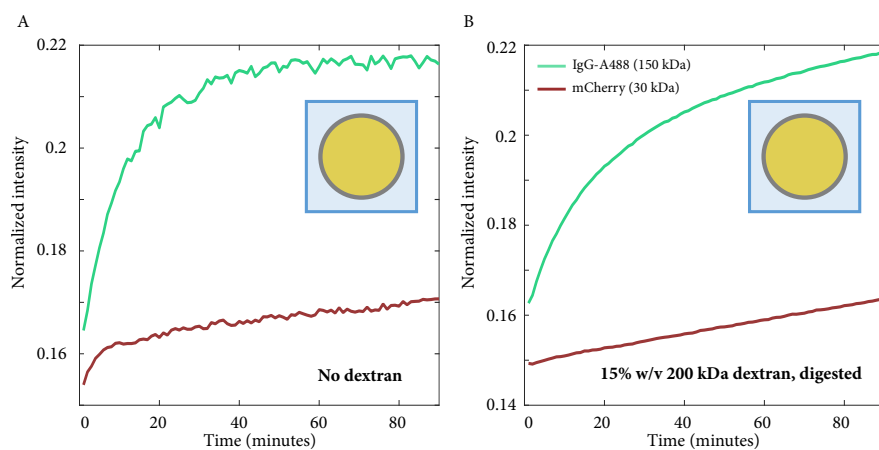


Figure 3.15: Comparison of protein accumulation within hydrogels made with or without dextran. Reservoirs contained 10 μM IgG-A488 and mCherry. (A) Accumulation in a 12% acrylamide hydrogel containing no Nups or dextran. (B) Accumulation in a 12% acrylamide hydrogel containing no Nups but made with 15% w/v 200 kDa dextran and digested for 2 hours at 37°C with 20 mg/mL dextranase.

treatment did not increase subsequent diffusion of fluorescent proteins into the treated hydrogels. For these experiments, I used 200 kD non-fluorescent dextran in the acrylamide precursor solution. After the gels (either 12% or 6% final acrylamide concentration) were crosslinked, I treated them with 20 mg/mL dextranase solution in sodium acetate buffer (freshly made solution) for 2 hours at 37°C in an incubator. Then I rinsed the gels with buffer and used a syringe pump to flow 10 mL of PTB through the chamber over the course of 10 hours. The next day, I challenged the gels with a solution containing 10 μM each immunoglobulinG tagged with Alexa Fluor 488 (IgG-Alexa488, 150 kD) and mCherry (28 kD). I monitored the accumulation of each protein in the gel over time (Fig. 3.15). In both the 12% and 6% acrylamide gels, dextran-dextranase treatment did not improve influx of IgG-Alexa488 over corresponding non-treated gels. In 6% acrylamide gels, the influx of mCherry also remained approximately the same for treated and non-treated gels. This indicates that dextran-dextranase treatment does not significantly increase the pore size in acrylamide hydrogels. This is probably because significant dextran remains in the gel even after dextranase treatment, as suggested by Fig. 3.13.

In conclusion, dextranase is capable of digesting a significant fraction of high-MW dextran within an acrylamide hydrogel. However, a significant amount of the dextran still remains in the gel even after an overnight rinse, meaning that dextran-dextranase treatment does not result in noticeably larger pores overall. In addition, the dextranase we used digested the FSFG peptide

as well as dextran. Dextran-dextranase treatment is not suitable as a porogen system for our hydrogels.

3.8 Polymerization using confocal microscope

Although photomasks are simple to use, they have several drawbacks. As shown in Fig. 3.4, the flow chamber is filled with precursor solution and only a portion is exposed to UV light. The edges of the exposed region tend to behave differently depending on whether they are bounded by air or precursor solution. When using a photomask, the edge of the resulting gel typically shows a dip in transport factor or inert protein concentration when equilibrated, similar to that seen in Fig. 3.19. This dip is undesirable, as it makes fitting to the concentration profiles more difficult and is irreproducible. Additionally, the smallest feature that can be created with a photomask is a bar around 150 μm in thickness with a variability of about 50 μm . Smaller features would permit more rapid outlet equilibration and use less material.

Given the problems that arose using photomasks and a UV LED to make hydrogels, we tested a crosslinking method using a 405 nm laser on the Nikon A1R spinning disc confocal microscope in the JSCBB microscopy facility. Once a region of interest has been defined with the Nikon software, the photobleaching setting can be used to selectively expose regions of the field of view to UV light. The precursor solution therefore crosslinks in the region of interest only. This method is similar to that used in [127], but the masking is done using the A1R software instead of a physical mask in the back focal plane.

We were able to “draw” hydrogels of arbitrary shapes using the 10x objective on the confocal along with the 405 nm laser at 100% power. Figure 3.16 shows hollow rings with an outer diameter of about 600 μm and an inner diameter of 500 μm , as well as lines with a width of about 50 μm . In order to crosslink the precursor solution, two raster-scans of the laser across the region of interest were needed, with the longest-allowable dwell time per pixel. (In the microscope settings, the shortest dwell time is set as ‘1’ and the longest as ‘1/32’.) The precursor solution contained 0.5 mM LAP, 110 mg/mL 20kD 8-armed PEG-norbornene, 11 mg/mL 1kD PEG-dithiol, and 1 mM

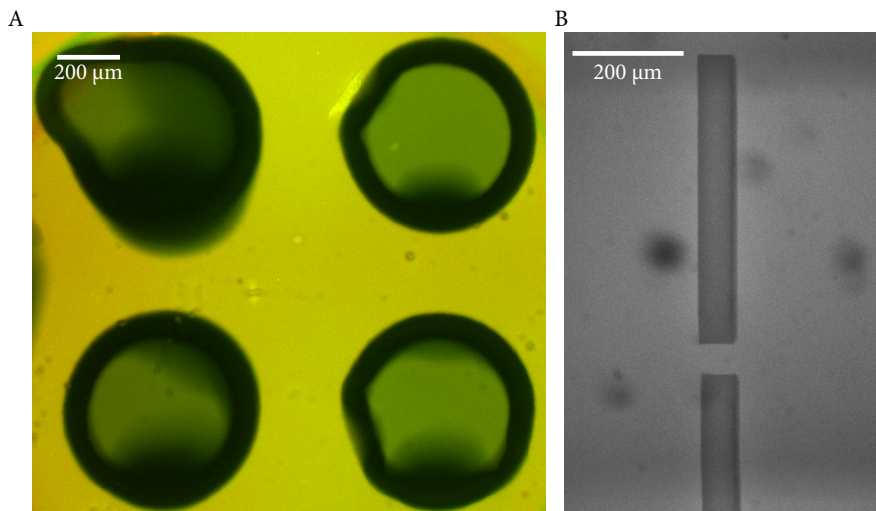


Figure 3.16: Image of laser-written hydrogels. (A) Ring hydrogels containing no Nups. Reservoir contains $20 \mu\text{M}$ NTF2-A488 and mCherry. (B) Line hydrogels containing FSFG-A647. Reservoir contains precursor solution with FSFG-A647. Photobleaching within gel by 405 nm laser is evident.

TCEP in PTB; it was used to fill 70- μm -thick sticky-tape or NOA flow chambers.

Crosslinking with the confocal has several advantages over LED crosslinking. Significantly smaller features are possible using the confocal. 50- μm features are consistent and reproducible, and features down to approximately 25 μm are possible, in contrast with the effective 100- μm lower limit using the LED and photomasks. Additionally, arbitrary shapes, including shapes with inner cavities, are possible using the confocal. Multiple small hydrogels can be created in the same chamber, including hydrogels of varying composition, created by removing the excess precursor solution and refilling the chamber with a different solution. Finally, the degree of crosslinking can potentially be varied by changing the photobleaching settings.

The most appealing geometry made possible with confocal crosslinking is the hydrogel ring, as shown in Figs. 3.16 and 3.18. Unlike all other hydrogel-chamber geometries, the inner reservoir is small enough to equilibrate in only a few hours (Fig. 3.17). Ideally, the hydrogel rings could have been used to test selective flux through the NPC mimics, a possibility not offered by other hydrogel-chamber geometries, which are optimized for testing influx into the hydrogels only. Long thin lines can also be written with the confocal by repeatedly moving the field of view and re-crosslinking, overlapping the new segment with the previous. This geometry could be useful in creating counter-propagating flow chambers with hydrogel windows.

Confocal crosslinking does not damage FSFG, as demonstrated in Fig. 3.18. Hydrogels were

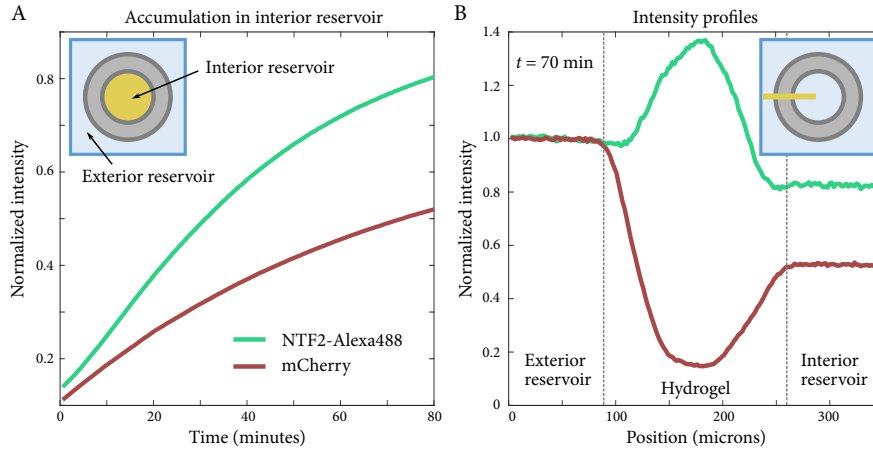


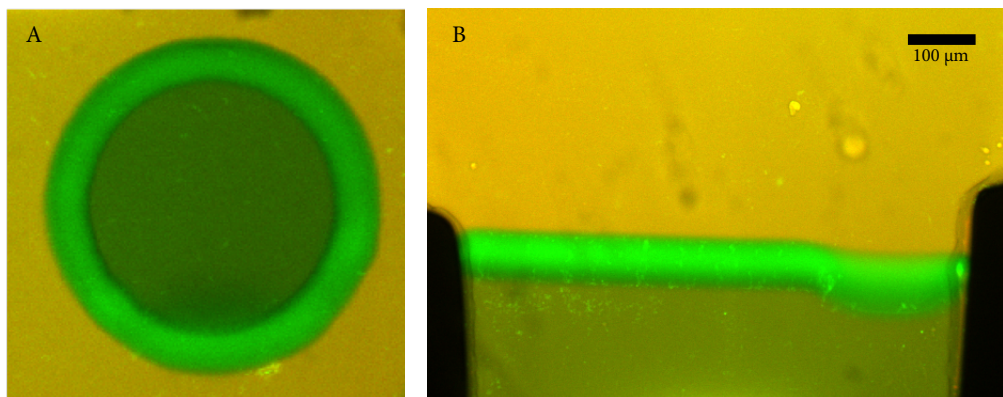
Figure 3.17: Sample (A) accumulation and (B) intensity profile plots for a 50 μm thick confocal-crosslinked ring nominally containing 10 mg/mL FSFG. Intensity normalized to inlet reservoir. Inlet contains 25 μM NTF2-Alexa488 and mCherry in PTB.

made using the precursor solution described above with the addition of 10 mg/mL FSFG-cys. After soaking in PTB buffer overnight, a mixture of 25 μM each NTF2-Alexa488 and mCherry was added to the outer reservoir. After two hours of equilibration, the FSFG hydrogels showed a partition coefficient greater than one for NTF2-Alexa488 but smaller than one for mCherry. This indicates that FSFG is anchored into the gel and that NTF2-A488 is able to bind it.

Finally, Norland Optical Adhesive (NOA) can also be crosslinked using this method. Complicated flow chambers can be created, although it is labor-intensive and difficult to remove all of the excess NOA afterwards.

Despite the advantages of confocal crosslinking, several obstacles combined to ultimately make this method unusable for our purposes. The most serious problem was that of stray crosslinking. Areas outside of the defined region of interest were often unpredictably crosslinked, as can be seen in Fig. 3.16. Stray crosslinking outside of the rings is limited by rinsing the gels within 5 minutes of crosslinking, removing any excess precursor solution [127]. However, rinsing the chamber does not remove precursor solution from the ring's inner reservoir. Stray crosslinking in this reservoir is often more difficult to detect and more damaging to the experimental results. Figure 3.18 illustrates the problem: the ring has been equilibrated with NTF2-A488, which has preferentially entered the inner reservoir over mCherry. The concentration of NTF2-A488 is, in fact, higher in the inner than the outer reservoir, indicating that there is some low concentration of FSFG available in the inner reservoir for binding to NTF2. As the hydrogel was soaked in buffer overnight after

Figure 3.18: Images of laser-written hydrogels nominally containing 10 mg/mL FSFG. Reservoirs contain 20 μ M NTF2-A488 and mCherry. (A) Hydrogel ring, likely with lightly-crosslinked inner reservoir. (B) Hydrogel bar separating large inlet and small outlet.



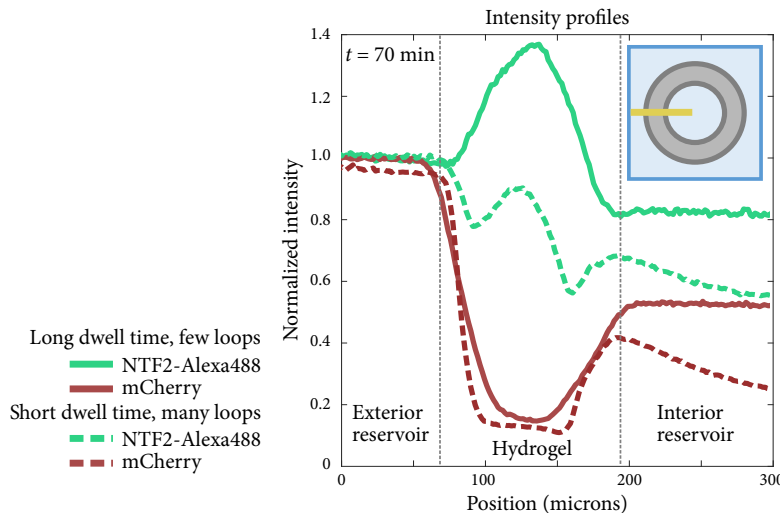


Figure 3.19: Effect of dwell time and loop number on edge-dip effect in equilibrated, confocal-crosslinked ring hydrogels. Nominal FSFG concentration is 10 mg/mL. Reservoirs contain 20 μM NTF2-A488 and mCherry in PTB. Intensity profiles are shown for a hydrogel polymerized with $t_{\text{dwell}} = 1/32$ and two loops (solid lines) and a hydrogel polymerized with $t_{\text{dwell}} = 1$ and 64 loops.

crosslinking, any mobile FSFG remaining from the precursor solution has been removed, meaning that the remaining FSFG is most likely anchored into a lightly-crosslinked hydrogel that fills the inner reservoir. The presence of this gel alters the results of an equilibration experiment by artificially increasing the final NTF2 concentration in the inner reservoir.

With help from Danielle Konetski and Christopher Bowman, we attempted to address the stray crosslinking by adding a photoinhibitor to the precursor solution. The radical inhibitor 2,2,6,6-tetramethylpiperidine 1-oxyl (TEMPO) can be used in aqueous solution to limit crosslinking [123]. We tested the effect of the photoinhibitor using a precursor solution as described above with the addition of 0.5 mM TEMPO. While the edges of the resulting hydrogels became marginally sharper, stray crosslinking was still evident, especially in the interior reservoir.

Another significant problem was swelling and buckling of the hydrogels. Despite the hope that thinner hydrogels would swell and equilibrate more easily, buckling of the rings and lines was pervasive and difficult to predict (Fig. 3.16). Ring hydrogels in particular often developed minor leaks due to buckling. Despite many attempts to improve the swelling problem, the rings ultimately could not be used for selective transport experiments.

One interesting feature of confocal crosslinking is the degree of control it affords over the illumination method. In the A1R's photobleaching mode, the 405 nm laser is raster-scanned over each pixel in the field of view. The shutter is toggled in order to illuminate only pixels within the

predefined region of interest. The controls permit the laser intensity, dwell time at each pixel, and number of raster scan loops to be varied. The laser intensity was always kept at 100%, but changing the dwell time and loop number had a dramatic effect on the final properties of the hydrogel.

Generally speaking, a longer dwell time at each pixel and a low number of loops gave the best results. Figure 3.19 shows post-equilibration profiles for two hydrogel rings made with different illumination settings. Each gel received the same total illumination time, but in one case the dwell time was reduced 32-fold and the loop number increased by the same factor. In both cases, the hydrogels were soaked in PTB buffer overnight and then challenged with 25 μM NTF2-Alexa488 and mCherry. After 70 minutes, sufficient NTF2 had accumulated in the gel to make the differences between gels obvious. The low-dwell-time hydrogel accumulated less NTF2 and displayed noticeable dips in NTF2 accumulation at both its inner and outer edges. The edge-dip is reminiscent of those noted in the gels crosslinked by photomasking and the UV LED. While the cause of the dip is unclear, it may be the result of diffusion of fresh precursor solution into the edge region over the course of the crosslinking process. The fresh precursor then crosslinks, leading to a dense hydrogel edge that excludes NTF2 and mCherry. This hypothesis is consistent with the observation that a longer dwell time and fewer raster loops largely eliminated the edge dip. With fewer raster loops, there is less opportunity for diffusion of uncrosslinked precursor solution into the gel edge. It should also be noted that the edge dip does not form when an entire droplet of precursor solution is crosslinked with the UV LED (i.e. no mask is used), further supporting the diffusion explanation. In any case, long dwell times and low loop numbers are clearly preferable with confocal crosslinking.

In conclusion, confocal crosslinking has a number of advantages over LED crosslinking, and a corresponding number of obstacles. Despite the attraction of testing selective transport using small hydrogel rings, we ultimately chose to use a much simpler hydrogel geometry and crosslinking method.

3.9 Dye-labeling and free dye

NTF2 must be labeled with a fluorescent dye before it can be used in diffusion experiments. Alexa Fluor 488 or fluorescein have both been used. When photobleaching is needed, as in the case of fluorescence recovery after photobleaching, fluorescein should be used, due to the extreme photostability of Alexa Fluor 488. There are several choices of labeling chemistry, including both NHS and SDP esters, which label the multiple exposed lysines of NTF2, and maleimide, which labels the cysteine of an engineered NTF2-cys. Both labeling chemistries result in bonds that eventually hydrolyze, cleaving the dye from the protein.

Free dye is a significant problem for diffusion experiments, since free dye (about 1kDa) diffuses much faster than dye bound to a protein and is experimentally identical. Non-negligible levels of free dye would give the impression that NTF2 is equilibrating significantly faster than it actually is. With help from Annette Erbse, Eric Verbeke and I tested several protocols to optimize the dye-labeling process and minimize the presence of free dye. We found that the maleimide-labeling chemistry is more stable, but in practice not as efficient as the ester-labeling protocol. Ultimately we chose to use esters for labeling. Detailed protocols are described in Appendix G. Extensive washing during the protein re-purification step is crucial, as is immediate aliquoting and freezing of the labeled protein. Labeled protein should be used within a few days of thawing.

As soon as possible after a reaction, a BCA is performed to quantify the protein concentration in the labeled sample. Within 24 hours, the labeled protein is aliquoted and frozen. A small sample is thawed and run on a native PAGE gel along with a sample of free dye. The gel is then imaged using a Typhoon fluorescence imager and stained with Coomassie. The intensity of each fluorescence band in the labeled protein sample is estimated with a line scan. Figure 3.20 shows a representative batch of labeled protein. Typically, the free dye band is 1-3% the amplitude of the labeled-protein band. Finally, I measure the absorbance of the labeled protein at 494 (check this wavelength) nm to calculate the concentration of Alexa488. I compare this measurement with the protein measurement from the BCA to calculate a labeling efficiency. Typical labeling efficiencies

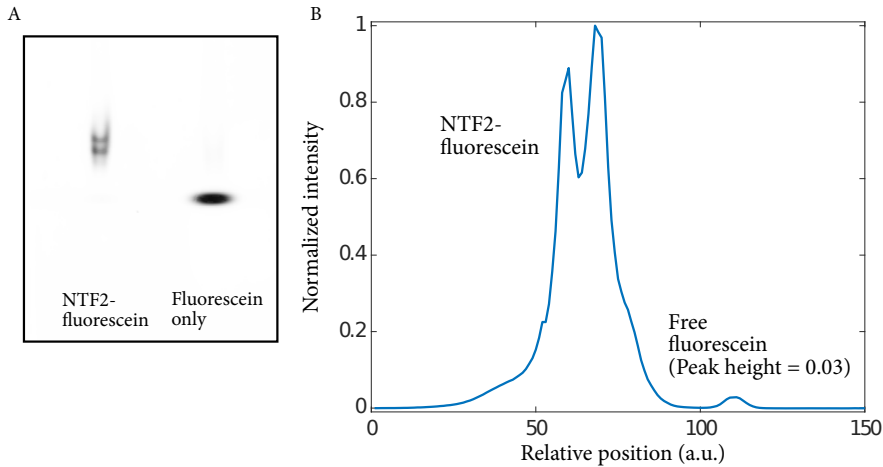


Figure 3.20: (A) Fluorescence Typhoon image native PAGE gel containing freshly-labeled NTF2-fluorescein sample and fluorescein sample. Free dye band is too dim to see. NTF2 shows monomer and dimer band. (B) Line scan of NTF2-fluorescein sample. The height of the free dye peak is 3% that of the labeled protein peak.

are 50-70%, lower than the reported values of 90% or more.

Mathematical analysis also suggests that free dye is minimal when the optimized protocol is used. A large dataset of accumulation curves was fit to either single or double exponentials and the resulting parameters and goodness of fit analyzed. While the accumulation curve should in fact be related to the error function (Sec. 4.4.1), exponentials were used to simplify the analysis.

If there is no free dye, as in the case of the mCherry accumulation, the accumulated intensity $I(t)$ can be approximated as

$$I(t) = A_1 \exp(-t/\tau_1) + C \quad (3.1)$$

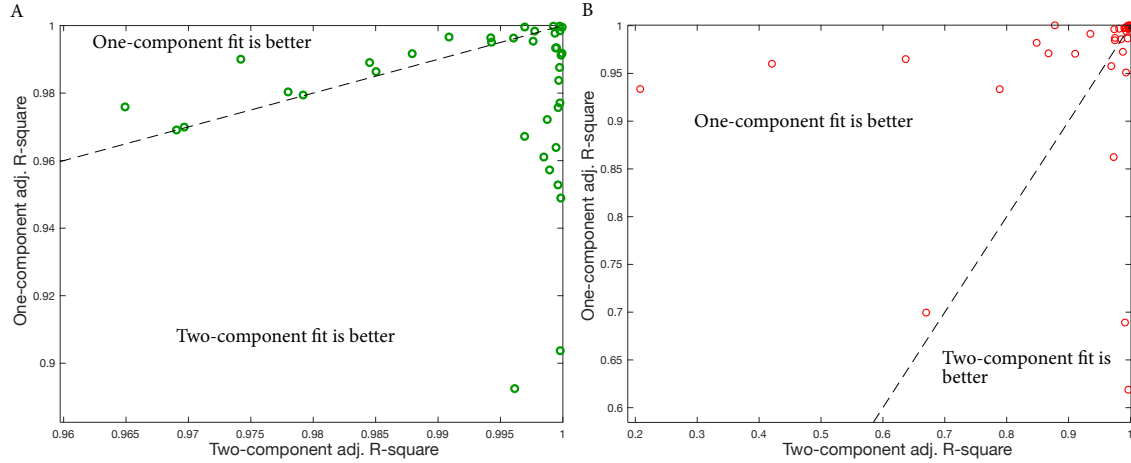
with some amplitude A_1 , equilibration lifetime τ_1 , and constant offset C . In this case, a non-zero value of C is likely due to background fluorescence. If, on the other hand, a sample contains a population of small, free dye molecules as well as large labeled protein, both populations will equilibrate at different rates, leading to an accumulated intensity of

$$I(t) = A_1 \exp(-t/\tau_1) + A_2 \exp(-t/\tau_2) + C \quad (3.2)$$

where each population has an equilibration lifetime as well as an amplitude related to its abundance in the sample.

I fit a collection of 43 accumulation experiments to both Eqns. 3.1 and 3.2. I compared the resulting parameters as well as the adjusted R-square value of each fit. Adding more parameters to the fit will always improve the fit, but the adjusted R-square is intended to account for the effect

Figure 3.21: Comparison of adjusted R-square goodness-of-fit value for one- and two- component exponential fits for (A) NTF2 and (B) mCherry accumulation fits. Dotted line indicates no change between fits. Points in the upper left fit better to a single exponential while points in the lower right fit better to a double exponential.



of adding more parameters to a model. A higher adjusted R-square therefore means a better fit.

The adjusted R-square values did not significantly improve when the mCherry data was fitted to a double instead of a single exponential (Fig. 3.21B). The adjusted R-square values changed by an average of -0.04 ± 0.03 . In addition, the lifetimes and amplitudes of each component of the two-component fit were apparently uncorrelated. Both results support the fact that there is no free dye in the red channel, since the only fluorescence is coming from mCherry.

On the other hand, the NTF2 fits did result in a significantly higher (0.019 ± 0.006) adjusted R-square value on average with the double-exponential fit (Fig. 3.21A). Strikingly, the two components sorted themselves into two categories: a low-amplitude, short-lifetime component and a high-amplitude, long-lifetime one. The most straightforward interpretation is that the low-amplitude component is the free dye, which should be present in low amounts and equilibrate much more rapidly than labeled protein, thanks to its small size.

The median amplitude of the free-dye signal was 1.2% that of the labeled-protein signal, using a sample of 43 experiments, a result comparable to that seen in Fig. 3.20. The median free-dye equilibration lifetime was 50 minutes, as compared to approximately 2000 minutes for the labeled-protein lifetime. These results confirm that the new, more stringent dye-labeling protocol is

successful in removing almost all free dye from the labeled-protein sample, and that the hydrolysis of the dye is negligible on the time scale of the experiment and enforced shelf life of the labeled protein.

Chapter 4

Bound diffusion measurements

Bound-state mobility - the ability of a macromolecule to diffuse while binding to its environment - was the key parameter in our simplified model of selective transport in Chapter 2. After many false starts, we designed an experimental system to investigate bound diffusion in biomaterials. This hydrogel nuclear pore mimic, as described in Chapter 3, is inspired by the nuclear pore but does not attempt to exactly reproduce selective nuclear transport. Instead, it is designed to provide a method of measuring the effect of model parameters such as binding valency, tether length, and tether concentration on bound diffusion.

Diffusion of transport factors and inert proteins was measured within the Nup-filled hydrogels using two main methods: by quantifying the influx of these proteins into the hydrogels, and by measuring fluorescence recovery after photobleaching (FRAP) using hydrogels equilibrated with fluorescent proteins. FRAP relies on the gradual redistribution of fluorophores after patterned photobleaching. After a small portion of the hydrogel is bleached, the bleached spot gradually exchanges with the non-bleached fluorophores outside, and the average fluorescence intensity within the bleached spot recovers. The recovery lifetime can be used to determine the fluorophore's diffusion constant, and the final recovered intensity as compared to the intensity outside the bleach spot can be used to determine the mobile fraction of fluorophore. Many models of FRAP exist, including some that take binding into account [136–139]. We made use of several models of varying degrees of complexity.

We calculated bound diffusion constants for NTF2 in hydrogels containing FSFG concat-1

or FSFG concat-2 and found non-zero bound diffusion in both cases. Both tether lengths led to bound diffusion that was consistent with that predicted by our tethered-diffusion model.

4.1 Experimental parameters

Our reaction-diffusion model of selectivity is controlled by a relatively small number of parameters. Ideally, we would like to vary all of these experimentally in order to verify the model's predictions. In reality, most are highly difficult to alter in a well-controlled way. Of the model's parameters, the contour length L_C of the tethered Nups is the simplest to control. Varying this contour length will vary the bound diffusion coefficient D_B according to Eqn. 2.22. This section discusses L_C and the other experimental parameters used in our hydrogel nuclear pore mimics.

4.1.1 Nup contour length and valency

The most straightforward way to vary D_B is to change the contour length of the Nups that are anchored into the hydrogel. To that end, we compared hydrogels containing the constructs FSFG concat-1 and FSFG concat-2 (Sec. 3.4, Appendix F). These Nup fragments have $L_C = 50$ nm and 100 nm, respectively. Given the parameters described below, the bound diffusion constant should increase by roughly 40% from FSFG concat-1 to FSFG concat-2.

In addition to differing lengths, the FSFG concat-1 and concat-2 differ in their number of binding sites, with six and twelve respectively. In order to control for the change in binding valency, we tested FSFG concat-2 hydrogels with the same molar concentration of FG repeats as the FSFG concat-1 gels as well as testing gels with the same molar concentration of Nups.

4.1.2 Binding affinity of NTF2 and FSFG

Although bound diffusion is the key parameter from our reaction-diffusion model of selectivity, the kinetic parameters of off-rate k_{off} , on rate k_{on} , and dissociation constant $K_D = k_{\text{off}}/k_{\text{on}}$ are also important. These parameters are surprisingly difficult to measure, yielding values between 10 nM and 10 μM depending on the experimental conditions. We estimated the dissociation constant

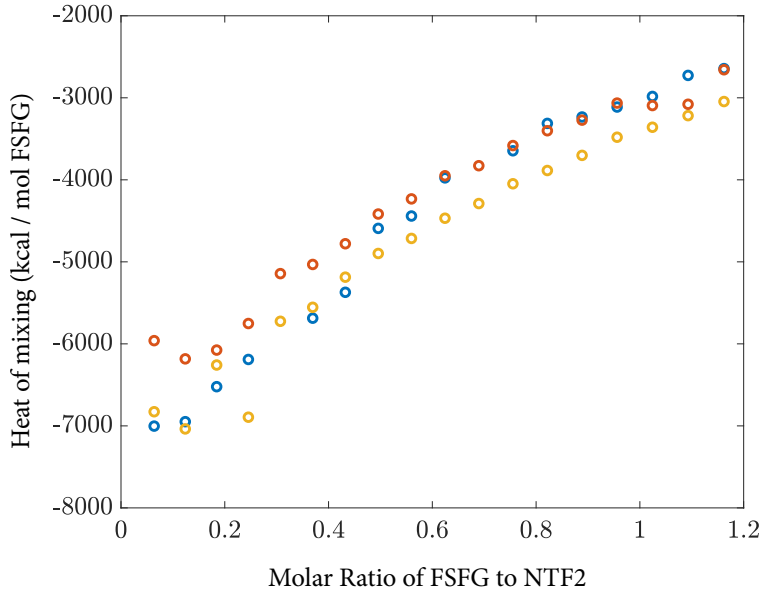


Figure 4.1: Isothermal calorimetry titration curve: heat of injection vs. molar ratio of FSFG to NTF2. Fits are questionable but multiple runs suggest $K_D \approx 200 \mu\text{M}$.

for NTF2 and FSFG concat-1 using isothermal titration calorimetry (ITC). The heat of injection was recorded as FSFG was titrated into a stock of NTF2. While the resulting titration curves had low signal-to-noise and did not reach saturation, they clearly indicated binding (Fig. 4.1). Simple fits are likely inaccurate, given the high degree of multivalent binding, but may provide an order-of-magnitude estimate of the affinity. Several ITC curves agree on a dissociation constant of $K_D \approx 200 \mu\text{M}$. This is roughly compatible with the millimolar per-FSFG constant measured by the Rout lab with NMR and ITC [27]. Similarly weak values were predicted through NMR, simulation, and stopped-flow anisotropy [26].

Due to the twin difficulties of varying K_D in a controlled way and accurately measuring its value, we did not attempt to experimentally alter this parameter. Ideally, a transport factor - Nup pair with $K_D \approx 1 \mu\text{M}$ would have been used to maximize selectivity. For the purposes of determining the bound diffusion constant, the only value that is necessary to measure is the ratio K_D/N_T , which can be estimated using the partitioning of transport factors and inert proteins into the FSFG hydrogels (Sec. 4.3.2). We investigated using the ubiquitin-associated (UBA) domain of the mRNA exporter Mex67 as a Nup-binding domain in GFP fusion proteins. In principle, varying numbers of this small (<10 kDa) domain could be added to GFP to explore the effect of varying binding affinity and valency in transport factors. The constructs GFP-UBA, GFP-UBAx2, and

GFP-UBAx3 were created by Eric Verbeke, but did not express and/or bind well.

4.1.3 Quantifying concentration of tethered Nups

Another potentially-tunable parameter of the bound-diffusion model is N_T , the total concentration of tethered Nups. It is straightforward to control the Nup concentration in the hydrogel precursor solution by resuspending a known mass of lyophilized protein. Nup concentrations up to ~ 50 mg/mL can be resuspended. However, it is much more difficult to determine how much protein was tethered to the hydrogel upon crosslinking.

BCA protein quantitation assays were used to place upper bounds on N_T . Two methods were attempted: incubating the hydrogel itself in the working reagent, and soaking the hydrogel in a known volume of buffer and testing the concentration of FSFG released. When applying the first method, the hydrogel was first soaked to remove excess precursor solution and thoroughly rinsed. The gel was placed into a 96-well plate and buffer added until the appropriate sample volume was reached. A standard BCA protocol was then followed. Upon incubation with the working reagent, the hydrogels turned purple, as expected. Standard absorption measurements and processing yielded an estimate of 0.5 mg/mL tethered FSFG-concat 1; this should be taken as an approximate value only. The second method, that of soaking hydrogels and measuring the FSFG released, placed a similarly-low upper bound on tethered FSFG concentration. Hydrogels made with 5 μ L of precursor solution were soaked in 45 μ L buffer to equilibrate. The buffer was then measured to have a concentration of 1.0 mg/mL FSFG, implying a tethered FSFG concentration of < 1 mg/mL.

The concentration of Nups within the pore may reach 100 mg/mL, depending on how compact the disordered FG Nups are. The low concentration of tethered Nups that we were able to achieve is therefore a major barrier to selectivity. It is likely that the disordered nature of FSFG makes the labeled end less accessible to the hydrogel scaffold than would be the case for an ordered protein. In an effort to overcome this limitation, we tested other linkers and conjugation methods. We conjugated the FSFG-cys to PEG-diacrylate of varying lengths (700 Da and 10 kDa), to multi-

armed PEG-diacrylate, and to maleimide-PEG-acrylate. While labeling was verified using Ellman's reagent (Appendix D), there was no noticeable difference in transport factor partitioning into these hydrogels.

4.1.4 Free diffusion constant

The final tunable parameter from the binding-diffusion model is the diffusion constant of the transport factor when it is not bound to a Nup, the free diffusion constant D_F . Decreasing D_F is predicted to increase a material's selectivity while decreasing the absolute flux of transport factor (Figs. 2.4, 2.5). The free diffusion is predominantly determined by the protein's size and the viscosity of the solution, according to the Stokes-Einstein equation $D = k_B T / 6\pi\eta R$, where $k_B T$ is the thermal energy, η the solution viscosity, and R the particle radius. The solution viscosity could potentially be increased using a viscous additive such as glycerol; however, these attempts appeared to interfere with the binding of NTF2 and FSFG.

The diffusion of the non-binding 30 kDa protein mCherry was used as a proxy for the free diffusion of similarly-sized NTF2 within the FSFG hydrogels.

4.2 Experimental procedures

The nuclear pore mimics in this dataset were designed with the lessons of Chapter 3 in mind. They consist of hydrogels with the largest average pore size and simplest geometry: a single microliter-scale droplet. While this geometry does not allow for direct measurements of selectivity, the in-gel diffusion constants of both NTF2 and mCherry can be determined and bound diffusion calculated. Two types of experiments were carried out: influx experiments, in which the entry of fluorescent proteins into the hydrogels was monitored, and FRAP experiments, in which a portion of an equilibrated hydrogel was bleached and the recovery observed. Both experiments provide a measurement of the proteins' diffusion constants. These experiments were performed at CU's BioFrontiers Advanced Light Microscopy Core Facility. Thanks go to Joseph Dragavon for much assistance with the microscopy.

4.2.1 Hydrogel preparation

Detailed precursor solution recipes are given in Appendix E. For the dataset analyzed in this chapter, all nuclear pore mimic hydrogels were 6% acrylamide and contained 2 mM LAP. The precursor was made with potassium transport buffer (PTB) and contained either FSFG concat-1 bis or FSFG concat-2 bis. Lyophilized FSFG-bis was resuspended in PTB, allowed to sit at room temperature for at least 20 minutes, and added to the precursor solution. After the precursor solution was thoroughly mixed, it was degassed in a vacuum desiccator for 10 minutes and immediately pipetted into a disassembled 400- μm -thick PDMS gasket chamber (Sec. 3.3). Drops between 0.5 and 2 μL were carefully pipetted onto the plastic slide and the chamber assembled around the drops. Typically, each chamber measured a few centimeters on a side and contained a control gel with no Nups as well as one or more Nup-filled gels. The chamber was then illuminated as uniformly as possible with 365 nm light at approximately 200 mW/cm² with a ThorLabs M365 LP1 LED. Condensation around the gels indicated that they had crosslinked. The chamber was immediately rinsed with at least 100 μL of PTB, filled with fresh PTB, and sealed with a PDMS slab and clingwrap. The gels were left to soak at 4°C for at least 12 hours so that any remaining precursor solution and protein could leave the gel.

4.2.2 Influx of transport factor and inert protein

After soaking in buffer, the buffer solution was removed by pipette or wicking with a Kimwipe and a fluorescent reservoir solution added. Aspirating the chamber was avoided if possible, as it sometimes disturbed the seal between the gel and the chamber. The reservoir solution contained 20 μM each freshly-thawed NTF2-fluorescein (NTF2-F) and mCherry in PTB. The chamber was resealed after adding the solution. If no influx experiment was planned, the gels were then allowed to equilibrate for 24 hours before FRAP was performed.

When influx experiments were run, they began as soon as possible after loading the reservoir solution. Videos were recorded at 4x magnification on an Olympus IX-81 widefield microscope

using FITC (excitation 464-500 nm / emission 516-556 nm) and TRITC (excitation 532-544 nm / emission 573-613 nm) filter cubes. Exposure times were typically 30-100 ms with 3-8 dB gain. Videos consisted of 120 frames at one frame per minute. Minimal photobleaching took place over the course of these experiments. After the influx experiment, the chamber was usually stored for equilibration 4°C, protected from light, and a FRAP experiment performed the following day.

Influx experiments on hydrogels containing FSFG show binding of NTF2-F to mCherry (Fig. 4.2). A bright wavefront of NTF2-F slowly progresses into the gel, while mCherry remains largely excluded. As expected, mCherry equilibrates more rapidly than does NTF2-F, due to the lack of binding. Influx experiments were analyzed as described in Sec. 4.4.

4.2.3 Fluorescence recovery after photobleaching

FRAP is typically performed using a confocal microscope, but we were able to bleach the hydrogels using an Olympus IX-81 widefield microscope. The widefield was preferable because the greater depth of field allowed for thicker hydrogel samples, which were easier to fabricate and manipulate. As described above, the hydrogel was first allowed to equilibrate with 20 μ M NTF2-F and mCherry in PTB. A reference image was taken at 4x magnification in both fluorescence channels. A circular region of the hydrogel around 300 μ m (?? check this) in radius was then photobleached by taking a five-second exposure at 40x magnification using a DAPI (excitation 352-402 nm / emission 417-477 nm) filter cube. Following the bleach, the 4x objective was rapidly returned and a time series recorded. Typical series consisted of 15-30 frames taken as rapidly as possible (5-10 s per frame), followed by 30-60 frames taken at a slower rate (1-2 minutes per frame). Total experiment time was 1-4 hours. Typical exposure times were 10 ms for NTF2-F and 40 ms for mCherry, both with a gain of 3 dB.

In order to increase throughput, up to three FRAP experiments were run concurrently by sequentially bleaching and then imaging several locations within a single chamber. This led to a maximum delay time of approximately 35 s between the end of the bleach segment and the beginning of the time series. Delay times were recorded and taken into account in the data processing.

Figure 4.2: Influx image series. A hydrogel containing a nominal 5 mg/mL FSFG concat-2 was challenged with 20 μ M NTF2-F and mCherry. The hydrogel shows selective entry of NTF2-F and has largely equilibrated within 24 hours.

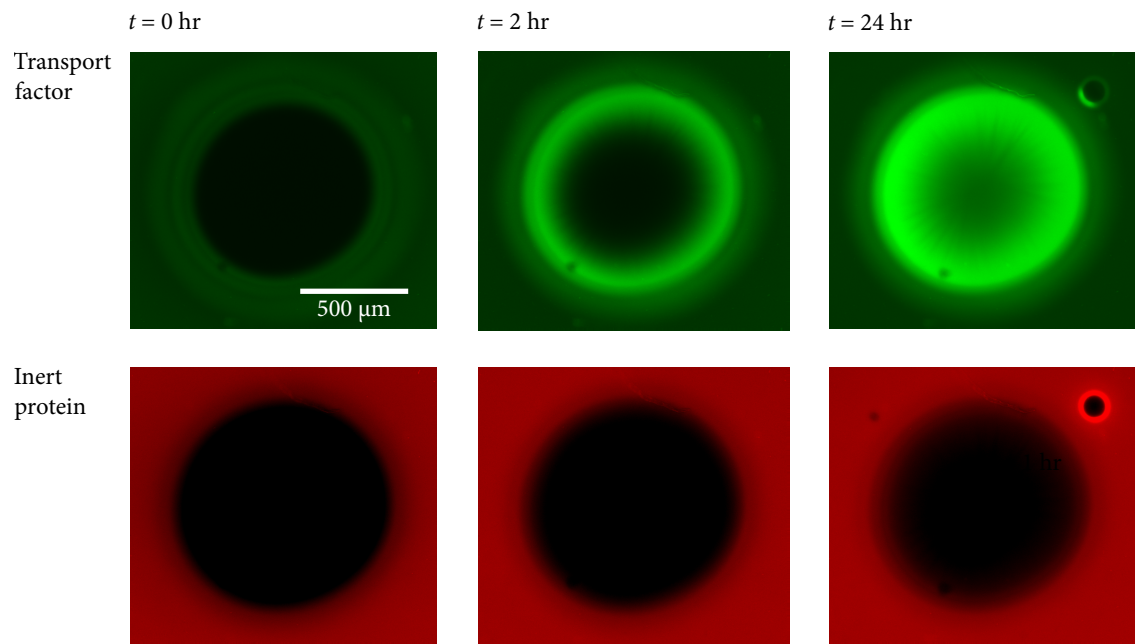


Figure 4.3 shows a representative series of images pre- and post-FRAP for both NTF2-F and mCherry.

Despite allowing 24 hours for equilibration, the fluorescence intensity across the hydrogel was not always uniform at the beginning of a FRAP experiment. This could be due to slow diffusion into the hydrogels, or to inhomogeneous crosslinking. The center of a hydrogel is more likely to be tightly crosslinked than the edges, as swelling is most inhibited at the center. Gels which were too inhomogenous to display a clear bleach spot were discarded, but many nonuniform hydrogels were used in the final dataset, with the lack of equilibrium addressed in the data analysis (Sec. 4.5). Smaller hydrogels ($0.5 \mu\text{L}$ of precursor solution) equilibrated more readily, at the cost of increasing the effect of fluorescent protein exchange with the reservoir, since the bleach spot then covered a significant fraction of the hydrogel. This effect was also taken into account during data analysis.

4.3 Steady-state hydrogel properties

Both the influx and FRAP experiments rely on steady-state properties of the hydrogel as well as time-dependent ones. These properties include the partition coefficients of transport factors and inert proteins, as well as some dependent on the geometry of the hydrogel.

4.3.1 Gel dimension estimates

Although the hydrogels were not perfectly circular, all analysis treated them as circular or nearly so. In total, the analysis made use of a gel's radius, center, perimeter, and area. I began by manually defining two masks: one that covered the entire gel, and one that covered only the bleach spot (Fig. 4.4). The gel area was calculated by summing all of the pixels in the gel mask and, where necessary, making use of the $1.58 \mu\text{m}$ per pixel scale of the Olympus 4x objective. The perimeter was calculated using Matlab's `bwperim` function, which takes a binary mask and returns a mask whose only nonzero entries are that mask's perimeter. Summing over these pixels and scaling provides the gel perimeter. It should be noted that in some cases the full area of the gel was not within the field of view. In these cases, sometimes the partial area in the field of view

Figure 4.3: FRAP image series. NTF2-FITC (top, green) and mCherry (bottom, red) bleaching and recovery shown separately. Hydrogel contained...

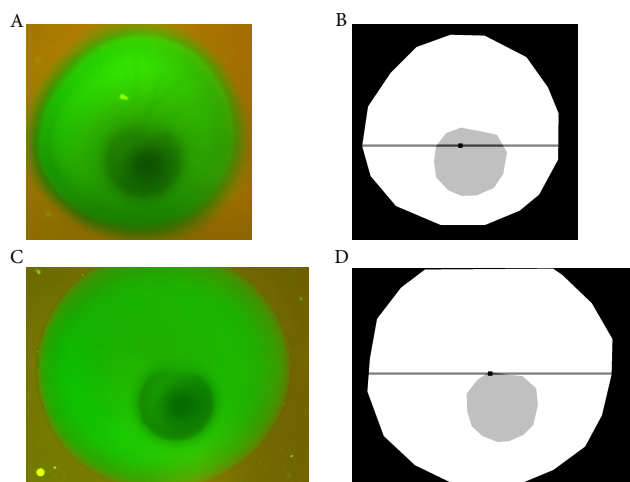
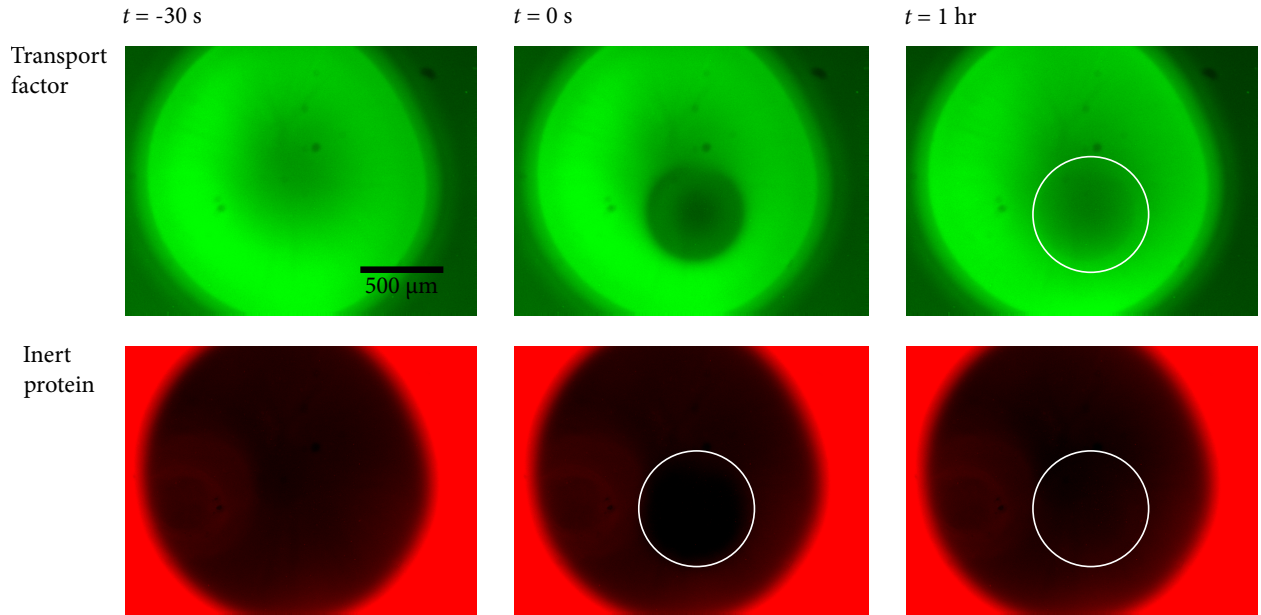


Figure 4.4: Sample hydrogel masks with radius and center calculations. (A) An equilibrated $0.5\text{-}\mu\text{L}$ hydrogel containing FSFG concat-1, immediately post-bleach. (B) The corresponding hydrogel mask (white), bleach spot mask (light gray), calculated gel diameter, and calculated gel center. (C)-(D) A $1\text{-}\mu\text{L}$ hydrogel, showing that the gel is not entirely within the field of view.

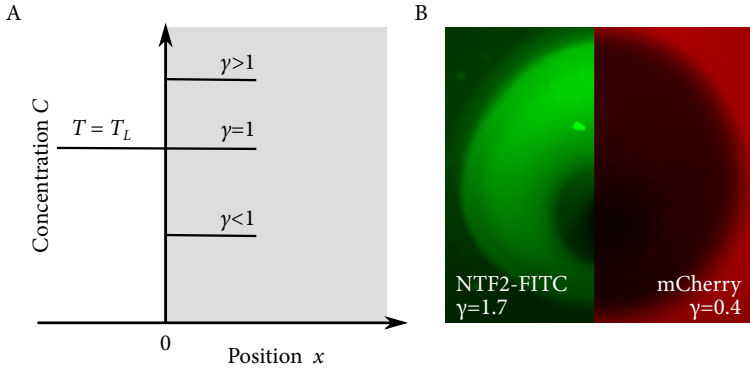


Figure 4.5: Partitioning of NTF2 and mCherry into FSFG hydrogel. (A) Partition coefficient γ depends on whether the hydrogel excludes or binds protein. (B) Equilibrated FSFG concat-1 hydrogel (nominally 10 mg/mL) showing partitioning of $T_L = 20 \mu\text{M}$ each NTF2-FITC and mCherry. Contrast adjusted for ease of viewing.

was used as the area estimate, and sometimes I embedded the gel image in a larger frame and estimated the remaining area when drawing the mask. Following sections indicate which method was used and the mathematical reasoning. However, all perimeter calculations were performed with the estimated full area.

The hydrogel radius was estimated taking the diameter to be the widest row of the gel mask. The widest row also set the y -coordinate of the gel center, with the x -coordinate calculated to be midway along the non-zero values for that row. As seen in Fig. 4.4, this is a quick and relatively crude method, but in almost all cases it works reasonably well. An advantage of this method is that it works even for hydrogels which do not fit in the vertical field of view.

4.3.2 Partition coefficients and fraction of time spent bound

The concentration of NTF2 and mCherry in a flow chamber's reservoir can be directly controlled, but the partitioning of a protein into the hydrogel depends on the degree to which the presence of the gel sterically excludes the protein, as well as on binding interactions between the gel and protein. When a transport-factor-sized inert protein is present to control for the steric effects, information about the transport factor's dissociation constant and fraction of time spent bound can be extracted from knowledge of the partition coefficient γ . In particular, p_B , the fraction of time spent bound, is necessary in order to calculate the bound diffusion coefficient.

As shown in Fig. 4.5A, the partition coefficient is the ratio of a protein's concentration in a well-equilibrated hydrogel to that in the surrounding reservoir. This quantity is calculated by

dividing the average intensity of the gel by that of the reservoir within the field of view (Fig. 4.5B). If the gel is not fully equilibrated, the partition coefficient can be estimated using a line scan through the reservoir and gel, though this will likely underestimate the true value.

When the system is in chemical equilibrium, the concentration of free transport factor (T), free Nup (N), and transport factor - Nup complex (C) is related to the dissociation constant K_D by $K_D = NT/C \approx N_T T/C$ in the linear approximation $N \approx N_T$. The total tethered Nup concentration, both free and bound, is the constant N_T . The fraction of transport factors that are bound is then given by

$$p_B = \frac{C}{C + T} = \frac{C}{C + \frac{CK_D}{N_T}} = \frac{1}{1 + \frac{K_D}{N_T}} \quad (4.1)$$

To relate this expression to measureable quantities, write the protein concentrations within the hydrogel in terms of their partition coefficients. The concentration c_0 of the inert protein and the transport factor is equal in the reservoir. If γ_T is the partition coefficient of the transport factor and γ_I that of the inert protein, then the transport factor concentrations can be expressed as

$$T = \gamma_I c_0 \quad (4.2)$$

$$C = T_T - T = \gamma_T c_0 - \gamma_I c_0 \quad (4.3)$$

The total transport factor concentration within the gel is $T_T = T + C$ and is a constant. Therefore, within the gel, the chemical equilibrium condition can be expressed as

$$\frac{K_D}{N_T} = \frac{T}{C} = \frac{\gamma_I c_0}{\gamma_T c_0 - \gamma_I c_0} = \frac{\gamma_I}{\gamma_T - \gamma_I} \quad (4.4)$$

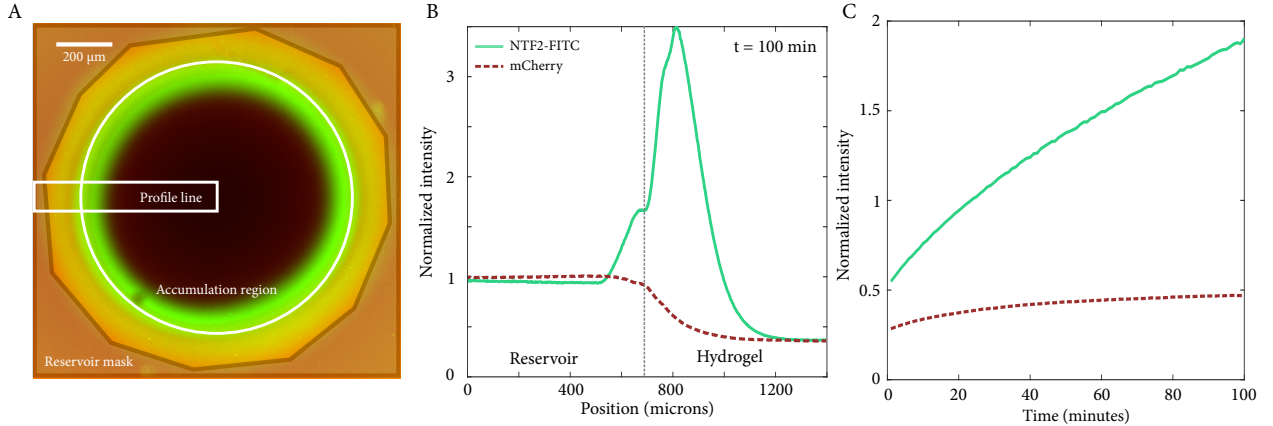
Combining Eqns. 4.1 and 4.4, the bound probability can be expressed in terms of the partition coefficients as

$$p_B = \frac{1}{1 + \frac{K_D}{N_T}} = \frac{1}{1 + \frac{\gamma_I}{\gamma_T - \gamma_I}} = 1 - \frac{\gamma_I}{\gamma_T} \quad (4.5)$$

4.3.3 Bound-diffusion calculation

Once the observed diffusion constants for NTF2 and mCherry have been calculated, along with the fraction of time spent bound p_B , the bound diffusion is given straightforwardly by the

Figure 4.6: Intensity profiles and total accumulation within hydrogel as determined from influx time series. (A) Image of an FSFG concat-2 hydrogel with a nominal Nup concentration of 10 mg/mL. Reservoir contains 20 μ M NTF2-F and mCherry in PTB. Reservoir mask is shown (red polygon) as well as accumulation area and rectangle over which the profile averaging was performed. (B) Normalized intensity profiles as calculated using the box in (A). (C) Normalized average intensity within hydrogel.



weighted average

$$D_{\text{obs,TF}} = p_B D_B + (1 - p_B) D_F \quad (4.6)$$

This result assumes Fickian diffusion. In reality the diffusion will be slightly anomalous due to binding and the presence of the hydrogel. However, the binding is highly transient and the hydrogel relatively permeable to proteins of the size of NTF2 and mCherry (Sec. 3.6).

Taking the free diffusion coefficient of the transport factor to be approximately equal to the observed diffusion of the inert protein ($D_F = D_{\text{obs,I}}$), the bound diffusion coefficient of the transport factor is

$$D_B = \frac{D_{\text{obs,TF}} - (1 - p_B) D_{\text{obs,I}}}{p_B} \quad (4.7)$$

Note that neither the dissociation constant or the total Nup concentration need to be measured independently in order to calculate the bound diffusion constant.

4.4 Influx analysis

After recording a time series of fluorescent protein influx into a hydrogel, diffusion constants can be estimated using either a plot of the intensity profile across the gel or a plot of total accu-

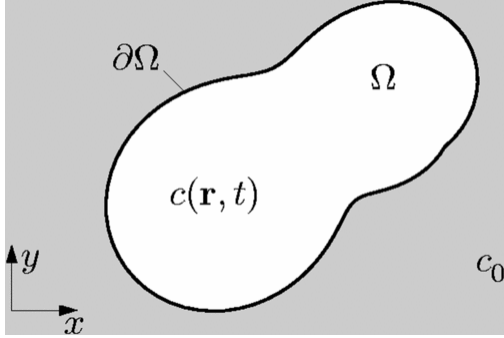


Figure 4.7: Geometry used to solve diffusion equation in [140]. The reservoir concentration c_0 fixed the concentration at the edge of the region Ω . The concentration $c(\mathbf{r}, t)$ is determined within Ω as a function of position and time.

mulation within the gel. Figure 4.6 shows an example of each plot. The intensity within the gel is normalized to the average intensity of the reservoir, as calculated using the mask shown in Fig 4.6A. Therefore, each profile trace begins at $I = 1$ within the reservoir and either dips or rises to the partition coefficient value within the gel. As the gels are not equilibrated, much of the gel interior shows only background fluorescence. Likewise, the average intensity within the hydrogel trends towards the partition coefficient but does not reach it on the time scale of an average experiment.

Analysis of the accumulation and profile curves used the diffusion-equation solutions described by Mortensen, Okkels, and Bruus [140]. This method assumes that the edge of a nearly-circular two-dimensional region is held at a fixed concentration while the interior equilibrates (Fig. 4.7). Such boundary conditions correspond to an infinite fluorophore reservoir. Given that our reservoirs are 10-20 times larger than the hydrogel volume, this is a reasonable assumption. In a slight modification, we allow for an arbitrary partition coefficient γ by taking the fixed boundary concentration c_0 to be γT_0 , where T_0 is the fluorescent protein intensity in the reservoir. The assumption of near-circularity is also a good one.

The two most troublesome restrictions of the Mortensen equations are Fickian diffusion and the homogeneity of the hydrogel. As discussed in Sec. 2.5, the presence of the hydrogel meshwork and binding make diffusion within the hydrogels slightly anomalous. Additionally, despite the improvements to the fabrication protocol, the hydrogels likely contain some degree of nonuniformity in their density, with the centers most likely being slightly denser than the edges due to differential swelling. The effects of swelling and non-uniform thickness are greatest at the gel edge. Unfortunately, the points at the edge of the gel and earliest in the experiment are the most important to

the following fits. As a result, the diffusion constants extracted using the profile and accumulation plots are not reliable. The analysis is presented below nonetheless, as a similar approach was taken in analyzing the FRAP experiments.

4.4.1 Profile analysis

Mortensen *et al* first define a characteristic timescale for equilibration $\tau = (\mathcal{A}/\mathcal{P})^2(\pi/4D)$ where \mathcal{A} and \mathcal{P} are the area and perimeter, respectively, of Ω . For a circle $\mathcal{A}/\mathcal{P} = a/2$, but this ratio was numerically calculated for the hydrogels (Sec. 4.3.1). For times $t \ll \tau$, the concentration profile as a function of the distance r from the gel center can be approximated as

$$c(r, t) = c_0 \operatorname{erfc} \left(\frac{r}{\sqrt{4Dt}} \right) \quad (4.8)$$

where D is the diffusion constant.

The typical duration of an influx experiment was approximately τ , making the short-time approximation questionable throughout most of the time series. We attempted to fit the intensity profile (Fig. 4.8) and obtained fits with fairly low error but with unreliable fit parameters. In addition to the issues of timescale, it was often difficult to determine where the gel edge was located, as well as the partition coefficient. Given these problems, it is not surprising that fits at successive timepoints yielded incompatible values of diffusion constant for both mCherry and NTF2. A similar problem prevented the use of diffusion constants obtained from intensity fits at a fixed position over time (Fig. 4.9).

A more exact solution for $c(r, t)$ can be written if the gel is assumed to be circular. Mortensen *et al* quantify the error introduced by small deviations from circularity and find it to be small. Assuming a circular gel, the concentration profile at an arbitrary time t is given by

$$\frac{c(r, t)}{c_0} = 1 - 2 \sum_{n=0}^{\infty} \frac{J_0(\alpha_n r)}{\alpha_n a J_1(\alpha_n a)} \exp(-\alpha_n D t) \quad (4.9)$$

where a is the gel radius and $\alpha_n a$ is the n th zero of the Bessel function of the first kind J_0 .

I fit the intensity profiles to Eqn. 4.9 using different numbers of terms N . For the mCherry curves, the resulting fit parameters tended to converge as N increased, and the RMSE stabilized.

Figure 4.8: Fits to Eqn. 4.8 near the beginning of the influx experiment for (A) mCherry and (B) NTF2-Alexa488 intensity profiles. Hydrogel nominally contains 10 mg/mL FSFG-PEGDA 700 kDa. The entire intensity profile is shown in the top panel with the portion used for fitting highlighted in red. Approximate locations of the gel edge, background fluorescence level, and partition coefficient are also shown.

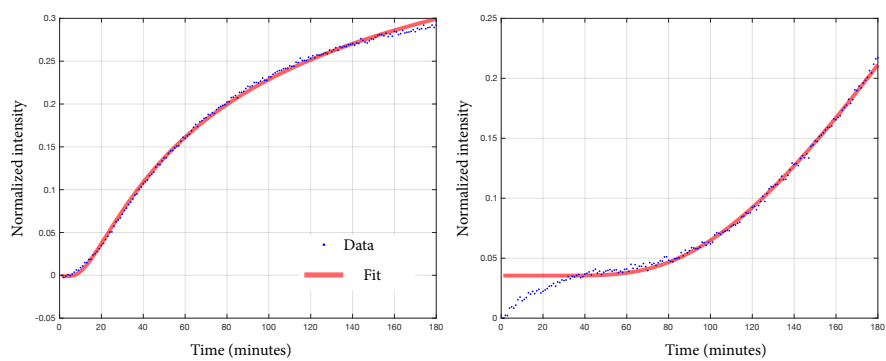
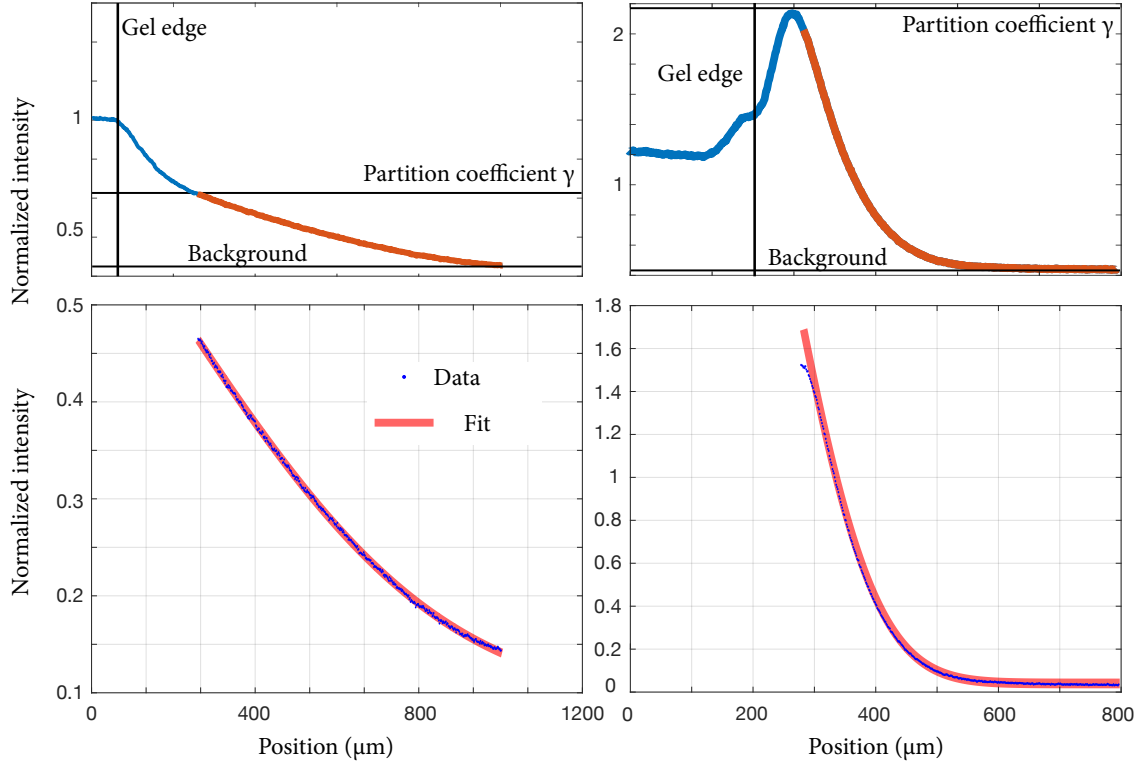


Figure 4.9: Fits to Eqn. 4.8 at a fixed point near the gel edge for (A) mCherry and (B) NTF2-Alexa488 intensity profiles. The short-time approximation likely only holds for times $t \lesssim 20$ minutes. Hydrogel nominally contains 10 mg/mL FSFG-PEGDA 700 kDa.

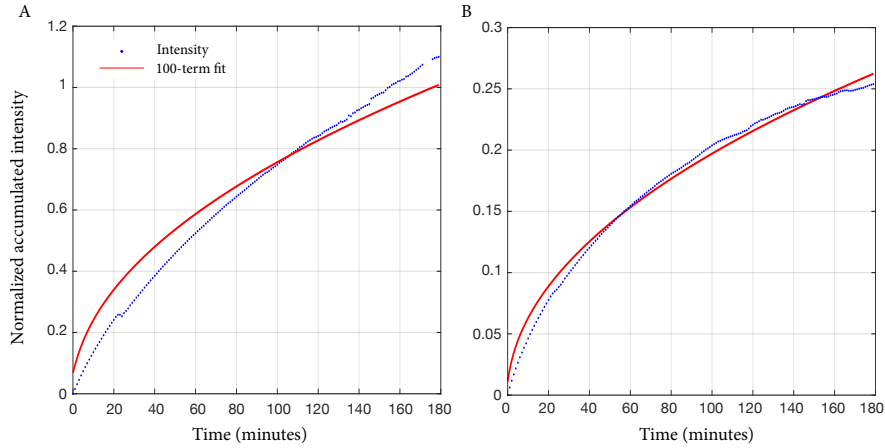


Figure 4.10: Accumulation fits to Eqn. 4.10 for (A) mCherry and (B) NTF2-Alexa488. Hydrogel nominally contains 10 mg/mL FSFG-PEGDA 700 kDa.

However, neither was true for the NTF2 curves. Increasing values of N led to steadily decreasing values of diffusion constant. This may be due to the effect of binding on NTF2 diffusion.

4.4.2 Accumulation analysis

The total accumulation within the hydrogel can be modeled by integrating the concentration profile over the entire gel. When this is done, the averaged intensity within the hydrogel $N(t)$ is found to be

$$\frac{N(t)}{N_0} = 1 - \sum_{n=0}^{\infty} \frac{4}{(\alpha_n a)^2} \exp\left(-\frac{(\alpha_n a)^2 \pi t}{16\tau}\right) \quad (4.10)$$

where N_0 is the equilibrium value, here equal to the partition coefficient γ once the intensity has been normalized to that of the reservoir.

Fits to the first 100 terms of Eqn. 4.10 are shown in Fig. 4.10 for mCherry and NTF2. These fits had systematic error, likely for the same reasons as the profile fits.

While the profile and accumulation data do contain information on the diffusion constants of NTF2 and mCherry, I was unable to reliably extract that information using the influx experiments. The model presented above is a remarkably good match to the experimental setup except for the presence of binding and the unpredictable gel-edge effects. The FRAP experiments overcome the problem of edge effects by making use of equilibrated regions deep within the hydrogel.

4.5 FRAP analysis

4.5.1 Accounting for photobleaching

Small but noticeable amounts of photobleaching occur over the course of the FRAP experiment. In order to correct for photobleaching, the intensity of the bleached spot must be normalized to that of the entire gel, including the bleached region. The normalized intensity used to fit the recovery curves is given by

$$N(t) = \frac{c_b(t)}{c_g(t)} \quad (4.11)$$

where the average intensity of the bleach spot is $c_b(t) = C_b(t)/A_b$. The total intensity within the bleach spot is $C_b(t)$ and A_b is the area of the spot as shown in Fig. 4.4. The average intensity of the entire gel $c_g(t)$ is defined similarly. Using this normalization removes the effects of photobleaching, as verified by simulating recovery data with various photobleaching rates.

4.5.2 No-exchange solution to diffusion equation

The simplest realistic model of fluorescence recovery assumes that the hydrogel is perfectly uniform and equilibrated, that the presence of the gel is unimportant, and that there is no exchange of fluorescent proteins between the hydrogel and the reservoir during the experiment. Upon making those assumptions, the recovery curve can be fit using a sum of two Bessel functions as described in [67, 136]. The model used in [136] distinguishes between binding affinity regimes; NTF2-FSFG binding is sufficiently transient that it falls into the effective diffusion regime, allowing standard diffusion equations to be used without modification to calculate an effective diffusion constant as described in Sec. 4.3.3. The solution to fluorescence recovery with effective diffusion is given by

$$N(t) = A \exp(-\tau_D/2t) (I_0(\tau_D/2t) + I_1(\tau_D/2t)) + C \quad (4.12)$$

where the diffusion lifetime τ_D is related to the diffusion constant by $D = w^2/\tau_D$ if w is the bleach spot radius.

The amplitude A and offset C are related to the bleach depth (given by C) and final recovered

value (given by $A + C$). Typical bleach depths were 5-10% of the initial intensity and tended to be smaller for mCherry than for NTF2. In principle, the final recovered value reflects the immobile fraction of fluorophore. If there is an immobile fraction, the bleached region will not recover to its intial value. Given the weak binding between NTF2 and FSFG, we do not expect an appreciable immobile fraction of either NTF2 or mCherry. For the most part, the hydrogels appear to recover to their initial value. A few do not, for reasons that are unclear even after accounting for photobleaching.

The no-exchange model fits well to the larger hydrogels and those that are well-equilibrated. Many of the large gels, however, were not fully equilibrated even after a 24 hour incubation with the reservoir solution. The concentration within these gels will change over the course of the experiment as they continue to equilibrate. Smaller hydrogels were quicker to uniformly equilibrate; however, these gels are small enough that exchange of fluorescent proteins with the reservoir is important over the timescale of FRAP recovery. Both of these problems can be accounted for using a more thorough solution to the diffusion equation.

4.5.3 Fourier transform solution to diffusion equation

To account for exchange of fluorescent proteins with the reservoir, as well as for incomplete equilibration, some of the assumptions of the previous section must be relaxed. In particular, the assumption of radial symmetry must be abandoned. In order to incorporate angular as well as radial dependence, the solution must be written as a sum over Bessel function and cosine modes. While such a solution is cumbersome, it allows for an accurate description of the concentration throughout the hydrogel immediately post-bleach. Additionally, the boundary condition can be defined so as to allow exchange between the hydrogel and reservoir.

This analysis begins by numerically calculating the two-dimensional polar Fourier transform of the initial concentration distribution within the gel, decomposing it into a finite number of modes weighted by their contribution to the image. These mode coefficients are then used to create the equation to which the experimentally-measured recovery curve is fit. The fit parameters include

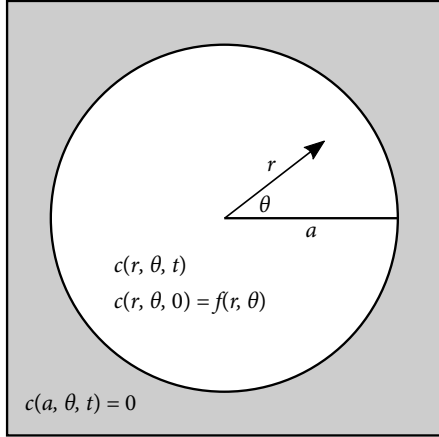


Figure 4.11: Geometry for diffusion-equation solution Eqn. 4.13. A circle of radius a is centered at the origin. The boundary $r = a$ is held at concentration $c = 0$ and the interior has initial concentration profile $f(r, \theta)$.

the observed diffusion coefficients for NTF2 and mCherry, allowing the bound diffusion constant to be determined as described in Sec. 4.3.3.

Scripts to perform the following calculations are available at <https://github.com/LauraMaguire/image-processing>.

4.5.3.1 Analytic series solution

The problem is that of diffusion in a circular region of radius a , centered at the origin, whose boundary is held at a fixed concentration. The region $r < a$ has an arbitrary initial concentration distribution $f(r, \theta)$ which consists of the first post-bleach image (Fig. 4.11). To find the concentration $c(r, \theta, t)$ for $r < a$, we used the Green's function integrals described in [141], as heat transfer obeys the same differential equation as diffusion of particles. Green's functions describe a system's response to an instantaneous point source. An initial distribution can be built by integrating the Green's function over the region of interest. The correct Green's function must be identified for a particular geometry and set of boundary conditions, but a formal solution is straightforward to write once they have been obtained.

As this solution is two-dimensional, two sums must be taken over the basis functions. Bessel functions J_ν of the first kind and integer order ν are the radial basis, and cosines are the angular basis. The time dependence is carried by decaying exponentials whose time constant is related to the diffusion coefficient D as well as to the zeros of the Bessel functions. The terms are summed

over the Bessel orders as well as over the zeros of each Bessel function. For our situation, the full solution to the diffusion equation within the hydrogel is given by [?]

$$c(r, \theta, t) = \sum_{\nu=-\infty}^{\infty} \sum_{\alpha=0}^{\infty} \frac{\exp(-D\alpha^2 t) J_{\nu}(\alpha r)}{(J'_{\nu}(\alpha a))^2} \times b_{\nu, \alpha} \int_0^{2\pi} \int_0^a \cos(\nu(\theta - \theta')) J_{\nu}(\alpha r') f(r', \theta') r' dr' d\theta' \quad (4.13)$$

where, as in the previous section, αa are the zeros of J_{ν} , and $b_{\nu, \alpha}$ are normalization constants defined in Sec. 4.5.3.2. Note that the sums run over all positive and negative integer Bessel orders and over all zeros of each Bessel function.

This solution applies to a circle whose boundary is held at $c = 0$, so it must be shifted by an offset in order to match the experimental concentration at the boundary. Note that the relevant boundary concentration is just within the hydrogel, not the concentration of the reservoir. The reservoir is assumed to be infinite, in order to maintain the hydrogel edge at its equilibrium concentration, but the concentration of the reservoir itself is irrelevant.

The integral above is difficult to use as written because it contains both primed and unprimed coordinates in the angular term, $\cos(\nu(\theta - \theta'))$. The unprimed coordinate can be removed from the integral using the identity

$$\cos(\phi_1 - \phi_2) = \cos \phi_1 \cos \phi_2 + \sin \phi_1 \sin \phi_2$$

The mode coefficients $C_{\nu, \alpha}$ and $S_{\nu, \alpha}$ can then be defined as

$$c(r, \theta, t) = \sum_{\nu=-\infty}^{\infty} \sum_{\alpha=0}^{\infty} \frac{\exp(-D\alpha^2 t) J_{\nu}(\alpha r)}{(J'_{\nu}(\alpha a))^2} (C_{\nu, \alpha} \cos(\nu \theta) + S_{\nu, \alpha} \sin(\nu \theta)) \quad (4.14)$$

with

$$C_{n, \alpha} = b_{\nu, \alpha} \int_0^{2\pi} \int_0^a \cos(\nu \theta') J_{\nu}(\alpha r') f(r', \theta') r' dr' d\theta' \quad (4.15)$$

$$S_{n, \alpha} = b_{\nu, \alpha} \int_0^{2\pi} \int_0^a \sin(\nu \theta') J_{\nu}(\alpha r') f(r', \theta') r' dr' d\theta' \quad (4.16)$$

The problem is reduced to determining the mode coefficients by evaluating the integrals.

4.5.3.2 Calculating mode coefficients

Before mode coefficients can be calculated using Eqns. 4.15 and 4.16, the normalization constants $b_{\nu,\alpha}$ must be determined. To find an expression for them, begin with Eqn. 4.23 at $t = 0$, when $c(r, \theta, 0) = f(r, \theta)$.

$$f(r, \theta) = \sum_{\nu=-\infty}^{\infty} \sum_{\alpha=0}^{\infty} \frac{J_{\nu}(\alpha r)}{(J'_{\nu}(\alpha a))^2} (C_{\nu,\alpha} \cos(\nu\theta) + S_{\nu,\alpha} \sin(\nu\theta)) \quad (4.17)$$

This expression for $f(r, \theta)$ can be substituted into Eqns. 4.15 and 4.16. Using the cosine coefficients as an example,

$$\begin{aligned} C_{n,\alpha} &= b_{\nu,\alpha} \int_0^{2\pi} \int_0^a \cos(\nu\theta') J_{\nu}(\alpha r') \times \\ &\quad \left[\sum_{\mu=-\infty}^{\infty} \sum_{\beta=0}^{\infty} \frac{J_{\mu}(\beta r')}{(J'_{\mu}(\beta a))^2} (C_{\mu,\beta} \cos(\mu\theta') + S_{\mu,\beta} \sin(\mu\theta')) \right] r' dr' d\theta' \\ C_{n,\alpha} &= b_{\nu,\alpha} \sum_{\mu=-\infty}^{\infty} \sum_{\beta=0}^{\infty} \int_0^{2\pi} \int_0^a \cos(\nu\theta') \frac{J_{\nu}(\alpha r') J_{\mu}(\beta r')}{(J'_{\mu}(\beta a))^2} \times \\ &\quad (C_{\mu,\beta} \cos(\mu\theta') + S_{\mu,\beta} \sin(\mu\theta')) r' dr' d\theta' \\ C_{n,\alpha} &= b_{\nu,\alpha} \int_0^{2\pi} \int_0^a \frac{J_{\nu}^2(\alpha r')}{(J'_{\nu}(\alpha a))^2} (C_{\nu,\alpha} \cos^2(\nu\theta') + S_{\nu,\alpha} \cos(\nu\theta') \sin(\nu\theta')) r' dr' d\theta' \end{aligned}$$

The integral and sum have been switched and the orthogonality of the basis functions used to collapse the sums. The integral of the $S_{\nu,\alpha}$ term vanishes, as it is an odd function ($\cos(\nu\theta') \sin(\nu\theta')$) integrated over all θ' . Similarly, the $C_{\nu,\alpha}$ term drops from the sine coefficient integral. The remaining term gives

$$C_{n,\alpha} = b_{\nu,\alpha} \int_0^{2\pi} \int_0^a \frac{J_{\nu}^2(\alpha r')}{(J'_{\nu}(\alpha a))^2} C_{\nu,\alpha} \cos^2(\nu\theta') r' dr' d\theta'$$

or finally

$$\frac{1}{b_{\nu,\alpha}} = \int_0^{2\pi} \int_0^a \frac{J_{\nu}^2(\alpha r') \cos^2(\nu\theta')}{(J'_{\nu}(\alpha a))^2} r' dr' d\theta' \quad (4.18)$$

So long as the integral is truly over the entire circle $r < a$, this constant is the same for both $C_{\nu,\alpha}$ and $S_{\nu,\alpha}$. In that case, Eqn. 4.18 gives $b_{\nu,\alpha} = 2/\pi a^2$ for every mode.

However, in many cases, it is not possible to numerically integrate over the entire gel, as seen in Fig. 4.4D. All numerical integrals are instead over the gel mask, which encompasses as much of

the gel as fits into the field of view. The value of this mask is one within the gel and zero outside, so it serves to define the limits of numerical integration. Denoting the area covered by this mask as Ω , the normalization constants for $C_{\nu,\alpha}$ and $S_{\nu,\alpha}$, respectively, are

$$1/b_{\nu,\alpha}^C = \int_{\Omega} \frac{J_{\nu}^2(\alpha r') \cos^2(\nu\theta')}{(J'_{\nu}(\alpha a))^2} r' dr' d\theta' \quad (4.19)$$

$$1/b_{\nu,\alpha}^S = \int_{\Omega} \frac{J_{\nu}^2(\alpha r') \sin^2(\nu\theta')}{(J'_{\nu}(\alpha a))^2} r' dr' d\theta' \quad (4.20)$$

Likewise, the numerical integrals in Eqns. 4.15 and 4.16 are more precisely written

$$C_{n,\alpha} = b_{\nu,\alpha}^C \int_{\Omega} \cos(\nu\theta') J_{\nu}(\alpha r') f(r', \theta') r' dr' d\theta' \quad (4.21)$$

$$S_{n,\alpha} = b_{\nu,\alpha}^S \int_{\Omega} \sin(\nu\theta') J_{\nu}(\alpha r') f(r', \theta') r' dr' d\theta' \quad (4.22)$$

The degree to which the resulting coefficients deviate from the ideal case of a perfect circle can be roughly quantified by the ratio $b_{\nu,\alpha}/(2/\pi a^2) = \pi a^2 b_{\nu,\alpha}/2$. For small hydrogels, which entirely fit into the field of view, these values range from 1.01 to 1.03, signifying deviations of up to 3%. Large hydrogels whose top and bottom were cut from the field of view had deviations of up to 10%. However, using Eqns. 4.19 and 4.19 instead of the uniform mode weighting $b_{\nu,\alpha} = 2/\pi a^2$ should compensate for the irregular area of integration.

For every hydrogel, Bessel order ν , and Bessel zero α , mode coefficients were calculated numerically. The polar coordinates (r, θ) were converted to Cartesian (x, y) and a sum taken over all the pixels of the initial post-bleach image $f(x, y)$, using the hydrogel mask to set the limits. The center of the coordinate system was set at the center of the gel and the value of the gel radius a calculated as described in Sec. 4.3.1. Before the sum was calculated, the average intensity of the equilibrated portions of the hydrogel was subtracted from the entire image, effectively setting the equilibrium concentration at $c = 0$ as required by the series solution.

The sum was scaled using the area represented by each pixel (using the scale 1.58 $\mu\text{m}/\text{pixel}$) and normalized using the weighting constants $b_{\nu,\alpha}$. The final values of $C_{\nu,\alpha}$ and $S_{\nu,\alpha}$ were stored in two arrays for use in constructing the equation to which the experimental data was fit.

4.5.3.3 Reconstruction of initial image

To verify the mode coefficients, I reconstructed the initial post-bleach image from which they were calculated. The image was reconstructed by numerically integrating Eqn. 4.17 using a similar method to that discussed in the previous section. The area outside the gel mask was not reconstructed. Figure 4.12 shows the resulting reconstructions as the number of terms in the series increases. The relative magnitudes of those terms are plotted in Fig. 4.13. The reconstruction is adequate for our purposes by the time $N_\nu = 20$ and $N_\alpha = 20$, i.e. twenty Bessel orders and twenty zeros are used. Note that the Bessel orders are given by $\nu = -10, -9, \dots, 0, \dots, 8, 9$. A coefficient array of this size allowed a dataset of 43 hydrogels to be entirely processed and fit in approximately 24 hours on a desktop computer; larger coefficient arrays would require the use of a computing cluster.

4.5.3.4 Fitting recovery curves

Once the mode coefficients had been calculated, a fit string was constructed using the full series equation Eqn. 4.23 and fed into the Matlab curve fitter. Careful thought was required to ensure that the model was treated in the same way as the experimental data.

To begin, the mode coefficients were used to predict the average intensity of the bleach spot at each time point. Since the time dependence in each term is only in a decaying exponential, the average value of the bleach spot could be determined by integrating over the bleach spot:

$$\bar{c}_{\text{bleach}}(D, t) = \frac{1}{A_B} \sum_{\nu=-\infty}^{\infty} \sum_{\alpha=0}^{\infty} \exp(-D\alpha^2 t) \int_{\Omega_B} \frac{J_\nu(\alpha r)}{(J'_\nu(\alpha a))^2} (C_{\nu,\alpha} \cos(\nu\theta) + S_{\nu,\alpha} \sin(\nu\theta)) dA \quad (4.23)$$

where Ω_B is the region defined by the bleach-spot mask and A_B its total area. The Bessel function derivative J'_ν was computed using the identity

$$J'_\nu(x) = \frac{1}{2} (J_{\nu-1}(x) - J_{\nu+1}(x))$$

The average intensity of the entire gel, including the bleach spot, was determined in the same way, using the hydrogel mask instead of the bleach-spot mask. Both results were formatted as strings of sums, containing numerical values wherever possible as well as the diffusion constant parameter D (units of $\mu\text{m}^2/\text{s}$) and the time variable t , measured in seconds.

Figure 4.12: Reconstruction of initial concentration distribution. Reservoir is masked and not included. (A) Heatmap of original image with average equilibrated gel intensity set to zero. (B) Reconstruction using two Bessel orders ($N_\nu = 2$) and two zeros ($N_\alpha = 2$) in each order. (C-E) Reconstructions with $N_\nu = N_\alpha = 4, 10$, and 20 .

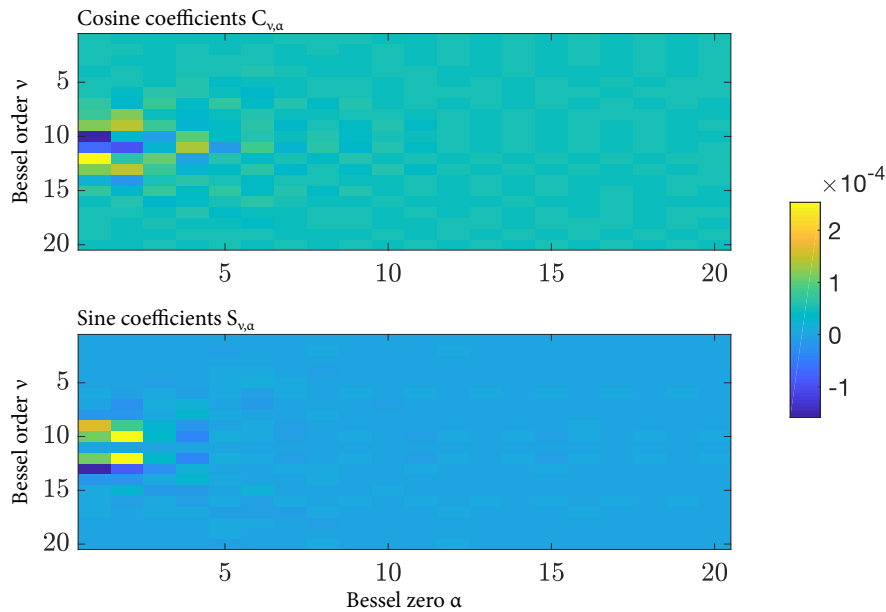
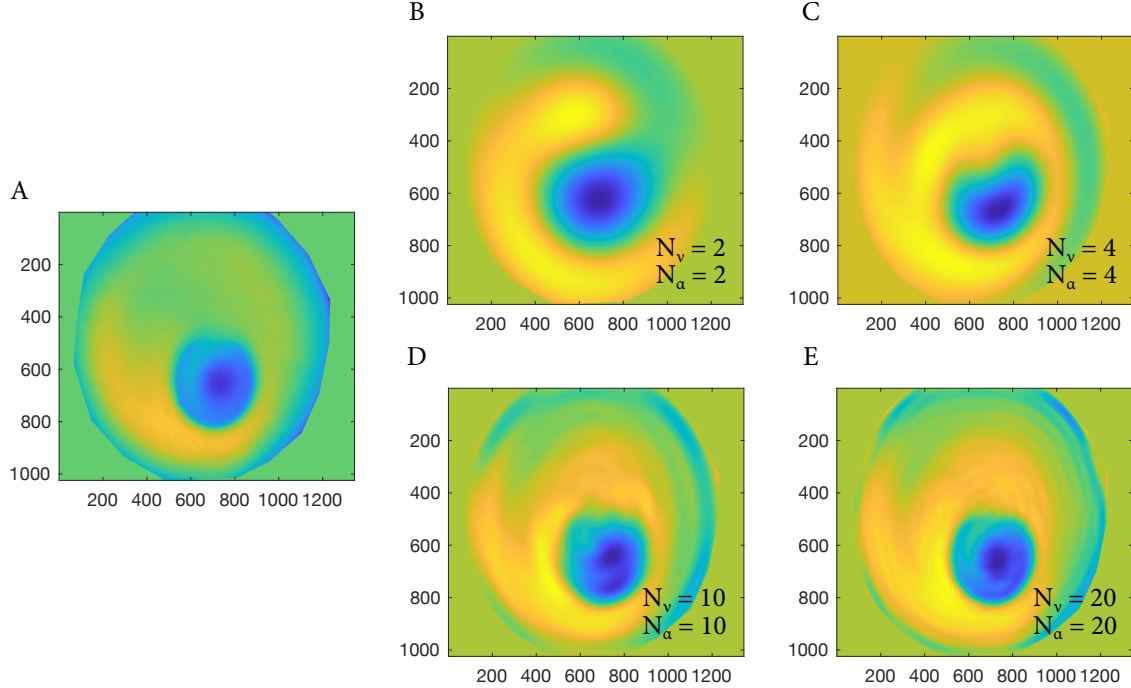
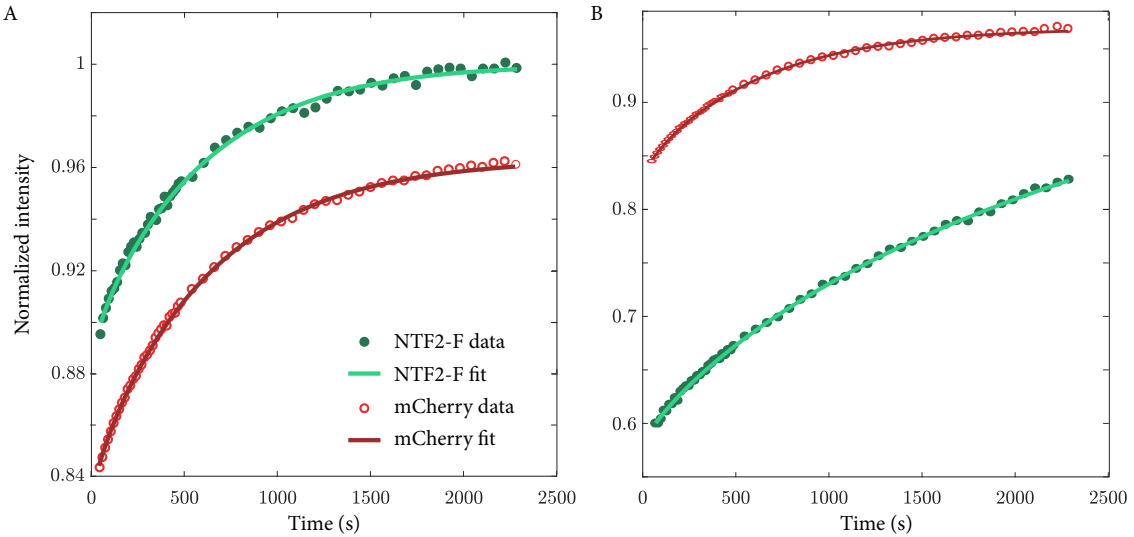


Figure 4.13: Heatmap of cosine and sine mode coefficients $C_{\nu,\alpha}$ and $S_{\nu,\alpha}$ for the reconstruction shown in Fig. 4.12E. Values are shown for each Bessel order ν and each zero α .

Figure 4.14: Fits using the series expansion Eqn. 4.13. (A) NTF2-F and mCherry recovery curves for a no-nup hydrogel. (B) NTF2-F and mCherry recovery curves for a hydrogel nominally containing 10 mg/mL FSFG concat-1.



Once these strings were created, the equilibrium concentration value c_0 was added back to both of them, and their ratio was taken, in order to mimic the data processing in Sec. 4.5.1. Mathematically, this gave a normalized string of

$$f(D, t) = \frac{\bar{c}_{\text{bleach}}(D, t) + c_0}{\bar{c}_{\text{gel}}(D, t) + c_0} \quad (4.24)$$

At this point, I checked the normalization by simulating data using the value of D calculated from the no-exchange analysis in Sec. 4.5.2. Often the simulated data matched the experiment to within 10%, but further fit parameters were needed in order to fit the data well. Ultimately, the function to which the data were fit was

$$g(c_1, c_2, D, t) = c_1 f(D, t) + c_2 \quad (4.25)$$

where c_1 and c_2 reflect the bleach depth and final recovered concentration similarly to A and C in Sec. 4.5.2. Their values are less important than that of the diffusion constant D .

Fits such as those shown in Fig. 4.14 were typical results. Values for c_1 and c_2 were of order unity, except for a few fits that were clearly incorrect and were omitted from the final dataset.

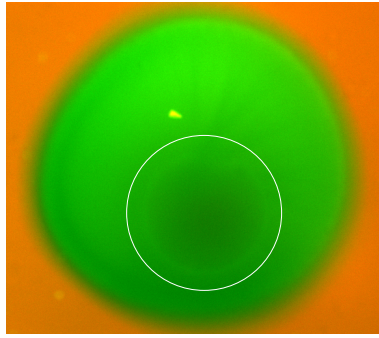


Figure 4.15: Bright NTF2-F ring surrounding photobleach spot, 70 minutes after bleaching. This ring often developed in FSFG concat-1 gels. Photo-bleach mask was chosen to be slightly smaller than the ring. Contrast adjusted for ease of viewing. While circle added to guide the eye.

4.6 Results

In all, FRAP analysis was performed on 36 hydrogels: 15 no-nup gels, 12 nominally containing 10 mg/mL FSFG concat-1, and 7 containing FSFG concat-2 nominally at 20 mg/mL.

Many of the FSFG concat-1 hydrogels showed an unusual bright ring in the NTF2-F channel around the photobleach spot which developed slowly after bleaching. Figure 4.15 shows an example. The ring is presumably due to photodamage by bleaching, but it is not clear why the edge of the bleach spot would exhibit increased NTF2-F binding. When hydrogels showed this bright ring, care was taken when drawing the bleach spot mask to exclude the ring entirely.

The partition coefficients for NTF2-F and mCherry are shown in Fig. 4.16 along with the corresponding fraction bound. As expected, the partition coefficients NTF2-F and mCherry are very similar in the no-nup hydrogels, while the NTF2-F partition coefficient increases for FSFG hydrogels due to binding. The FSFG concat-2 hydrogels show the highest NTF2-F partition coefficient, likely because there are more FG repeats in total. The fraction bound follows similar trends, although the difference between the FSFG concat-1 and concat-2 hydrogels is less pronounced. The fraction of NTF2-F bound to the no-nup hydrogels is indistinguishable from zero.

Figure 4.17 shows normalized recovery curves for all hydrogels in the dataset. In addition to the normalization described in Sec. 4.5.1, these curves were also scaled so that the pre-bleach average bleach spot intensity was one. Dark curves show the average NTF2 and mCherry recovery curves for each condition. The most obvious difference between conditions is the greater bleach depth for NTF2-F in FSFG hydrogels. Bleach depth stays roughly constant for mCherry between

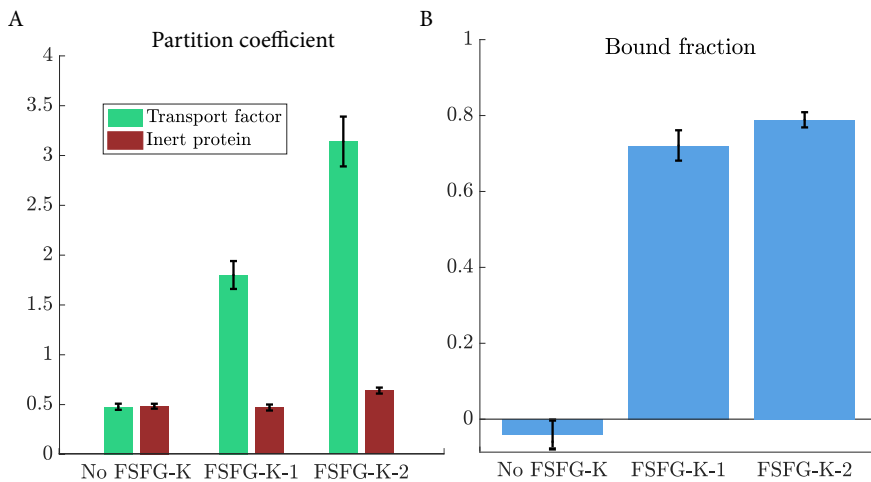


Figure 4.16: (A) Partition coefficients for NTF2-F and mCherry in each of the three experimental conditions. (B) Fraction of NTF2-F bound as calculated using Sec. 4.3.2. All errors are standard error of the mean.

conditions.

Finally, the observed diffusion constants for NTF2-F and mCherry were calculated using the Fourier series model. Mean values for each of the experimental conditions are shown in Fig. H.4 along with calculated bound diffusion constants. The observed diffusion for NTF2-F and mCherry was roughly equal in the no-nup hydrogels, but NTF2-F has a much lower diffusion constant in the FSFG conditions, due to binding. Two-tailed t-tests were conducted with the null hypothesis that $D_B = 0$. For FSFG concat-1, the resulting p-value was $p = 0.025$; for FSFG concat-2, it was $p = 0.13$. There is no distinguishable difference between D_B for FSFG concat-1 and FSFG concat-2, which may be due to the lack of sensitivity in our measurements.

4.7 Discussion

Our goal was to create a material in which we could measure and test the properties of bound diffusion. These results suggest that we can indeed measure non-zero bound diffusion, although there is no statistically significant difference between Nups of different lengths and valencies. Smaller effects would be measurable if the fraction of transport factor bound (p_B) increased, as then the contribution of bound diffusion to the observed diffusion would become more prominent. The most straightforward way of increasing the fraction bound is to increase the concentration of tethered Nups within the gel, a task which has proven difficult. However, this dataset still provides

Figure 4.17: Recovery curves for (A) no-nup, (B) FSFG concat-1, and (C) FSFG concat-2 hydrogels. All curves are shown for both NTF2-F and mCherry. Dark lines are averaged curves. Pre-bleach intensity set to one.

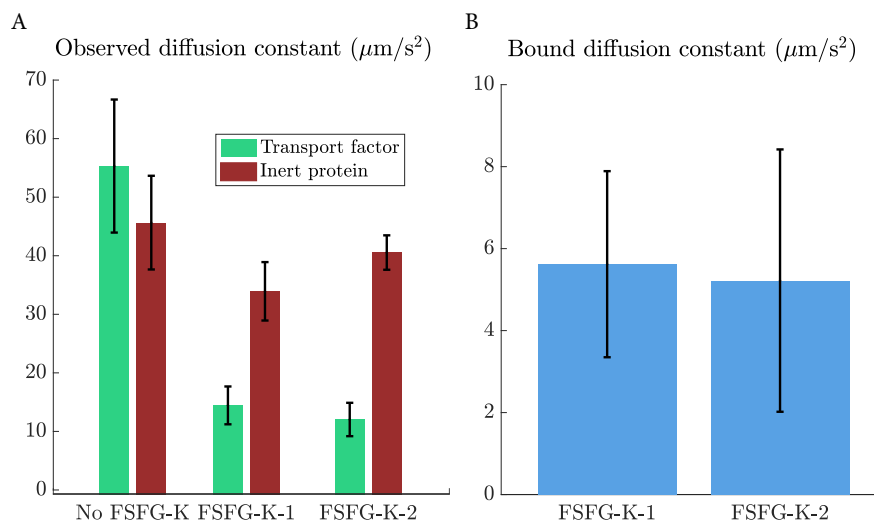
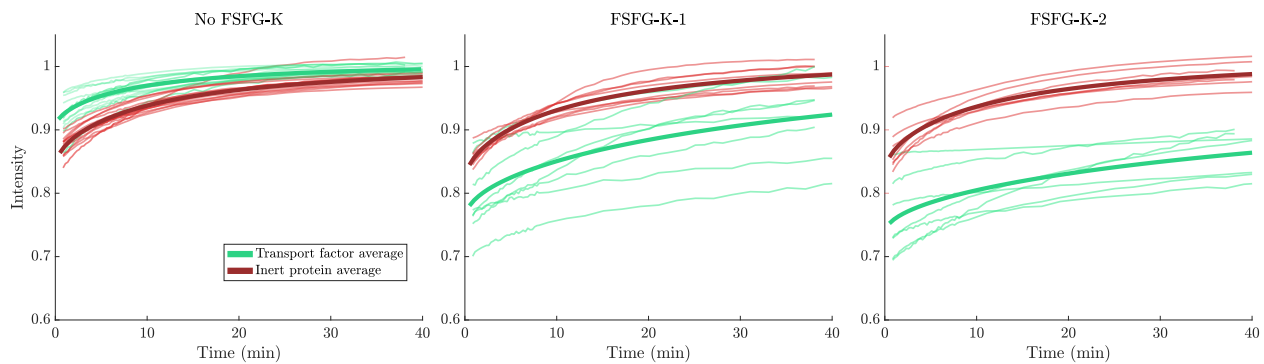


Figure 4.18: (A) Observed diffusion constant for NTF2-F and mCherry in each of the three experimental conditions. (B) Calculated values of the bound diffusion constant D_B for NTF2-F in the FSFG hydrogels. All errors shown are standard error of the mean.

a check on the predictions of our model.

Our bound-state diffusion model can predict the values of bound diffusion constant D_B that we expect to observe, provided we input an estimate of the off-rate k_{off} and assume that tethered diffusion the only mechanism of bound-state mobility (Appendix H). Taking $K_D \approx 0.5$ mM for FSFG concat-1 and $K_D \approx 0.4$ mM for FSFG concat-2, we can predict D_B for each FSFG hydrogel [27]. For FSFG concat-1 hydrogels, the predicted bound diffusion constant is $D_B = 6.9 \pm 0.3 \mu\text{m}^2/\text{s}$; for FSFG concat-2 gels this value is $D_B = 9.3 \pm 0.3 \mu\text{m}^2/\text{s}$. These values are consistent with our measured mean values of $D_B = 5.6 \pm 2.3 \mu\text{m}^2/\text{s}$ for FSFG concat-1 gels and $D_B = 5.2 \pm 3.2 \mu\text{m}^2/\text{s}$ for FSFG concat-2 gels. However, the large standard error in our measurements suggests that better measurements are needed before we can strongly state that our model has accurately predicted the bound diffusion constant.

Future work could productively focus on more precisely measuring the bound diffusion constant for transport factors interacting with Nups of various length and binding valency. We expect that longer Nups should lead to higher bound diffusion. If other experimental parameters such as total Nup concentration, binding affinity, and free diffusion constant can be varied in a controlled way, other predictions of the bound-diffusion model could be tested. Additionally, other systems of transient binding could be tested using these hydrogel models to determine how universal bound diffusion is in biological systems [142–144].

The hydrogel nuclear pore mimics discussed in this chapter do not reproduce the selectivity properties of nuclear transport; the tethered Nup concentration is too low and the transport factor - Nup dissociation constant is too high. However, they do provide a platform from which to measure bound diffusion. Non-zero bound diffusion of transport factors was measured when Nups were tethered to the hydrogel. This represents a first step towards understanding the effect of bound diffusion on selective biofilters.

Chapter 5

FG Nup aggregation under crowded conditions

Disordered proteins are often prone to aggregation, often causing disease, and the aggregation behavior of FG Nups is important to understand. It is not clear what the aggregation state of Nups is within the pore or how their aggregation might play into nuclear transport [?]. *In vitro*, many Nups spontaneously aggregate into amyoids over the course of a few hours, but there is evidence that this aggregation does not happen in the cellular environment [?, 49]. We investigated aggregation behavoir of an aggregation-prone Nup fragment in a number of different crowders. Inert crowders such as PEG and PVP help mimic the extremely crowded cellular environment, but they may interact different with the protein than nonspecifically-binding crowders such as cell lysate or BSA. We wanted to understand how different crowders affected the aggregation properties of Nups.

We used a 124-amino-acid fragment of the Nup Nsp1. The FG-repeat segment of Nsp1 contains an aggregation-resistant portion (used as the basis for the FSFG peptide) as well as one that aggregates in buffer over the course of a few hours. This aggregation-prone portion is the basis of the FG124 peptide used in the following aggregation experiments.

We used aggregation timecourses with thioflavin T as a readout, as well as fluorimetry, NMR, and x-ray scattering. Our conclusion is something about the phenylalanines and how they behave differently in when crowded with PEG than with PVP (which also has an aromatic ring).

need an intro kind of figure with amyloid structure, cartoon of aggregation

5.1 Fluorescence time courses

In order to probe the aggregation dynamics of FG124, we incubated samples in the presence of crowders and thioflavin T (ThT), a dye which is sensitive to the presence of amyloids. Over the course of several hours, FG124 aggregated and the fluorescence intensity from ThT increased. By recording the intensity at 10-minute intervals, we were able to plot sigmoidal aggregation curves for the samples, as shown in Fig. 5.1. These curves show a lag phase while the aggregates are nucleating, followed by a growth phase of rapid aggregation, ending in a plateau phase. We recorded timecourses for multiple crowders and analyzed the resulting aggregation parameters.

Thioflavin T is a dye that grows much brighter when bound to amyloids. Upon binding, its absorption maximum shifts from 385 nm to 450 nm and its emission maximum from 445 nm to 482 nm [145]. Although ThT is a more reliable indicator of amyloids than other fluorescence methods, notably Congo red stain, it suffers from reproducibility problems. There is no consensus on the mechanism of ThT binding to amyloids. Some proposed mechanisms rely on the presence of ThT micelles, which form above a critical concentration of about 4 μM , while others advocate for avoiding micelles [146, 147]. There is some evidence that amyloid fibrils can adsorb to the plastic surface of a multiwell plate, decreasing ThT fluorescence intensity as the fibrils mature [148]. Often in our timecourse experiments, the ThT fluorescence did reach a maximum and then decrease. The fluorescence intensity also depends on the sample viscosity, an effect which we noticed in our timecourses [149]. Despite these challenges, thioflavin T is the most consistent dye for detecting the process of amyloid formation.

5.1.1 Methods

5.1.1.1 Buffers

Potassium transport buffer (PTB) (150 mM KCl, 20 mM HEPES, 2 mM MgCl_2) was used for all timecourse and NMR samples.

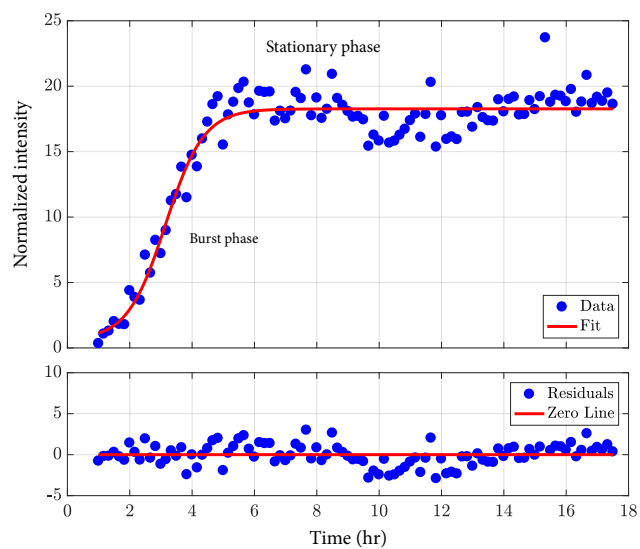


Figure 5.1: Sample sigmoid fit to FG124 sample with 13% w/v PEG. Burst phase and stationary phase are shown; lag phase took place before data collection began. Fit is to Eqn. 5.1.

5.1.1.2 FG124 preparation

His-tagged FG124 was expressed in *E. coli* in the plasmid pRSF. Cultures were grown in LB and induced at 37 degrees C for 2-4 hr with 1 mM IPTG at OD 0.6-0.8. Periplasmic matrix was removed prior to lysis. Cells were then lysed via sonication and FG124 purified using TALON cobalt resin. All purification buffers were PTB with 7M GuHCl and PIC. The elution buffer also contained 250 mM imidazole.

5.1.1.3 Timecourse preparation

Stocks of PEG and PVP in PTB were prepared at 20 or 40% w/v; serine stocks were prepared at 30% w/v. PEG and serine were at pH 7; PVP was pH 7 or pH 5. Lyophilized lysate was prepared by homogenizing BL21 DE3 Gold cells and spinning them down. The supernatant was lyophilized in a decomposing ammonium bicarbonate buffer and resuspended in PTB to the desired concentration when needed. A 10 mM stock solution of ThT in PTB was prepared and filtered no more than a week before the timecourse, stored at room temperature and protected from light. Immediately prior to starting the timecourse, FG124 was desalted into PTB to remove the imidazole and GuHCl. Samples were promptly prepared containing the appropriate percentage of crowder, a final concentration of 1-2 mg/mL FG124, and 200 uM thioflavin T. All samples in the same timecourse had the same concentration of FG124, including the buffer sample, which contained no crowding agent. Blanks were prepared with crowding agent and thioflavin T, but no FG124. Samples were pipetted into black, flat-bottomed, clear-bottomed 96-well plates with 150 uL per replicate. Each sample yielded four to six replicates. Only one blank replicate was used per condition. One negative control and corresponding blank were prepared per timecourse containing 7M GuHCl and no crowding agent but using the same protein sample as all other conditions. Each well contained a 3mm-diameter glass or teflon bead. The plate was sealed with a PCR seal and taken to a Safire II plate reader. The fluorescence was measured from the bottom at 10-minute intervals with an excitation wavelength of 450 nm, emission wavelength of 482 nm, and 5 nm bandwidths.

The plate shooook orbitally at high speed between measurements and was held at a temperature of 30 degrees C. The time between desalting and beginning the plate reader measurements was typically about an hour; the time of desalting was taken as $t = 0$ for the purposes of calculating lag time. In parallel with the sample preparation, the concentration of the desalted FG124 was measured with a BCA assay.

5.1.1.4 Timecourse analysis

After carrying out the aggregation timecourse, the data were normalized and fit to a sigmoid function in order to extract aggregation lifetimes and lag times.

The data were first normalized to the blanks, which contained crowding agents but no protein. In nearly all cases, the blank intensity remained steady over time, as expected. In those cases, the mean blank intensity was subtracted from the corresponding data. In cases where the blank intensity changed over time, it was subtracted pointwise from the data.

Then the normalized curves were fit to a sigmoid given by

$$I(t) = C + \frac{A}{1 + \exp(-k(t - T_{1/2}))} \quad (5.1)$$

where $I(t)$ is the normalized fluorescence intensity as a function of time. The aggregation dynamics are described by the rate k and the half-time $T_{1/2}$, which reflects the time needed for the intensity to reach half of its asymptotic value. More descriptive than the half-time is the lag time T_l , calculated as

$$T_l = T_{1/2} - \frac{2}{k} \quad (5.2)$$

and representing the duration of the lag phase [?]. The lag time here is defined as the intersection of the tangent line of maximum slope of the growth phase with the flat background signal of the lag phase.

The offset C and final amplitude A are less meaningful in this context, and less reliable. The offset should in principle be $C = 1$, as the fluorescence of the sample and its blank should be equal before aggregation has begun. Experimentally, $C \sim 1.2$, reaching a maximum near $C = 10$ for a

few sample conditions. While this may have been because sample aggregation had already begun, the long lag times of those conditions do not support that interpretation. It is possible that the presence of the unaggregated protein caused a change in baseline fluorescent through an unknown mechanism.

The plateau phase asymptotes to an intensity given by $I_\infty = C + A$. We found significant variation in I_∞ for the same condition between timecourses, and the relative magnitudes of different conditions also varied between timecourses. As seen in previous thioflavin T studies, higher viscosity tended to result in higher values of I_∞ . Therefore, we do not consider I_∞ in our analysis, leaving the aggregation rate k and lag time T_ℓ as parameters of interest.

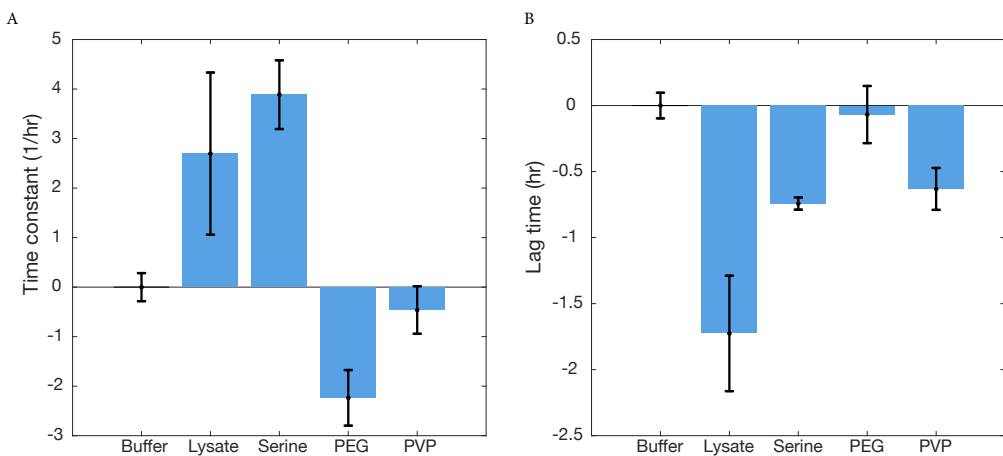
Next we normalized once again to account for differences between timecourses. It was impossible to hold the FG124 concentration exactly fixed between timecourses (lookup: make a table with Sophie's concentration info). Within each timecourse, we averaged the fit parameters for all replicates of FG124 in buffer only and subtracted that average from each replicate of each crowding condition.

5.1.2 Results

The final concentration of crowding agent was 19% serine w/v, 13% PEG, and 13% PVP. Lysate concentration varied between time courses and was in the 1-10 mg/mL range. Two timecourses were run with varying PEG and PVP concentrations: 25%, 20%, 13%, and 5%. Samples with no crowding agent ('buffer' samples) were run as a reference, and samples in 7M guanidine hydrochloride (GuHCl) with no crowding agent were run as negative controls in each timecourse. No aggregation was observed in the GuHCl samples. In every case, blanks were run alongside the sample conditions. In the blanks, the FG124 was omitted.

We then combined replicates from all timecourses by condition and took the final average and standard error of the mean for both fit parameters. The results are shown in Fig. ???. I ran a one-factor ANOVA to reject the null hypothesis that all means were the same, and then two-sample t-tests on each pair of conditions to find which differences were statistically significant. For the

Figure 5.2: (A) Aggregation lifetimes and (B) lag times for all crowding agents, normalized to the no-crowding condition. Crowder concentrations were 19% w/v serine, 13% PEG, 13% PVP, and 10 mg/mL cell lysate (lookup:check this). Error bars are standard error of the mean.



time constant, all pairs of conditions were significantly different from each other with $p < 0.05$ **except** buffer-PVP. For the lag time, all pairs of conditions were significantly different from each other with $p < 0.05$ **except** buffer-PEG and serine-PVP.

Table 5.1: Aggregation rate k p-values for all crowding agents, two-tailed t-test.

	10 mg/mL cell lysate	19% w/v serine	13% PEG	13% PVP
No crowder	0.031	1.2×10^{-6}	6.6×10^{-4}	0.41
10 mg/mL cell lysate	N/A	0.44	0.0010	0.022
19% w/v serine	N/A	N/A	4.4×10^{-9}	2.2×10^{-6}
13% PEG	N/A	N/A	N/A	0.019

Table 5.2: Lag time T_ℓ p-values for all crowding agents, two-tailed t-test.

	10 mg/mL cell lysate	19% w/v serine	13% PEG	13% PVP
No crowder	5.4×10^{-6}	1.4×10^{-8}	0.77	0.0012
10 mg/mL cell lysate	N/A	0.0051	0.00041	0.0060
19% w/v serine	N/A	N/A	0.0052	0.53
13% PEG	N/A	N/A	N/A	0.039

Table 5.3: Aggregation rate k p-values for PEG (% w/v) , two-tailed t-test.

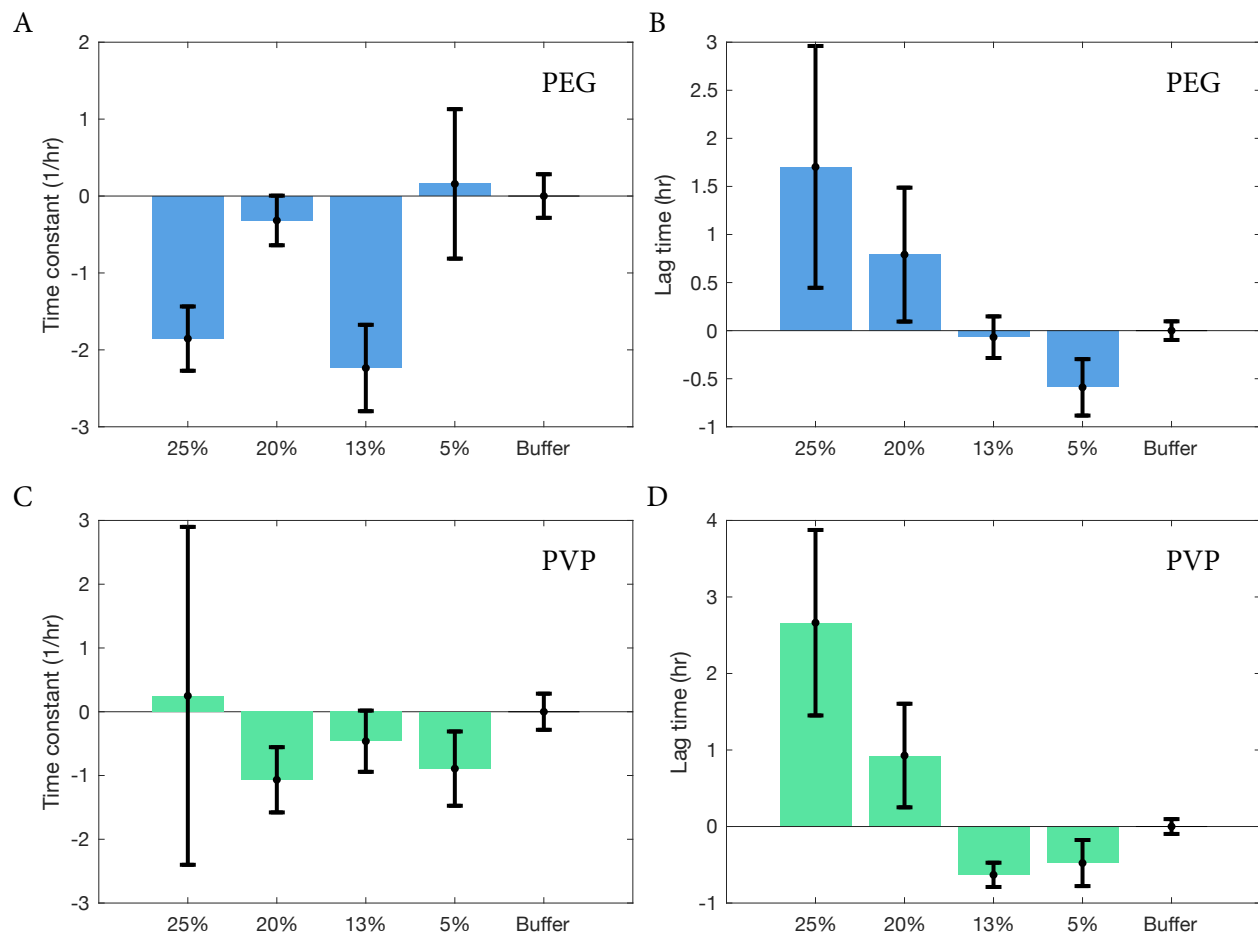
	20%	13%	5%	0%
25%	0.0063	0.6167	0.0007	0.8344
20%	N/A	0.0131	0.7539	0.0815
13%	N/A	N/A	0.1196	0.6508
5%	N/A	N/A	N/A	0.0681

Table 5.4: Lag time T_ℓ p-values for PEG (% w/v) , two-tailed t-test.

	20%	13%	5%	0%
25%	0.0071	0.0412	0.7726	0.0221
20%	N/A	0.5377	0.0206	0.1012
13%	N/A	N/A	0.1322	0.0927
5%	N/A	N/A	N/A	0.2833

Table 5.5: Aggregation rate k p-values for PVP (% w/v) , two-tailed t-test.

	20%	13%	5%	0%
25%	0.8521	0.1327	0.4104	0.1880
20%	N/A	0.6607	0.6530	0.6815
13%	N/A	N/A	0.5991	0.8283
5%	N/A	N/A	N/A	0.6902

Figure 5.3: test

I followed the same process for the timecourses involving the concentration series for PEG and PVP, but there were fewer significant differences between concentrations, as seen in Fig. 5.3. The ANOVA for the PEG time constants gave $p = 0.0024$ with the t-test showing differences between: buffer-25% PEG, buffer-13% PEG, and 25% PEG-20% PEG. The ANOVA for the PEG lag times was likewise significant with $p = 0.0102$. The significant pairs were: buffer-25% PEG, buffer-20% PEG, buffer-5% PEG, and 25% PEG-13% PEG.

For PVP, there were no significant differences in the time constant. For the lag time, after the ANOVA and t-tests, there were differences between: buffer and everything except 5% PVP, 25% PVP and everything but 20% PVP, and 20%PVP-13% PVP.

For both conditions, it looks roughly like the lag time increases with the crowder concentration, but given the large error bars, I wouldn't read too much into it. The time constants don't follow any particular trend and are mostly indistinguishable anyway.

We tested the effects of pH on FG124 aggregation by running several experiments in buffer at varying pH. We ran six replicates of each condition, for pH values between 5 and 8. No significant differences were found in the lifetimes or lag times of any pH condition. Results are summarized in Table 5.7. We concluded that aggregation is not affected by pH in the range 5-8.

Table 5.6: Lag time T_ℓ p-values for PVP (% w/v), two-tailed t-test.

	20%	13%	5%	0%
25%	4.7×10^{-5}	0.0133	0.0012	0.0628
20%	N/A	0.2586	8.6×10^{-6}	0.0272
13%	N/A	N/A	0.0018	0.0709
5%	N/A	N/A	N/A	0.6774

Table 5.7: FG124 aggregation lifetime and lag time with varying pH. Each condition run with 6 replicates in PTB buffer. One-way ANOVAs show no statistically significant differences between conditions. Standard errors are shown.

pH	Lifetime τ (hr)	Lag time T_{lag} (hr)
5	0.34 ± 0.09	6.8 ± 0.1
6	0.35 ± 0.12	6.2 ± 0.2
7	0.38 ± 0.14	6.8 ± 0.4
8	0.50 ± 0.14	6.6 ± 0.2

5.1.3 Discussion

5.2 NMR relaxation measurements

5.2.1 Methods

5.2.2 Results

5.2.3 Discussion

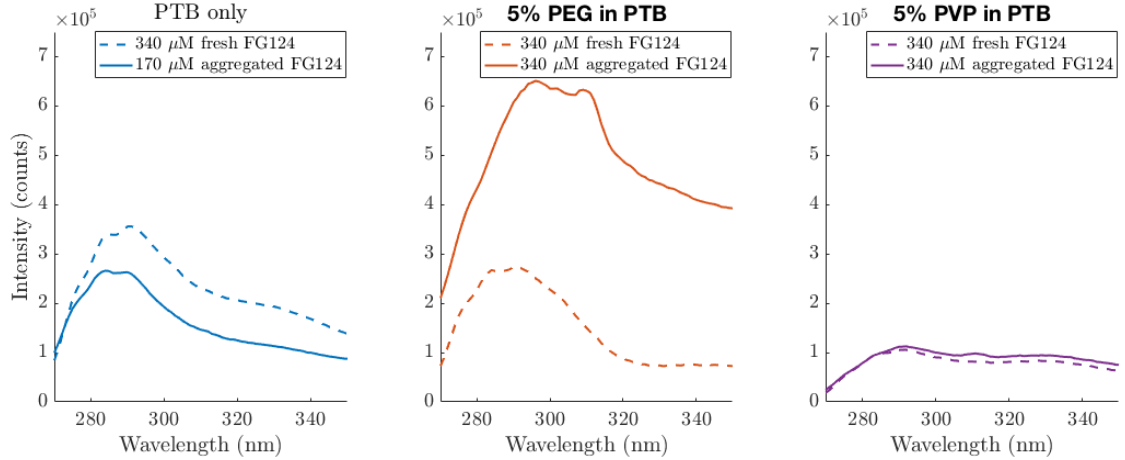
5.3 Fluorescence spectra

We hypothesized that the crowder-dependent difference in aggregation might arise from the aromatic ring in PVP, which could interact with the phenylalanine in FG124 in a ring-stacking interaction. To test this idea, I collected emission spectra of fresh and aggregated FG124 in PEG and PVP crowders near the phenylalanine peak wavelength (see Fig. 5.4).

5.3.1 Methods

FG124 was purified as described above and stored in PTB with 7M GuHCl. Immediately before use, 130 uL of 520 uM FG124 was desalted with a Zeba spin desalting column to remove the GuHCl. The resulting stock was used in the crowder samples, which had a final concentration of 340 uM Fg124. I used the shared-instrumentation fluorimeter. I tested PTB, 5% PEG (MW, source, purity?) in PTB, and 5% PVP (same questions?) in PTB as blanks. I measured 340 uM FG124 in PTB and the two crowders as well. Between runs, I cleaned the cuvette (micro quartz cuvette from Kaar lab (sample volume?)) with ethanol 3x, then 5x with DI water, and gently blotted the outside with ethanol. Fluorimeter settings: 4 nm slits, 1000 V PMT, excitation wavelength of 240 nm. Step size = 1nm, average over 2 runs. After taking this data with fresh FG124, I let the samples sit at room temp overnight to aggregate (no shaking) and most were cloudy in the morning. I took similar data with the aggregated samples. I needed to rinse with 7M GuHCl, let soak in 7M GuHCl for 5 minutes, and then perform the same cleaning procedure as the previous day in order to remove the aggregates from the cuvette.

Figure 5.4: Emission scan of fresh and aggregated FG124 in crowded conditions. Data normalized by subtracting blank sample.



5.3.2 Results

Only 5% PEG and PVP in PTB were tested because PEG has a peak near the FG124 peak which dominates at higher PEG concentrations. Data were normalized by averaging over two runs and subtracting a blank run (containing crowder and buffer but no protein). The PEG sample showed the largest difference upon aggregation, both in peak height and location. Figure 5.5 shows the same data, normalized to a maximum amplitude of one and offset, in order to emphasize the changes in peak shape. In both crowder conditions, but not in the buffer condition, a small peak appears in the aggregated FG124 near 310 nm.

Additionally, I compared the phenylalanine peaks in FSFG and fresh and aggregated FG124 to those of pure phenylalanine [149], as seen in Fig. 5.6. Data are blanked and normalized to a maximum intensity of one. The peak slightly shifts toward longer wavelengths as the data progress from phenylalanine to FSFG to fresh and aggregated FG124. I also measured PEG and PVP absorbance near 240 nm (see Fig. 5.7). PVP has a very high absorbance in that range, which might explain why the recorded counts were lowest for the PVP conditions.

Figure 5.5: Emission scan of phenylalanine, FSFG, and FG124. Excited at 240 nm. Phe data is not mine, need to check reference. Data normalized to a maximum amplitude of 1.

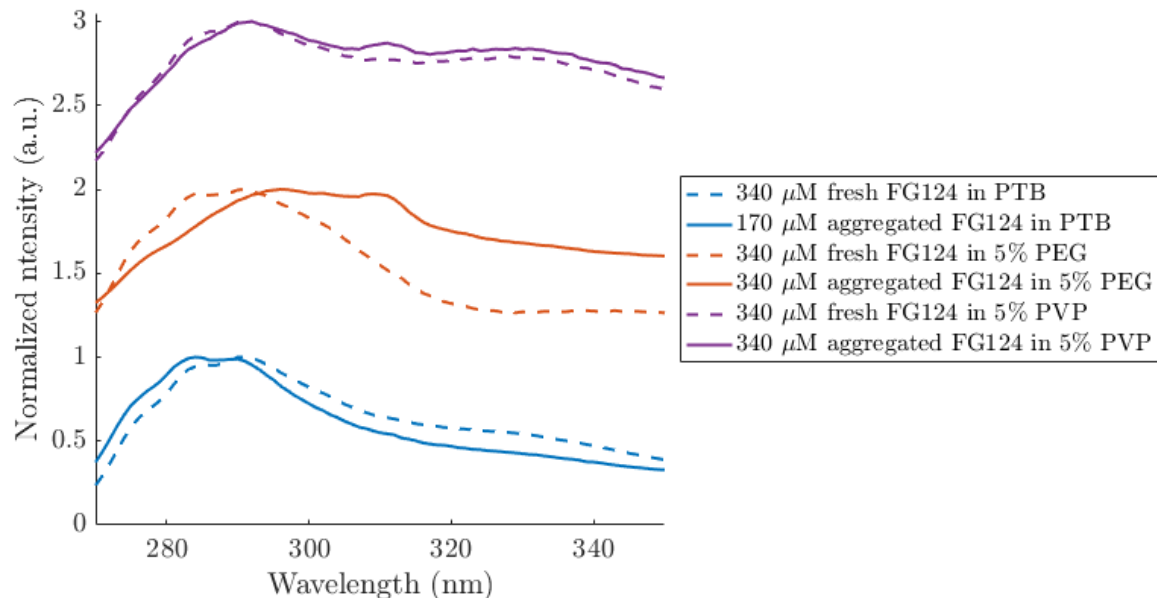


Figure 5.6: Emission scan of phenylalanine, FSFG, and FG124. Excited at 240 nm. Phe data is not mine, need to check reference. Data normalized to a maximum amplitude of 1.

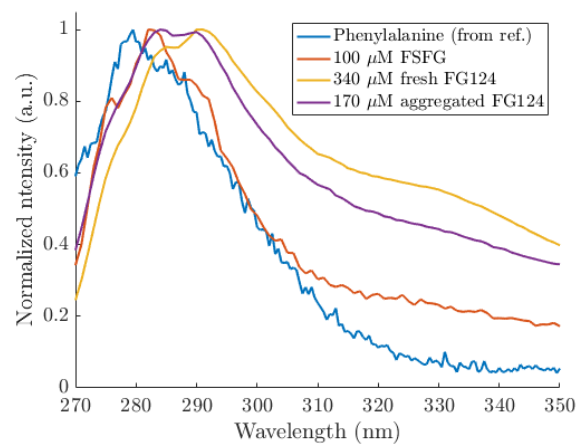
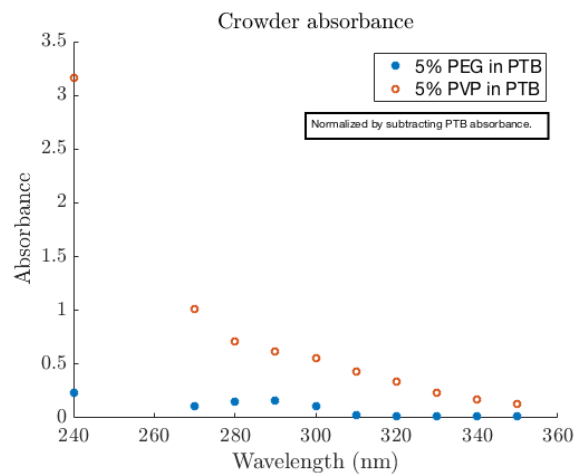


Figure 5.7: Absorbance of 5% PEG and PVP solutions in PTB. Normalized by subtracting PTB absorbance.



5.3.3 Discussion

5.4 Conclusions

It's possible that the differences in aggregation time between PEG and PVP come from changes in viscosity. The two samples do have widely different viscosity, as measured by Steve Whitten. A 13% PEG solution in PTB has a dynamic viscosity of 15.87 mPa s, while that of a 13% PVP solution in PTB is 7.34 mPa s. The literature doesn't entirely agree on what happens to aggregation as a function of viscosity, but what we see could be due to that change. (Check in lab book where I have lit search notes.)

Bibliography

- [1] B. L. Timney, B. Raveh, R. Mironksa, J. M. Trivedi, S. J. Kim, D. Russel, S. R. Wente, A. Sali, and M. P. Rout. Simple rules for passive diffusion through the nuclear pore complex. *J Cell Biol*, 215(1):57–76, October 2016.
- [2] V. N. Uversky. A decade and a half of protein intrinsic disorder: Biology still waits for physics. *Protein Science*, 22(6):693–+, June 2013. WOS:000319422500001.
- [3] P. E. Wright and H. J. Dyson. Intrinsically disordered proteins in cellular signalling and regulation. *Nature Reviews Molecular Cell Biology*, 16(1):18–29, January 2015.
- [4] I. V. Aramburu and E. A. Lemke. Floppy but not sloppy: Interaction mechanism of FG-nucleoporins and nuclear transport receptors. *Seminars in Cell & Developmental Biology*, 68:34–41, August 2017.
- [5] M. M. Babu, R. van der Lee, N. S. de Groot, and J. Gsponer. Intrinsically disordered proteins: Regulation and disease. *Current Opinion in Structural Biology*, 21(3):432–440, June 2011.
- [6] C. P. Brangwynne, P. Tompa, and R. V. Pappu. Polymer physics of intracellular phase transitions. *Nature Physics*, 11(11):899–904, November 2015.
- [7] M. Beck and E. Hurt. The nuclear pore complex: Understanding its function through structural insight. *Nature Reviews Molecular Cell Biology*, 18(2):73–89, February 2017.
- [8] S. S. Patel, B. J. Belmont, J. M. Sante, and M. F. Rexach. Natively Unfolded Nucleoporins Gate Protein Diffusion across the Nuclear Pore Complex. *Cell*, 129(1):83–96, April 2007.
- [9] C. Strambio-De-Castillia, M. Niepel, and M. P. Rout. The nuclear pore complex: Bridging nuclear transport and gene regulation. *Nature Reviews Molecular Cell Biology*, 11(7):490–501, July 2010.
- [10] L. J. Terry and S. R. Wente. Flexible Gates: Dynamic Topologies and Functions for FG-Nucleoporins in Nucleocytoplasmic Transport. *Eukaryotic Cell*, 8(12):1814–1827, December 2009.
- [11] L. E. Hough, K. Dutta, S. Sparks, D. B. Temel, A. Kamal, J. Tetenbaum-Novatt, M. P. Rout, and D. Cowburn. The molecular mechanism of nuclear transport revealed by atomic-scale measurements. *eLife*, 4:e10027, September 2015.

- [12] Y. Sakiyama, A. Mazur, L. E. Kapinos, and R. Y. H. Lim. Spatiotemporal dynamics of the nuclear pore complex transport barrier resolved by high-speed atomic force microscopy. *Nature Nanotechnology*, 11(8):719–723, August 2016.
- [13] L.-C. Tu and S. M. Musser. Single Molecule Studies of Nucleocytoplasmic Transport. *Biochimica et biophysica acta*, 1813(9):1607–1618, September 2011.
- [14] R. Moussavi-Baygi and M. R. K. Mofrad. Rapid Brownian Motion Primes Ultrafast Reconstruction of Intrinsically Disordered Phe-Gly Repeats Inside the Nuclear Pore Complex. *Scientific Reports*, 6, July 2016.
- [15] R. L. Schoch, L. E. Kapinos, and R. Y. H. Lim. Nuclear transport receptor binding avidity triggers a self-healing collapse transition in FG-nucleoporin molecular brushes. *Proceedings of the National Academy of Sciences of the United States of America*, 109(42):16911–16916, October 2012.
- [16] J. Yamada, J. L. Phillips, S. Patel, G. Goldfien, A. Calestagne-Morelli, H. Huang, R. Reza, J. Acheson, V. V. Krishnan, S. Newsam, A. Gopinathan, E. Y. Lau, M. E. Colvin, V. N. Uversky, and M. F. Rexach. A bimodal distribution of two distinct categories of intrinsically disordered structures with separate functions in FG nucleoporins. *Molecular & cellular proteomics: MCP*, 9(10):2205–2224, October 2010.
- [17] D. Ando, R. Zandi, Y. W. Kim, M. Colvin, M. Rexach, and A. Gopinathan. Nuclear Pore Complex Protein Sequences Determine Overall Copolymer Brush Structure and Function. *Biophysical Journal*, 106(9):1997–2007, May 2014.
- [18] M. Tagliazucchi, O. Peleg, M. Kroeger, Y. Rabin, and I. Szleifer. Effect of charge, hydrophobicity, and sequence of nucleoporins on the translocation of model particles through the nuclear pore complex. *Proceedings of the National Academy of Sciences of the United States of America*, 110(9):3363–3368, February 2013. WOS:000315841900039.
- [19] B. Zeitler and K. Weis. The FG-repeat asymmetry of the nuclear pore complex is dispensable for bulk nucleocytoplasmic transport *in vivo*. *The Journal of Cell Biology*, 167(4):583–590, November 2004.
- [20] L. A. Strawn, T. Shen, N. Shulga, D. S. Goldfarb, and S. R. Wente. Minimal nuclear pore complexes define FG repeat domains essential for transport. *Nature Cell Biology*, 6(3):197–206, March 2004.
- [21] S. W. Kowalczyk, L. Kapinos, T. R. Blosser, T. Magalhães, P. van Nies, R. Y. H. Lim, and C. Dekker. Single-molecule transport across an individual biomimetic nuclear pore complex. *Nature Nanotechnology*, 6(7):433–438, July 2011.
- [22] T. Jovanovic-Talisman, J. Tetenbaum-Novatt, A. S. McKenney, A. Zilman, R. Peters, M. P. Rout, and B. T. Chait. Artificial nanopores that mimic the transport selectivity of the nuclear pore complex. *Nature*, 457(7232):1023–1027, February 2009.
- [23] B. Pyhtila and M. Rexach. A Gradient of Affinity for the Karyopherin Kap95p along the Yeast Nuclear Pore Complex. *Journal of Biological Chemistry*, 278(43):42699–42709, October 2003.

- [24] D. Gilchrist, B. Mykytka, and M. Rexach. Accelerating the Rate of Disassembly of Karyopherin-Cargo Complexes. *Journal of Biological Chemistry*, 277(20):18161–18172, May 2002.
- [25] J. Tetenbaum-Novatt, L. E. Hough, R. Mironcka, A. S. McKenney, and M. P. Rout. Nucleocytoplasmic Transport: A Role for Nonspecific Competition in Karyopherin-Nucleoporin Interactions. *Molecular & Cellular Proteomics : MCP*, 11(5):31–46, May 2012.
- [26] S. Milles, D. Mercadante, I. V. Aramburu, M. R. Jensen, N. Banterle, C. Koehler, S. Tyagi, J. Clarke, S. L. Shammas, M. Blackledge, F. Gräter, and E. A. Lemke. Plasticity of an Ultrafast Interaction between Nucleoporins and Nuclear Transport Receptors. *Cell*, 163(3):734–745, October 2015.
- [27] R. Hayama, S. Sparks, L. M. Hecht, K. Dutta, J. M. Karp, C. M. Cabana, M. P. Rout, and D. Cowburn. Thermodynamic characterization of the multivalent interactions underlying rapid and selective translocation through the nuclear pore complex. *Journal of Biological Chemistry*, 293(12):4555–4563, March 2018.
- [28] T. Jovanovic-Talisman and A. Zilman. Protein Transport by the Nuclear Pore Complex: Simple Biophysics of a Complex Biomachine. *Biophysical Journal*, 113(1):6–14, July 2017.
- [29] L. E. Kapinos, B. Huang, C. Rencurel, and R. Y. H. Lim. Karyopherins regulate nuclear pore complex barrier and transport function. *J Cell Biol*, page jcb.201702092, September 2017.
- [30] S. H. Yoshimura and T. Hirano. HEAT repeats – versatile arrays of amphiphilic helices working in crowded environments? *J Cell Sci*, 129(21):3963–3970, November 2016.
- [31] Y. M. Chook and K. E. Süel. Nuclear import by karyopherin-*Bs*: Recognition and inhibition. *Biochimica et Biophysica Acta (BBA) - Molecular Cell Research*, 1813(9):1593–1606, September 2011.
- [32] L. E. Kapinos, R. L. Schoch, R. S. Wagner, K. D. Schleicher, and R. Y. H. Lim. Karyopherin-Centric Control of Nuclear Pores Based on Molecular Occupancy and Kinetic Analysis of Multivalent Binding with FG Nucleoporins. *Biophysical Journal*, 115(12):2512, December 2018.
- [33] K. D. Schleicher, S. L. Dettmer, L. E. Kapinos, S. Pagliara, U. F. Keyser, S. Jeney, and R. Y. H. Lim. Selective transport control on molecular velcro made from intrinsically disordered proteins. *Nature Nanotechnology*, 9(7):525–530, July 2014.
- [34] L. E. Kapinos, R. L. Schoch, R. S. Wagner, K. D. Schleicher, and R. Y. Lim. Karyopherin-Centric Control of Nuclear Pores Based on Molecular Occupancy and Kinetic Analysis of Multivalent Binding with FG Nucleoporins. *Biophysical Journal*, 106(8):1751–1762, April 2014.
- [35] D. Görlich, N. Panté, U. Kutay, U. Aebi, and F. R. Bischoff. Identification of different roles for RanGDP and RanGTP in nuclear protein import. *The EMBO Journal*, 15(20):5584–5594, October 1996.
- [36] M. Stewart. Molecular mechanism of the nuclear protein import cycle. *Nature Reviews. Molecular Cell Biology*, 8(3):195–208, March 2007.

- [37] K. Ribbeck, G. Lipowsky, H. M. Kent, M. Stewart, and D. Görlich. NTF2 mediates nuclear import of Ran. *The EMBO Journal*, 17(22):6587–6598, November 1998.
- [38] R. Bayliss, K. Ribbeck, D. Akin, H. M. Kent, C. M. Feldherr, D. Görlich, and M. Stewart. Interaction between NTF2 and xFxFG-containing nucleoporins is required to mediate nuclear import of RanGDP 1. *Journal of Molecular Biology*, 293(3):579–593, October 1999.
- [39] K. Ribbeck and D. Görlich. Kinetic analysis of translocation through nuclear pore complexes. *The EMBO Journal*, 20(6):1320–1330, March 2001.
- [40] J. P. Siebrasse and R. Peters. Rapid translocation of NTF2 through the nuclear pore of isolated nuclei and nuclear envelopes. *EMBO Reports*, 3(9):887–892, September 2002.
- [41] N. I. Kiskin, J. P. Siebrasse, and R. Peters. Optical Micowell Assay of Membrane Transport Kinetics. *Biophysical Journal*, 85(4):2311–2322, October 2003.
- [42] G. J. Stanley, A. Fassati, and B. W. Hoogenboom. Biomechanics of the transport barrier in the nuclear pore complex. *Seminars in Cell & Developmental Biology*, 68:42–51, August 2017.
- [43] A. Paradise, M. K. Levin, G. Korza, and J. H. Carson. Significant proportions of nuclear transport proteins with reduced intracellular mobilities resolved by fluorescence correlation spectroscopy. *Journal of molecular biology*, 365(1):50–65, January 2007.
- [44] W. Yang and S. M. Musser. Nuclear import time and transport efficiency depend on importin β concentration. *The Journal of Cell Biology*, 174(7):951–961, September 2006.
- [45] T. Dange, D. Grünwald, A. Grünwald, R. Peters, and U. Kubitscheck. Autonomy and robustness of translocation through the nuclear pore complex: A single-molecule study. *The Journal of Cell Biology*, 183(1):77–86, 2008.
- [46] U. Kubitscheck, D. Grünwald, A. Hoekstra, D. Rohleder, T. Kues, J. P. Siebrasse, and R. Peters. Nuclear transport of single molecules. *The Journal of Cell Biology*, 168(2):233–243, January 2005.
- [47] M. Elbaum. Polymers in the Pore. *Science*, 314(5800):766–767, November 2006.
- [48] S. Frey, R. P. Richter, and D. Görlich. FG-Rich Repeats of Nuclear Pore Proteins Form a Three-Dimensional Meshwork with Hydrogel-Like Properties. *Science*, 314(5800):815–817, November 2006.
- [49] S. Frey and D. Görlich. A Saturated FG-Repeat Hydrogel Can Reproduce the Permeability Properties of Nuclear Pore Complexes. *Cell*, 130(3):512–523, August 2007.
- [50] C. Ader, S. Frey, W. Maas, H. B. Schmidt, D. Görlich, and M. Baldus. Amyloid-like interactions within nucleoporin FG hydrogels. *Proceedings of the National Academy of Sciences*, 107(14):6281–6285, June 2010.
- [51] M. Kim, W. G. Chen, J. W. Kang, M. J. Glassman, K. Ribbeck, and B. D. Olsen. Artificially Engineered Protein Hydrogels Adapted from the Nucleoporin Nsp1 for Selective Biomolecular Transport. *Advanced materials (Deerfield Beach, Fla.)*, 27(28):4207–4212, July 2015.

- [52] T. Bickel and R. Bruinsma. The Nuclear Pore Complex Mystery and Anomalous Diffusion in Reversible Gels. *Biophysical Journal*, 83(6):3079–3087, December 2002.
- [53] C. Gu, A. Vovk, T. Zheng, R. D. Coalson, and A. Zilman. The Role of Cohesiveness in the Permeability of the Spatial Assemblies of FG Nucleoporins. *Biophysical Journal*, 116(7):1204–1215, April 2019.
- [54] M. P. Rout, J. D. Aitchison, A. Suprapto, K. Hjertaas, Y. Zhao, and B. T. Chait. The Yeast Nuclear Pore Complex Composition, Architecture, and Transport Mechanism. *The Journal of Cell Biology*, 148(4):635–652, February 2000.
- [55] R. Y. H. Lim, U. Aebi, and B. Fahrenkrog. Towards reconciling structure and function in the nuclear pore complex. *Histochemistry and Cell Biology*, 129(2):105–116, February 2008.
- [56] R. S. Wagner, L. E. Kapinos, N. J. Marshall, M. Stewart, and R. Y. H. Lim. Promiscuous Binding of Karyopherin β 1 Modulates FG Nucleoporin Barrier Function and Expedites NTF2 Transport Kinetics. *Biophysical Journal*, 108(4):918–927, February 2015.
- [57] R. Zahn, D. Osmanović, S. Ehret, C. A. Callis, S. Frey, M. Stewart, C. You, D. Görlich, B. W. Hoogenboom, and R. P. Richter. A physical model describing the interaction of nuclear transport receptors with FG nucleoporin domain assemblies. *eLife*, 5:e14119, April 2016.
- [58] A. Vovk, C. Gu, M. G. Opferman, L. E. Kapinos, R. Y. Lim, R. D. Coalson, D. Jasnow, and A. Zilman. Simple biophysics underpins collective conformations of the intrinsically disordered proteins of the Nuclear Pore Complex. *eLife*, 5:e10785, May 2016.
- [59] A. E. Nasrabad, D. Jasnow, A. Zilman, and R. D. Coalson. Precise control of polymer coated nanopores by nanoparticle additives: Insights from computational modeling. *Journal of Chemical Physics*, 145(6):064901, August 2016. WOS:000381680300043.
- [60] J. S. Mincer and S. M. Simon. Simulations of nuclear pore transport yield mechanistic insights and quantitative predictions. *Proceedings of the National Academy of Sciences of the United States of America*, 108(31):E351–358, August 2011.
- [61] A. Zilman, S. D. Talia, B. T. Chait, M. P. Rout, and M. O. Magnasco. Efficiency, Selectivity, and Robustness of Nucleocytoplasmic Transport. *PLOS Computational Biology*, 3(7):e125, July 2007.
- [62] L.-C. Tu, G. Fu, A. Zilman, and S. M. Musser. Large cargo transport by nuclear pores: Implications for the spatial organization of FG-nucleoporins. *The EMBO journal*, 32(24):3220–3230, December 2013.
- [63] J. Tetenbaum-Novatt, L. E. Hough, R. Mironská, A. S. McKenney, and M. P. Rout. Nucleocytoplasmic Transport: A Role for Nonspecific Competition in Karyopherin-Nucleoporin Interactions. *Molecular & Cellular Proteomics : MCP*, 11(5):31–46, May 2012.
- [64] A. Zilman. Effects of Multiple Occupancy and Interparticle Interactions on Selective Transport through Narrow Channels: Theory versus Experiment. *Biophysical Journal*, 96(4):1235–1248, February 2009.

- [65] A. Zilman, S. D. Talia, T. Jovanovic-Talismann, B. T. Chait, M. P. Rout, and M. O. Magnasco. Enhancement of Transport Selectivity through Nano-Channels by Non-Specific Competition. *PLOS Computational Biology*, 6(6):e1000804, June 2010.
- [66] B. L. Timney, J. Tetenbaum-Novatt, D. S. Agate, R. Williams, W. Zhang, B. T. Chait, and M. P. Rout. Simple kinetic relationships and nonspecific competition govern nuclear import rates in vivo. *J Cell Biol*, 175(4):579–593, November 2006.
- [67] Y. J. Yang, D. J. Mai, T. J. Dursch, and B. D. Olsen. Nucleopore-Inspired Polymer Hydrogels for Selective Biomolecular Transport. *Biomacromolecules*, September 2018.
- [68] A. N. Ananth, A. Mishra, S. Frey, A. Dwarkasing, R. Versloot, E. van der Giessen, D. Görlich, P. Onck, and C. Dekker. Spatial structure of disordered proteins dictates conductance and selectivity in nuclear pore complex mimics. *eLife*, 7:e31510, February 2018.
- [69] A. K. Friedman and L. A. Baker. Synthetic hydrogel mimics of the nuclear pore complex display selectivity dependent on FG-repeat concentration and electrostatics. *Soft Matter*, 12(47):9477–9484, November 2016.
- [70] P. D. E. Fisher, Q. Shen, B. Akpinar, L. K. Davis, K. K. H. Chung, D. Baddeley, A. Saric, T. J. Melia, B. W. Hoogenboom, C. Lin, and C. P. Lusk. A Programmable DNA Origami Platform for Organizing Intrinsically Disordered Nucleoporins within Nanopore Confinement. *ACS nano*, January 2018.
- [71] T. Carlson, J. Lock, and R. Carrier. Engineering the Mucus Barrier. *Annual Review of Biomedical Engineering*, 20(1):197–220, 2018.
- [72] A. F. L. Schneider and C. P. R. Hackenberger. Fluorescent labelling in living cells. *Current Opinion in Biotechnology*, 48:61–68, December 2017.
- [73] J. Witten and K. Ribbeck. The particle in the spider’s web: Transport through biological hydrogels. *Nanoscale*, May 2017.
- [74] S. K. Lai, Y.-Y. Wang, K. Hida, R. Cone, and J. Hanes. Nanoparticles reveal that human cervicovaginal mucus is riddled with pores larger than viruses. *Proceedings of the National Academy of Sciences*, 107(2):598–603, January 2010.
- [75] S. K. Lai, J. S. Suk, A. Pace, Y.-Y. Wang, M. Yang, O. Mert, J. Chen, J. Kim, and J. Hanes. Drug carrier nanoparticles that penetrate human chronic rhinosinusitis mucus. *Biomaterials*, 32(26):6285–6290, September 2011.
- [76] N. A. Peppas and P. A. Buri. Surface, interfacial and molecular aspects of polymer bioadhesion on soft tissues. *Journal of Controlled Release*, 2:257–275, November 1985.
- [77] J. C. Lay, M. R. Stang, P. E. Fisher, J. R. Yankaskas, and W. D. Bennett. Airway retention of materials of different solubility following local intrabronchial deposition in dogs. *Journal of Aerosol Medicine: The Official Journal of the International Society for Aerosols in Medicine*, 16(2):153–166, 2003.
- [78] A. Popov, L. Schopf, J. Bourassa, and H. Chen. Enhanced pulmonary delivery of fluticasone propionate in rodents by mucus-penetrating nanoparticles. *International Journal of Pharmaceutics*, 502(1):188–197, April 2016.

- [79] X. Huang, J. Chisholm, J. Zhuang, Y. Xiao, G. Duncan, X. Chen, J. S. Suk, and J. Hanes. Protein nanocages that penetrate airway mucus and tumor tissue. *Proceedings of the National Academy of Sciences*, 114(32):E6595–E6602, August 2017.
- [80] P. Mastorakos, A. L. da Silva, J. Chisholm, E. Song, W. K. Choi, M. P. Boyle, M. M. Morales, J. Hanes, and J. S. Suk. Highly compacted biodegradable DNA nanoparticles capable of overcoming the mucus barrier for inhaled lung gene therapy. *Proceedings of the National Academy of Sciences*, 112(28):8720–8725, July 2015.
- [81] B. Porsio, E. F. Craparo, N. Mauro, G. Giannona, and G. Cavallaro. Mucus and Cell-Penetrating Nanoparticles Embedded in Nano-into-Micro Formulations for Pulmonary Delivery of Ivacaftor in Patients with Cystic Fibrosis. *ACS Applied Materials & Interfaces*, 10(1):165–181, January 2018.
- [82] B. C. Tang, M. Dawson, S. K. Lai, Y.-Y. Wang, J. S. Suk, M. Yang, P. Zeitlin, M. P. Boyle, J. Fu, and J. Hanes. Biodegradable polymer nanoparticles that rapidly penetrate the human mucus barrier. *Proceedings of the National Academy of Sciences of the United States of America*, 106(46):19268–19273, November 2009.
- [83] L. Mirny, M. Slutsky, Z. Wunderlich, A. Tafvizi, J. Leith, and A. Kosmrlj. How a protein searches for its site on DNA: The mechanism of facilitated diffusion. *Journal of Physics A: Mathematical and Theoretical*, 42(43):434013, October 2009.
- [84] S. E. Halford. An end to 40 years of mistakes in DNA–protein association kinetics? *Biochemical Society Transactions*, 37(2):343–348, April 2009.
- [85] B. Raveh, J. M. Karp, S. Sparks, K. Dutta, M. P. Rout, A. Sali, and D. Cowburn. Slide-and-exchange mechanism for rapid and selective transport through the nuclear pore complex. *Proceedings of the National Academy of Sciences*, 113(18):E2489–E2497, May 2016.
- [86] M. Doucette and G. M. Clore. Global jumping and domain-specific intersegment transfer between DNA cognate sites of the multidomain transcription factor Oct-1. *Proceedings of the National Academy of Sciences*, 105(37):13871–13876, September 2008.
- [87] S. E. Halford, A. J. Welsh, and M. D. Szczelkun. Enzyme-mediated DNA looping. *Annual Review of Biophysics and Biomolecular Structure*, 33:1–24, 2004.
- [88] J. Iwahara and Y. Levy. Speed-stability paradox in DNA-scanning by zinc-finger proteins. *Transcription*, 4(2):58–61, March 2013.
- [89] L. Zandarashvili, A. Esadze, D. Vuzman, C. A. Kemme, Y. Levy, and J. Iwahara. Balancing between affinity and speed in target DNA search by zinc-finger proteins via modulation of dynamic conformational ensemble. *Proceedings of the National Academy of Sciences*, 112(37):E5142–E5149, September 2015.
- [90] M. V. Sukhanova, S. Abrakhi, V. Joshi, D. Pastre, M. M. Kutuzov, R. O. Anarbaev, P. A. Curmi, L. Hamon, and O. I. Lavrik. Single molecule detection of PARP1 and PARP2 interaction with DNA strand breaks and their poly(ADP-ribosyl)ation using high-resolution AFM imaging. *Nucleic Acids Research*, 44(6):e60–e60, April 2016.
- [91] J. Rudolph, J. Mahadevan, P. Dyer, and K. Luger. Poly(ADP-ribose) polymerase 1 searches DNA via a ‘monkey bar’ mechanism. *eLife*, 7:e37818, August 2018.

- [92] J. Mahadevan, J. Rudolph, A. Jha, J. W. Tay, J. Dragavon, E. M. Grumstrup, and K. Luger. Q-FADD: A mechanistic approach for modeling the accumulation of proteins at sites of DNA damage by free diffusion. *bioRxiv*, page 373043, July 2018.
- [93] M. Feric, N. Vaidya, T. S. Harmon, D. M. Mitrea, L. Zhu, T. M. Richardson, R. W. Krizacki, R. V. Pappu, and C. P. Brangwynne. Coexisting Liquid Phases Underlie Nucleolar Subcompartments. *Cell*, 165(7):1686–1697, June 2016.
- [94] N. Shiina. Liquid- and solid-like RNA granules form through specific scaffold proteins and combine into biphasic granules. *Journal of Biological Chemistry*, 294(10):3532–3548, August 2019.
- [95] A. E. Posey, A. S. Holehouse, and R. V. Pappu. Chapter One - Phase Separation of Intrinsically Disordered Proteins. In E. Rhoades, editor, *Methods in Enzymology*, volume 611 of *Intrinsically Disordered Proteins*, pages 1–30. Academic Press, January 2018.
- [96] A. Catalano and D. H. O’Day. Evidence for nucleolar subcompartments in Dictyostelium. *Biochemical and Biophysical Research Communications*, 456(4):901–907, January 2015.
- [97] D. H. O’Day. Proteins of the Nucleolus of Dictyostelium discoideum: Nucleolar Compartmentalization, Targeting Sequences, Protein Translocations and Binding Partners. *Cells*, 8(2):167, February 2019.
- [98] S. Jain, J. R. Wheeler, R. W. Walters, A. Agrawal, A. Barsic, and R. Parker. ATPase-Modulated Stress Granules Contain a Diverse Proteome and Substructure. *Cell*, 164(3):487–498, January 2016.
- [99] L. Ristroph, A. J. Bergou, G. J. Berman, J. Guckenheimer, Z. J. Wang, and I. Cohen. Dynamics, Control, and Stabilization of Turning Flight in Fruit Flies. In S. Childress, A. Hosoi, W. W. Schultz, and J. Wang, editors, *Natural Locomotion in Fluids and on Surfaces*, The IMA Volumes in Mathematics and Its Applications, pages 83–99. Springer New York, 2012.
- [100] A. C. Noel and D. L. Hu. Cats use hollow papillae to wick saliva into fur. *Proceedings of the National Academy of Sciences*, 115(49):12377–12382, December 2018.
- [101] S. J. Gerbode, J. R. Puzyk, A. G. McCormick, and L. Mahadevan. How the Cucumber Tendril Coils and Overwinds. *Science*, 337(6098):1087–1091, August 2012.
- [102] J. Pulupa, M. Rachh, M. D. Tomasini, J. S. Mincer, and S. M. Simon. A coarse-grained computational model of the nuclear pore complex predicts Phe-Gly nucleoporin dynamics. *The Journal of General Physiology*, page jgp.201711769, September 2017.
- [103] S. Pagliara, S. L. Dettmer, and U. F. Keyser. Channel-facilitated diffusion boosted by particle binding at the channel entrance. *Physical Review Letters*, 113(4):048102, July 2014.
- [104] A. R. Lowe, J. H. Tang, J. Yassif, M. Graf, W. Y. Huang, J. T. Groves, K. Weis, and J. T. Liphardt. Importin- β modulates the permeability of the nuclear pore complex in a Ran-dependent manner. *eLife*, 4:e04052, March 2015.

- [105] W. Yang, J. Gelles, and S. M. Musser. Imaging of single-molecule translocation through nuclear pore complexes. *Proceedings of the National Academy of Sciences of the United States of America*, 101(35):12887–12892, August 2004.
- [106] M. Stefferson. Dynamics of Crowded and Active Biological Systems. *Physics Graduate Theses & Dissertations*, January 2018.
- [107] H. B. Schmidt and D. Görlich. Nup98 FG domains from diverse species spontaneously phase-separate into particles with nuclear pore-like permselectivity. *eLife*, 4:e04251, January 2015.
- [108] D. Frenkel-Krispin, B. Maco, U. Aebi, and O. Medalia. Structural Analysis of a Metazoan Nuclear Pore Complex Reveals a Fused Concentric Ring Architecture. *Journal of Molecular Biology*, 395(3):578–586, January 2010.
- [109] T. Maimon, N. Elad, I. Dahan, and O. Medalia. The Human Nuclear Pore Complex as Revealed by Cryo-Electron Tomography. *Structure*, 20(6):998–1006, June 2012.
- [110] F. Cardarelli and E. Gratton. In Vivo Imaging of Single-Molecule Translocation Through Nuclear Pore Complexes by Pair Correlation Functions. *PLOS ONE*, 5(5):e10475, May 2010.
- [111] S. Frey and D. Görlich. FG/FxFG as well as GLFG repeats form a selective permeability barrier with self-healing properties. *The EMBO Journal*, 28(17):2554–2567, 2009.
- [112] R. Y. H. Lim, B. Fahrenkrog, J. Köser, K. Schwarz-Herion, J. Deng, and U. Aebi. Nanomechanical Basis of Selective Gating by the Nuclear Pore Complex. *Science*, 318(5850):640–643, October 2007.
- [113] S. Milles and E. A. Lemke. Mapping Multivalency and Differential Affinities within Large Intrinsically Disordered Protein Complexes with Segmental Motion Analysis. *Angewandte Chemie International Edition*, 53(28):7364–7367, July 2014.
- [114] J. Howard. *Mechanics of Motor Proteins and Cytoskeleton*. Sinauer Associates, 1st edition, 2001.
- [115] M. Doi and S. F. Edwards. *The Theory of Polymer Dynamics*. Clarendon Press, 1988. Google-Books-ID: dMzGyWs3GKcC.
- [116] V. Receveur-Bréchot and D. Durand. How Random are Intrinsically Disordered Proteins? A Small Angle Scattering Perspective. *Current Protein & Peptide Science*, 13(1):55–75, February 2012.
- [117] R. Blackwell, C. Edelmaier, O. Sweezy-Schindler, A. Lamson, Z. R. Gergely, E. O’Toole, A. Crapo, L. E. Hough, J. R. McIntosh, M. A. Glaser, and M. D. Betterton. Physical determinants of bipolar mitotic spindle assembly and stability in fission yeast. *Science Advances*, 3(1):e1601603, January 2017.
- [118] W. A. McGuinness, N. Malachowa, and F. R. DeLeo. Vancomycin Resistance in *Staphylococcus aureus*. *The Yale Journal of Biology and Medicine*, 90(2):269–281, June 2017.
- [119] M. Kruithof, F.-T. Chien, A. Routh, C. Logie, D. Rhodes, and J. van Noort. Single-molecule force spectroscopy reveals a highly compliant helical folding for the 30-nm chromatin fiber. *Nature Structural & Molecular Biology*, 16(5):534–540, May 2009.

- [120] D. Norouzi and V. B. Zhurkin. Dynamics of Chromatin Fibers: Comparison of Monte Carlo Simulations with Force Spectroscopy. *Biophysical Journal*, 115(9):1644–1655, November 2018.
- [121] N. Høiby, T. Bjarnsholt, M. Givskov, S. Molin, and O. Ciofu. Antibiotic resistance of bacterial biofilms. *International Journal of Antimicrobial Agents*, 35(4):322–332, April 2010.
- [122] Y. Zhou and J. Kopeček. Biological rationale for the design of polymeric anti-cancer nanomedicines. *Journal of Drug Targeting*, 21(1):1–26, January 2013.
- [123] S. Chatani, T. Gong, B. A. Earle, M. Podgórski, and C. N. Bowman. Visible-Light Initiated Thiol-Michael Addition Photopolymerization Reactions. *ACS Macro Letters*, 3(4):315–318, April 2014.
- [124] D. P. Nair, M. Podgórski, S. Chatani, T. Gong, W. Xi, C. R. Fenoli, and C. N. Bowman. The Thiol-Michael Addition Click Reaction: A Powerful and Widely Used Tool in Materials Chemistry. *Chemistry of Materials*, 26(1):724–744, January 2014.
- [125] B. D. Fairbanks, M. P. Schwartz, C. N. Bowman, and K. S. Anseth. Photoinitiated polymerization of PEG-diacrylate with lithium phenyl-2,4,6-trimethylbenzoylphosphinate: Polymerization rate and cytocompatibility. *Biomaterials*, 30(35):6702–6707, December 2009.
- [126] D. Bartolo, G. Degré, P. Nghe, and V. Studer. Microfluidic stickers. *Lab on a Chip*, 8(2):274–279, January 2008.
- [127] J. S. Paustian, R. N. Azevedo, S.-T. B. Lundin, M. J. Gilkey, and T. M. Squires. Microfluidic Microdialysis: Spatiotemporal Control over Solution Microenvironments Using Integrated Hydrogel Membrane Microwindows. *Physical Review X*, 3(4), November 2013.
- [128] J. Yin, P. D. Straight, S. M. McLoughlin, Z. Zhou, A. J. Lin, D. E. Golan, N. L. Kelleher, R. Kolter, and C. T. Walsh. Genetically encoded short peptide tag for versatile protein labeling by Sfp phosphopantetheinyl transferase. *Proceedings of the National Academy of Sciences*, 102(44):15815–15820, November 2005.
- [129] C. Chaillan-Huntington, P. J. G. Butler, J. A. Huntington, D. Akin, C. Feldherr, and M. Stewart. NTF2 monomer-dimer equilibrium1. *Journal of Molecular Biology*, 314(3):465–477, November 2001.
- [130] N. Annabi, J. W. Nichol, X. Zhong, C. Ji, S. Koshy, A. Khademhosseini, and F. Dehghani. Controlling the porosity and microarchitecture of hydrogels for tissue engineering. *Tissue Engineering Part B: Reviews*, 16(4):371–383, 2010.
- [131] T. Brunette, F. Parmeggiani, P.-S. Huang, G. Bhabha, D. C. Ekiert, S. E. Tsutakawa, G. L. Hura, J. A. Tainer, and D. Baker. Exploring the repeat protein universe through computational protein design. *Nature*, 528(7583):580–584, December 2015.
- [132] P.-S. Huang, G. Oberdorfer, C. Xu, X. Y. Pei, B. L. Nannenga, J. M. Rogers, F. DiMaio, T. Gonen, B. Luisi, and D. Baker. High thermodynamic stability of parametrically designed helical bundles. *Science*, 346(6208):481–485, October 2014.
- [133] M. Bruchet and A. Melman. Fabrication of patterned calcium cross-linked alginate hydrogel films and coatings through reductive cation exchange. *Carbohydrate Polymers*, 131:57–64, October 2015.

- [134] S. De and D. Robinson. Polymer relationships during preparation of chitosan–alginate and poly-l-lysine–alginate nanospheres. *Journal of Controlled Release*, 89(1):101–112, April 2003.
- [135] M. A. Masuelli. Dextrans in Aqueous Solution. Experimental Review on Intrinsic Viscosity Measurements and Temperature Effect. *Journal of Polymer and Biopolymer Physics Chemistry*, 1(1):13–21, January 2013.
- [136] B. L. Sprague, R. L. Pego, D. A. Stavreva, and J. G. McNally. Analysis of Binding Reactions by Fluorescence Recovery after Photobleaching. *Biophysical Journal*, 86(6):3473–3495, June 2004.
- [137] J. Wu, N. Shekhar, P. P. Lele, and T. P. Lele. FRAP Analysis: Accounting for Bleaching during Image Capture. *PLOS ONE*, 7(8):e42854, August 2012.
- [138] M. Kang, C. A. Day, E. DiBenedetto, and A. K. Kenworthy. A Quantitative Approach to Analyze Binding Diffusion Kinetics by Confocal FRAP. *Biophysical Journal*, 99(9):2737–2747, November 2010.
- [139] M. Kang, C. A. Day, A. K. Kenworthy, and E. DiBenedetto. Simplified equation to extract diffusion coefficients from confocal FRAP data. *Traffic (Copenhagen, Denmark)*, 13(12):1589–1600, December 2012.
- [140] N. A. Mortensen, F. Okkels, and H. Bruus. Universality in edge-source diffusion dynamics. *Physical Review E*, 73(1), January 2006.
- [141] H.S. Carslaw and J.C. Jaeger. *Conduction of Heat in Solids*. Clarendon Press, Oxford, 2 edition, 1959.
- [142] S. Piccolo, S. Dupont, and M. Cordenonsi. The Biology of YAP/TAZ: Hippo Signaling and Beyond. *Physiological Reviews*, 94(4):1287–1312, October 2014.
- [143] S. S. Olmsted, J. L. Padgett, A. I. Yudin, K. J. Whaley, T. R. Moench, and R. A. Cone. Diffusion of Macromolecules and Virus-Like Particles in Human Cervical Mucus. *Biophysical Journal*, 81(4):1930–1937, October 2001.
- [144] S. K. Lai, K. Hida, S. Shukair, Y.-Y. Wang, A. Figueiredo, R. Cone, T. J. Hope, and J. Hanes. Human Immunodeficiency Virus Type 1 Is Trapped by Acidic but Not by Neutralized Human Cervicovaginal Mucus. *Journal of Virology*, 83(21):11196–11200, November 2009.
- [145] M. M. Picken and G. A. Herrera. Thioflavin T Stain: An Easier and More Sensitive Method for Amyloid Detection. In M. M. P. M. FASN, A. D. M.D, and G. A. H. M.D, editors, *Amyloid and Related Disorders*, Current Clinical Pathology, pages 187–189. Humana Press, 2012.
- [146] R. Khurana, C. Coleman, C. Ionescu-Zanetti, S. A. Carter, V. Krishna, R. K. Grover, R. Roy, and S. Singh. Mechanism of thioflavin T binding to amyloid fibrils. *Journal of Structural Biology*, 151(3):229–238, September 2005.
- [147] M. Groenning. Binding mode of Thioflavin T and other molecular probes in the context of amyloid fibrils—current status. *Journal of Chemical Biology*, 3(1):1–18, August 2009.

- [148] A. N. Murray, F. L. Palhano, J. Bieschke, and J. W. Kelly. Surface adsorption considerations when working with amyloid fibrils in multiwell plates and Eppendorf tubes. Protein Science, 22(11):1531–1541, November 2013.
- [149] Phenylalanine. <https://omlc.org/spectra/PhotochemCAD/html/073.html>.
- [150] T. Canal and N. A. Peppas. Correlation between mesh size and equilibrium degree of swelling of polymeric networks. Journal of Biomedical Materials Research, 23(10):1183–1193, 1989.
- [151] M. B. Mellott, K. Searcy, and M. V. Pishko. Release of protein from highly cross-linked hydrogels of poly(ethylene glycol) diacrylate fabricated by UV polymerization. Biomaterials, 22(9):929–941, May 2001.
- [152] A. Datta. Characterization of polyethylene glycol hydrogels for biomedical applications. LSU Master's Theses, January 2007.

Appendix A

Predicted selectivity of nuclear pore mimics

Nup fragment	Nup concentration	Molecule	MW	Partition coeff.	Diffusion coeff. in gel	Diffusion coeff. free	K_D	D_B	D_B/D_F	S	S with partition coeff.	10x	Notes
Nsp1 (2-601)	3 mM	IBB-MBP-mEGFP-ImpB MBP-mCherry	510 kD 70 kD	100 0.16	0.17 $\mu\text{m}^2/\text{s}$	4.03 $\mu\text{m}^2/\text{s}$	4.8 μM	0.17 $\mu\text{m}^2/\text{s}$	0.04	42	50		[111]
Nup57 (1-223)-Nup49 (1-246)	3.7 mM	IBB-MBP-mECFP-ImpB MBP-mCherry	510 kD 70 kD	400 0.15	0.1 $\mu\text{m}^2/\text{s}$	2.7 $\mu\text{m}^2/\text{s}$	1.4 μM	0.1 $\mu\text{m}^2/\text{s}$	0.04	69	45		[111]
Nup57 (1-223)-Nsp1 (2-601)-Nup49 (1-246)	1.7 mM	IBB-MBP-mEGFP-ImpB MBP-mCherry	510 kD 70 kD	350 0.1	0.24 $\mu\text{m}^2/\text{s}$	4.03 $\mu\text{m}^2/\text{s}$	0.48 μM	0.24 $\mu\text{m}^2/\text{s}$	0.06	38	16		[111]
Nsp1 (2-175)	3.0 mM	IBB-MBP-mEGFP-ImpB MBP-mCherry	510 kD 70 kD	100 3	0.04 $\mu\text{m}^2/\text{s}$	12.1 $\mu\text{m}^2/\text{s}$	90 μM	0.04 $\mu\text{m}^2/\text{s}$	0.003	1.4	4.3		[50]
Nsp1 (2-601)	3.0 mM	IBB-MBP-mEGFP-ImpB MBP-mCherry	510 kD 70 kD	60 0.4	0.22 $\mu\text{m}^2/\text{s}$	6.94 $\mu\text{m}^2/\text{s}$	20 μM	0.22 $\mu\text{m}^2/\text{s}$	0.03	15	40		[50]
Nsp1 (1-601)	2.2 mM	IBB-Redstar-ImpB IBB-Redstar	530 kD 150 kD	1000 0.3	0.1 $\mu\text{m}^2/\text{s}$	0.2 $\mu\text{m}^2/\text{s}$	0.66 μM	0.1 $\mu\text{m}^2/\text{s}$	0.5	230	100		[49]
Nsp1 (1-601)	2.2 mM	GFP-ImpB IBB-Redstar	124 kD 150 kD	100 0.3	0.1-0.2 $\mu\text{m}^2/\text{s}$	0.2 $\mu\text{m}^2/\text{s}$	6.6 μM	0.1-0.2 $\mu\text{m}^2/\text{s}$	0.5-1	210-250	230-240		[49]
Nsp1 (1-601)	2.2 mM	GFP-ImpB acRedStar	124 kD 117 kD	100 0.05	0.1-0.2 $\mu\text{m}^2/\text{s}$	0.2-1 $\mu\text{m}^2/\text{s}$	1.1 μM	0.1-0.2 $\mu\text{m}^2/\text{s}$	0.1-1	94-260	53-130		[49]
P - Nsp1 (274-601) - P *	4.4 mM	IBB-MBP-mEGFP-ImpB IBB-MBP-mEGFP	510 kD 100 kD	7 0.9	2.78 $\mu\text{m}^2/\text{s}$	16.0 $\mu\text{m}^2/\text{s}$	560 μM	2.42 $\mu\text{m}^2/\text{s}$	0.15	5.3	25		[51]

Table A.1: Predicted selectivity of FG Nup hydrogels in previous work. We took partition and diffusion coefficients from tables in references or calculated them using concentration plots. We determined the dissociation constant K_D from the partition coefficient of the binding species (P_B) and non-binding species (P_N) and the Nup concentration N_t using $K_D \approx (P_I/P_B)N_t$. Note that the measured P_B is an underestimate of the true partition coefficient. We estimated the bound diffusion coefficient from the in-gel (effective) diffusion coefficient (D_{eff}) and the probability of the binding species being bound ($p_b \approx 1 - K_D/N_t$) using $D_B = p_b D_{\text{eff}}$ (Sec. 4.3.2). We used the reaction-diffusion equations discussed in Sec. 2.1 to estimate the selectivity. Because partition coefficient estimates were lower bounds, we also calculated selectivity assuming that the reported partition coefficients were 10% of their actual value. P - Nsp1 (274-601) - P * refers to a fusion between Nsp1 (274-601) and a pentameric coiled-coil P which facilitates the aggregation of the Nsp1 domain into hydrogels. See [51].

Appendix B

Protein expression and purification

B.1 Purification of his-tagged protein with metal affinity column

Most proteins used in this work contain a C-terminal 6x histidine tag. These proteins can be purified using a cobalt or nickel affinity column. Proteins purified with this protocol include all Nup variants (FSFG, FG124, etc.), NTF2, mCherry, and GFP. This protocol is designed for the purification of one 0.5-L cell pellet. If running more than one column at once, adjust the total buffer volumes accordingly.

This protocol is used for all Nup variants. For FSFG variants, use the urea concentrations noted in the buffer table. For FG124 purifications, use 7M guanidine hydrochloride in all buffers (including elution) instead of urea. Always make urea and guanidine hydrochloride solutions the same day they will be used. **Do not use urea, guanidine hydrochloride, or other denaturants when purifying ordered proteins.**

To prevent aggregation, BME must be used for any protein that contains two cysteines. **Do not use BME if not necessary; any BME solutions must be disposed of in the hazardous waste container in the fume hood.**

Add the protease inhibitor cocktail (PIC) stock in DMSO immediately before using the buffer. PIC has a lifetime of about 30 minutes in aqueous solution. Store all buffers on ice before use. Incubations should be done at 4°, but the column can be used at room temperature.

Figure B.1: Buffer guide for cobalt or nickel affinity column purifications.

Buffer	Use (and volume)	Composition
Lysis Buffer	for cell lysis (15 mL)	Buffer of choice 1x (15** mL) 1:1000 PIC (15uL) (8M Urea) (7.2 g) (3mM BME) (3 uL)
Wash I	for wash I (20 mL)	Buffer of choice 1x (20** mL) 1:1000 PIC (20uL) (3M Urea) (4 g) (3mM BME) (4uL)
Wash II *the imidazole is optional; can be useful for removing junk bound to column	for wash II (20 mL)	Buffer of choice 1x (20** mL) 1:1000 PIC (20 uL) (10mM Imidazole) (.013 g) (3mM BME) (4uL)
Elutions	20 mL total	Buffer of choice 1x (20** mL) 1:1000 PIC (20uL) 250mM Imidazole (.32 g) (3mM BME) (4uL)
Handy Molecular Weights	Imidazole: 68.08 g/mol Urea: 60.06 g/mol BME: 14.3 M GuHCl: 95.53 g/mol	**Bring up to volume with buffer. Will not need full 20- <u>25mL</u> if using urea

- (1) Remove the periplasmic matrix, if not already done (Sec. B.2).
- (2) Lyse the cells. Add 15 mL of lysis buffer to thawed 0.5-L pellet. Resuspend pellet by pipetting up and down or vortexing and then lyse by sonicating. Keep solution on ice. lookup: sonicator brand. Sonicate for at least two minutes total, in 30s-on, 60s-off pulses. Power delivered to sample should be at least 20 W. Centrifuge resulting lysate for about 15 mins on top speed of either floor centrifuge to pellet cellular debris.
- (3) Prepare the metal-affinity column. Gently resuspend the resin into a slurry by slowly turning the bottle. The beads will be crushed if shaken vigorously. Into a disposable plastic column, pipette enough slurry to contain 3.5-4 mL of beads once the storage buffer has drained out (typically 6-8 mL of slurry, if beads and buffer are stored in a one-to-one mixture).
Equilibrate the column by running 5-10x the bed volume (25-50 mL) of buffer through the column. Do not let the column run dry at any point in the purification.
- (4) Add supernatant to column and nutate for one hour at 4°C.
- (5) Drain the column. Add wash I buffer and nutate at 4°C for 10 minutes.
- (6) Drain the column. Add Wash II buffer, nutate at 4°C for 10 minutes, and drain.
- (7) Elute and collect the protein. Three elution methods can be used:
 - (a) *Fractional elution:* Prepare a row of eppendorfs. Add 5-10 mL elution buffer to open column and catch the draining liquid in fractions with 0.5-1.0 mL (8-16 drops) per eppendorf. Do not let the column dry. After all elutions are completed, use the Bradford test to pool the fractions with similar protein concentrations. **The Bradford test is unreliable for Nup variants and batch elution should be used.** Fractional elution gives the highest protein concentration and should be used where possible.

- (b) *Batch elution:* Add a bed volume of elution buffer to column and let drain to remove waste buffer from column. Watch resin color change carefully so as not to lose protein. Add 3-5 mL of elution buffer and collect flow-through.
- (c) *Nutated elution:* Add 5-10 mL of elution buffer to sealed column and nutate for 10-30 minutes. Collect flow-through.

Early elutions should be fractional or batch elutions.

9) Clean and store the column. Run 5 bed volumes of MES (lookup: precise components) through the column, then 5 bed volumes DI water. Run about 20 mL MES buffer through the column, then 20 mL DI water. Store 1:1 in 20% ethanol.

B.2 Periplasmic matrix removal (PPMR)

The periplasmic matrix (PPM) contains proteases and debris that binds to metal affinity columns. Removing the PPM before protein purification significantly increase the yield of his-tagged disordered proteins.

Note: Keep both solutions on ice. Resuspension of pellets should be done by gently pipetting up and down and swirling the tubes. Do not vortex to resuspend. Rough treatment of the cells may lyse them.

- (1) Spin down cell culture at 4000g (Sorvall centrifuge, GSA rotor) for 10 minutes at 4°C.
- (2) Resuspend pellets in at least 50 mL cold SHE buffer (20% Sucrose, 50mM HEPES, 1mM EDTA pH 7.9) per liter of culture. Keep tubes on ice.
- (3) Spin down for 10 minutes at 5000 rpm at 4°C.
- (4) Resuspend pellets in at least 50 mL cold 5mM MgSO₄ per liter of culture.
- (5) Incubate tubes on ice for 10 minutes.
- (6) Spin down for 10 minutes at 5000 rpm at 4°C.

- (7) Proceed to purification or flash-freeze tubes in liquid nitrogen and store in ultra-low freezer.

B.3 Lyophilization

Lyophilization refers to freeze-drying proteins. It's a good way to store a known mass of protein before resuspension in hydrogel precursor solution. All lyophilization in this work was done using a Labconco freeze dry system. Lyophilization concentrates any salts in the sample buffer. Therefore, whenever possible, a decomposing buffer should be used. A 25 mM ammonium bicarbonate buffer was used for all lyophilized Nup variants. This buffer decomposes into carbon dioxide, ammonia, and water when lyophilized or above 36°C.

- (1) Dialyze sample into 25 mM ammonium bicarbonate if possible.
- (2) Perform a BCA to quantify the protein concentration in the sample. Prepare eppendorf aliquots that contain the desired mass of protein (usually 100 or 200 µg).
- (3) Cover the aliquots with parafilm and use a needle to punch a hole in the covering.
- (4) Flash-freeze the aliquots.
- (5) Follow lyophilizer instructions. Keep samples frozen and load as quickly as possible to avoid thawing. Ensure that the vacuum is below 50×10^{-3} mBar.
- (6) Leave aliquots on lyophilizer at least 12 hours.
- (7) Remove aliquots from lyophilizer. Remove parafilm and close eppendorfs. Store with desiccant in ultra-low freezer.

Appendix C

Calculation of PEG hydrogel pore size

The following equation was used to estimate pore size in a 10 wt % PEG hydrogel with 20-kDa 8-armed PEG-norbornene and 1-kDa PEG-dithiol crosslinker [150].

$$\frac{1}{M_c} = \frac{2}{M_n} - \frac{\left(\frac{\bar{v}}{v_1}\right) (\ln(1 - v_{2,s} + v_{2,s} + \chi v_{2,s}^2))}{v_{2,r} \left(\left(\frac{v_{2,s}}{v_{2,r}}\right)^{1/3} - \frac{1}{2} \left(\frac{v_{2,s}}{v_{2,r}}\right) \right)} \quad (\text{C.1})$$

with:

The average molecular weight between crosslinks as M_c .

The average polymer molecular weight before crosslinking $M_n = 20$ kDa.

The specific volume of polymer $\bar{v} = 0.8 \text{ cm}^3/\text{g}$ for 1.5K PEG.

The molar volume of the swelling agent $v_1 = 18 \text{ g/mol}$ for water.

The Flory PEG-water interaction parameter $\chi = 0.4$ [151].

The polymer volume fraction before swelling $v_{2,r} = 0.10$ for a 10 wt % hydrogel.

The polymer volume fraction after swelling $v_{2,s} = (\rho_p(\frac{Q_m}{\rho_s} + \frac{1}{\rho_p}))^{-1}$ [152] with:

The solvent density $\rho_s = 1 \text{ g/cm}^3$ for water.

The polymer density $\rho_p = 1.2 \text{ g/cm}^3$ for 20-kDa PEG (Santa Cruz Biotech).

The mass ratio of solvent to polymer $Q_m = 9$.

This calculation gives me $M_c \approx 210$ Da as the average molecular weight between crosslinks.

The mesh size ξ can be estimated using [150]

$$\xi = v_{2,s}^{-1/3} \ell \left(\frac{2M_c}{M_r} \right)^{1/2} c_n^{1/2} \quad (\text{C.2})$$

with:

The carbon-carbon bond length $\ell = 1.54 \text{ \AA}$.

The molecular weight of the repeating polymer unit $M_r = 67 \text{ Da}$ for PEG.

The “characteristic ratio” for PEG $c_n \approx 4$.

The result is an estimated mesh size on the order of 1 nm.

Appendix D

Bis-labeling Nup fragments for incorporation into acrylamide hydrogels

Before FSFG-cys or any other cys-labeled Nup variant can be tethered to an acrylamide hydrogel, it needs to be labeled with bisacrylamide or PEG-DA. This protocol describes the labeling procedure for either chemical group. The cysteines must be fully reduced for the labeling to occur. No BME, TCEP, or other reducing agent can be present in the reaction mixture. FSFG and other disordered peptides form disulfide bonds within minutes of being removed from reducing agents, so begin the reaction as quickly as possible after reducing. This protocol was developed with the help of Benjamin Fairbanks. Following labeling, the extent of labeling can be quantified using an Ellman's reagent assay.

D.1 Bis-labeling reaction protocol

- (1) Begin with a stock of at least 1 mg/mL FSFG with a terminal cysteine in PBS pH 7.8. Typical reactions use 1 mL of approximately 2 mg/mL FSFG.
- (2) Equilibrate an equal amount of immobilized TCEP resin slurry in a disposable 5-mL column which can be spun in a conical tube. Refer to Thermo-Pierce product reference sheet for resin volume and nutation time if necessary. Equilibrate with 20-30 bed volumes of PBS pH 7.8 using gravity, then spin at 161g for 10 s to remove remaining buffer.
- (3) Immediately add the FSFG stock and nutate at 4°C for 1 hour.

- (4) Prepare a conical tube with 40 μL of triethanolamine (TEA, in fume hood) and 50 μL 2% bisacrylamide solution. This will lead to a 10-fold molar excess of bisacrylamide over protein and 300 mM TEA in the final reaction mixture. Place column in conical tube and spin down 1000 rpm for 1 minute.
- (5) Immediately vortex thoroughly. Nutate at room temperature for 30 minutes.
- (6) Dialyze into 25 mM ammonium bicarbonate buffer to remove excess bisacrylamide and prepare for lyophilizing.
- (7) Perform a BCA to quantify protein concentration. Prepare 100 or 200 μg aliquots, freeze, and lyophilize. Store lyophilized protein with a desiccant in ultra-low freezer.

D.2 Ellman's reagent assay protocol

This protocol was taken from Thermo-Fisher's protocol and modified for a microwell plate. Due to the rapid disulfide bond formation of FSFG, the reactants must be mixed very rapidly once reducing agent is removed.

- (1) Equilibrate 80 μL TCEP resin slurry in each of two disposable 1-mL spin columns which can be spun in an eppendorf centrifuge. Refer to Thermo-Pierce product reference sheet for resin volume and nutation time if necessary. Equilibrate with 20-30 bed volumes of PBS pH 7.8 using gravity, then spin at 2300g for 10 s to remove remaining buffer.
- (2) Add 80 μL of bis-labeled FSFG in 25 mM ammonium bicarbonate to one column and a known concentration of unlabeled FSFG cys (as a control) in 25 mM ammonium bicarbonate to the other. Nutate for two hours.
- (3) While incubation proceeds, prepare the reaction buffer (0.1 M sodium phosphate buffer pH 8.0 with 1 mM EDTA) and the Ellman's reagent solution (ERS, 4 mg/mL Ellman's reagent in reaction buffer).

- (4) Prepare a 96-well plate with wells containing 1.8 μM ERS and 29.5 μM reaction buffer. Prepare wells for the FSFG-bis and FSFG cys samples but do not add the protein until everything has been prepared. Prepare a well containing ERS, reaction buffer, and 68 μL of 25 mM ammonium bicarbonate buffer. Finally, prepare a well containing ERS, reaction buffer, and 68 μL of unlabeled FSFG cys of a known concentration that has not been reduced.
- (5) Spin down both columns of TCEP solution 2300g for 30 s in an eppendorf centrifuge and collect the flow-through. Very rapidly, add 68 μL of flow-through to the appropriate wells and mix by pipetting up and down.
- (6) Incubate plate at room temperature for 15 minutes.
- (7) Measure the absorbance at 412 nm using a plate reader.
- (8) Calculate labeling efficiency. Use the buffer well's absorbance to blank the absorbance of the reduced FSFG cys sample and the labeled FSFG sample. Divide the blanked absorbance of the labeled sample by that of the reduced FSFG cys sample and subtract the resulting ratio from 1. The unreduced FSFG sample is not directly used but is a good check on the results.

Appendix E

Hydrogel precursor solutions

This appendix contains details of hydrogel precursor solutions. Lyophilized protein should be resuspended in the buffer component of the precursor solution and incubated at room temperature for at least 20 minutes before adding the other components. No-Nup control gels simply omit the protein. Precursor solutions must be degassed for 10 minutes and promptly polymerized. All solutions containing photoinitiator must be protected from light at all times. Mix under red light only. Prepare precursor solutions immediately before use.

E.1 PEG hydrogel precursor recipes

All PEG hydrogels were 10 wt % PEG with and 0.5 thiol-ene ratio. For more accurate pipetting, stock solutions were designed to be combined in equal volumes.

Table E.1: PEG hydrogel precursor stocks

Component	Concentration	Buffer
20-kDa PEG-norbornene	438 $\mu\text{g}/\mu\text{L}$	Water
1-kDa PEG-dithiol crosslinker	45 $\mu\text{g}/\mu\text{L}$	Water
8-kDa PEG-dithiol crosslinker	360 $\mu\text{g}/\mu\text{L}$	Water
Irgacure 2959	2 mM	Water
LAP	2 mM	Water
TCEP	4 mM	4x PTB

E.2 Acrylamide hydrogel precursor recipes

The monomer and crosslinker were bought premixed from BioRad (acrylamide/bisacrylamide 30% 29:1) but potentially could be prepared in different ratios and mixed separately. Any additional components, such as dextran or photoinhibitor, should be made into a stock with PTB and used instead of the buffer component in the recipe. Acrylamide hydrogels were mostly crosslinked with LAP photoinitiator, but sometimes with the APS/TEMED chemical crosslinking system. Results of several APS/TEMED concentrations in a 6% acrylamide precursor solution are shown in Table E.5.

Table E.2: Sample precursor soution recipe (10 wt % PEG, 10 mg/mL nominal Nup concentration)

Stock	Amount
20-kDa PEG-norbornene	2.5 μ L
1-kDa PEG-dithiol crosslinker	2.5 μ L
Irgacure 2959	2.5 μ L
TCEP in 4x PTB	2.5 μ L
Lyophilized FSFG cys	100 μ g

Table E.3: Acrylamide hydrogel precursor stocks

Component	Concentration	Buffer
Acrylamide monomer	30%	Premixed
Bisacrylamide crosslinker	1%	Premixed
LAP	20 mM	Water
APS	10% w/v	PTB
TEMED	1% w/v	PTB
PTB buffer	1x	PTB

Table E.4: Sample precursor soution recipe (6% final acrylamide concentration)

Stock	Amount
Premixed acrylamide/bis	2 μ L
LAP	1 μ L
PTB	7 μ L
Lyophilized FSFG cys	100 μ g

Table E.5: APS/TEMED chemical crosslinking tests

APS concentration	TEMED concentration	Degas time (min)	Results
1%	0.5%	0	Gelled in under 10 s.
0.1%	0.5%	0	Gelled in 5 minutes.
0.1%	0.1%	5	Gelled in 5 minutes (while degassing).
0.1%	0.1%	0	Gelled in 10 minutes.
0.1%	0.05%	0	Did not gel.
0.1%	0.05%	5	Gelled in 10 minutes.

Appendix F

Protein and peptide sequences

Table F.1: FG Nup fragments

Description	Notes	Sequence
FSFG his	('FSFG concat-1')	MGTSATSKPAFSFGAKSDENKAGATSKPA FSFGAKPEEKDDNSSKPAFSFGAKSN EDKQDGTAKPASFSGAKPAEKNNNET SKPAFSFGAKSDEKKDGDASKPAFSF GAKPDENKASATSKPASHHHHHH
cys FSFG his		MGCTSATSKPAFSFGAKSDENKAGATSKPA FSFGAKPEEKDDNSSKPAFSFGAKSNED KQDGTAKPASFSGAKPAEKNNNETSKPA FSFGAKSDEKKDGDASKPAFSFGAKPDEN KASATSKPASHHHHHH
cys FSFG cys his	Aggregates unless kept in reducing agent.	MGCTSATSKPAFSFGAKSDENKAGATSKPA FSFGAKPEEKDDNSSKPAFSFGAKSNED KQDGTAKPASFSGAKPAEKNNNETSKPA FSFGAKSDEKKDGDASKPAFSFGAKPDEN KACATSKPASHHHHHH
ybbR FSFG cys his	Most often used for hydrogel experiments; ybbR tag is intended for site-specific labeling but not used in the hydrogel experiments.	MGDSLEFIASKLATSATSKPAFSFGAKSDEN KAGATSKPAFSFGAKPEEKDDNSSKPA FSFGAKSNEDKQDGTAKPASFSGAK PAEKNNNETSKPAFSFGAKSDEKKDGDAS KPAFSFGAKPDENKACATSKPASHHHHHH
ybbR FSFG concat- 2 cys his		MGDSLEFIASKLATSATSKPAFSFGAKSDEN KAGATSKPAFSFGAKPEEKDDNSSKPA FSFGAKSNEDKQDGTAKPASF FGAKPAEKNNNETSKPAFSFGA KSDEKKDGDASKPAFSFGAKP DENKASATSKPASATSKPAFS FGAKSDENKAGATSKPAFSF GAKPEEKDDNSSKPAFSFGAKSNED KQDGTAKPASFSGAKPAEKNNNET SKPAFSFGAKSDEKKDGDASKPAFSF GAKPDENKACATSKPASHHHHHH

Table F.2: FG Nup fragments, continued.

Description	Notes	Sequence
ybbR FSFG concat- 3 cys his	Did not express well in my hands.	MGDSLEFIASKLATSATSKPAFSFGAKSDEN KAGATSKPAFSFGAKPEEKKK DDNSSKPAFSFGAKSNEDKQDGTA PAFSFGAKPAEKNNNETSKPAFSF GAKSDEKKDGDASKPAFSFGAKPD ENKASATSKPASATSKPAFSFGAKS DENKAGATSKPAFSFGAKPEEKKDDN SSKPAFSFGAKSNEDKQDGTA GAKPAEKNNNETSKPAFSFGAKSDEKK DGDASKPAFSFGAKPDENKASATSKPA SATSKPAFSFGAKSDENKAGATSKPAFS FGAKPEEKKDDNSSKPAFSFGAKSNEDKQ DGTAKPAFSFGAKPAEKNNNETSKPAF SFGAKSDEKKDGDASKPAFSFGAKPDEN KACATSKPASHHHHH
ybbR SSSG cys his	Nonbinding control.	MGDSLEFIASKLATSATSKPASSSGAKSDEN KAGATSKPASSSGAKPEEKKDDNSSKPA SSSGAKSNEDKQDGTA PAEKNNNETSKPASSSGAKSDEKKDGDAS KPASSSGAKPDENKACATSKPASLEHHH HHH
FG124 his	Aggregates unless kept in denaturant	MAPNNTNNANSSITPAFGSNNTGN SNPTSNVFGSNNSTTNTFGSNSAGT SLFGSSSAQQTKSNGTAGGNT FGSSSLFNNNSTNSNTTKPAFGLNFGGGN NTTPSSTGNANTSNNLFGATASHHHHHH
cys FG124 his	Aggregates unless kept in denaturant.	MGCTSAPNNTNNANSSITPAFGSNNTGN TAFGNSNPTSNVFGSNNSTTNT FGSNSAGTSLFGSSAQQTKSNGTAGGNT FGSSSLFNNNSTNSNTTKPAFGLNFGGGN NTTPSSTGNANTSNNLFGATASHMHHH HHH

Table F.3: Other sequences

Description	Notes	Sequence
NTF2 his	Wild-type yeast NTF2.	MALDFNTLAQNFTQFYNNQFDTDRSQLGN LYRNESMLTFETSQLQGAKDIVEKLVS LPFQKVQHRITTLDAQPASPNGDVLVMIT GDLLIDEEQNPQRFSQVFHLIPDGN SYYVFNDIFRLNYSAAHHHHH
Pho4	Nuclear localization sequence.	KVDKLGGSGSANKVTKNKSNSSPYLNKRR GKPGPDSLE
Spo12	Nuclear localization sequence.	KVDKLGGSGKSTSNLKSSHTTSNLVKKT FKRDLLKQDPKRKLQLQQRFASPTDR LVSPCSLKLE

Appendix G

Dye-labeling protocols

The following protocols were used to label proteins with various fluorophores. Dyes should always be stored in the ultra-low freezer in anhydrous DMSO. Labeled proteins should be aliquoted within 24 hours of labeling and stored in the ultra-low freezer until just before use. These protocols were adapted from Thermo-Fisher amine and cysteine labeling protocols with help from Eric Verbeke and Annette Erbse.

If better efficiency is needed, the next improvement would be to carry out the protocols in a glove bag under nitrogen.

G.1 Labeling NTF2 with fluorescein-NHS

- (1) Resuspend lyophilized fluorescein-NHS at 100 mg/mL in anhydrous DMSO in the dark-room. Discard the remaining DMSO aliquot. Make 100- μ L aliquots of dye solution. Store with desiccant in ultra-low freezer, protected from light.
- (2) Mix NTF2 in PTB pH 7.0 and 100 mg/mL fluorescein-NHS in DMSO with around 15-fold molar excess dye. Several other buffers can be used as well (see Thermo protocol). A typical labeling reaction used 0.5 mL of 16 mg/mL NTF2 and 18.6 μ L dye stock mixed in an Eppendorf with an Eppendorf stir bar.
- (3) Incubate mixture, stirring, protected from light, at room temperature for one hour.

- (4) Equilibrate TALON cobalt resin with PTB in a column that can be spun in a centrifuge. TALON resin has a stated capacity of 5-15 mL protein per mL resin. Using significantly more than needed can lead to nonspecific binding of free dye. A typical reaction required 1.6 mL of the resin slurry. Equilibrate with at least 10 bed volumes PTB.
- (5) Cap column and add reaction mixture. Nutate at 4°C for one hour, protected from light.
- (6) Allow column to drain and wash with approximately 100 bed volumes of PTB, protected from light as best as possible. Occasionally cap column and resuspend resin to remove free dye from column cap and sides. Test flow-through using UV light to ensure that no dye is visible by the end of the wash. Resin should still be bright yellow.
- (7) Spin column at 160g for one minute to remove remaining wash buffer. Immediately cap and elute with 1 mL of 300 mM imidazole in PTB. Nutate 4°C for half an hour and collect elution. Resin should return to pink.
- (8) Dialyze elution against PTB to remove imidazole. No more than 24 hours after labeling, aliquot and freeze labeled NTF2.
- (9) Run a sample of labeled NTF2 on a native PAGE gel along with a sample of fluorescein-NHS. Use the Typhoon to compare the concentration of free dye to labeled protein in the protein sample.

G.2 Labeling NTF2 with Alexa Fluor 488 - SDP or FSFG with Alexa Fluor 647 - SDP

- (1) Resuspend lyophilized Alexa Fluor 488 at 10 mg/mL in anhydrous DMSO in the darkroom. Discard the remaining DMSO aliquot. Make 10- μ L aliquots of dye solution. Store with desiccant in ultra-low freezer, protected from light.
- (2) Mix NTF2 in 0.1 M sodium bicarbonate buffer and 10 mg/mL fluorescein-NHS in DMSO. A typical labeling reaction used 200 μ L of 16 mg/mL NTF2 and 20 μ L dye stock mixed in

an Eppendorf with an Eppendorf stir bar.

- (3) Incubate mixture, stirring, protected from light, at room temperature for one hour.
- (4) Equilibrate TALON cobalt resin with PTB in a column that can be spun in a centrifuge. TALON resin has a stated capacity of 5-15 mL protein per mL resin. Using significantly more than needed can lead to nonspecific binding of free dye. Equilibrate with at least 10 bed volumes PTB.
- (5) Cap column and add reaction mixture. Nute at 4°C for one hour, protected from light.
- (6) Allow column to drain and wash with approximately 100 bed volumes of PTB, protected from light as best as possible. Occasionally cap column and resuspend resin to remove free dye from column cap and sides. Test flow-through using UV light to ensure that no dye is visible by the end of the wash. Resin should still be bright yellow.
- (7) Spin column 2300g for 20 s to remove remaining wash buffer. Immediately cap and elute with 300 μ L of 500 mM imidazole in PTB. Nute at 4°C for half an hour and collect elution. Resin should return to pink.
- (8) Dialyze elution against PTB to remove imidazole. No more than 24 hours after labeling, aliquot and freeze labeled NTF2.
- (9) Run a sample of labeled NTF2 on a native PAGE gel along with a sample of fluorescein-NHS. Use the Typhoon to compare the concentration of free dye to labeled protein in the protein sample.

G.3 Labeling NTF2-cys with Alexa Fluor 488 - maleimide

- (1) Resuspend lyophilized Alexa Fluor 488 at 10 mg/mL in anhydrous DMSO in the darkroom. Discard the remaining DMSO aliquot. Make 10- μ L aliquots of dye solution. Store with desiccant in ultra-low freezer, protected from light.

- (2) Mix protein in PTB pH 7.0 and 50 μ M TCEP (with no other reducing agent present) and 10 mg/mL dye in DMSO. Typical amounts were 50 μ L of 100 μ M NTF2-cys into 50 μ L dye stock.
- (3) Incubate mixture, stirring, protected from light, at room temperature for two hours.
- (4) Equilibrate TALON cobalt resin with PTB in a column that can be spun in a centrifuge. TALON resin has a stated capacity of 5-15 mL protein per mL resin. Using significantly more than needed can lead to nonspecific binding of free dye. Equilibrate with at least 10 bed volumes PTB.
- (5) Cap column and add reaction mixture. Nutate at 4°C for one hour, protected from light.
- (6) Allow column to drain and wash with approximately 100 bed volumes of PTB, protected from light as best as possible. Occasionally cap column and resuspend resin to remove free dye from column cap and sides. Test flow-through using UV light to ensure that no dye is visible by the end of the wash. Resin should still be bright yellow.
- (7) Spin column 2300g for 20 s to remove remaining wash buffer. Immediately cap and elute with 300 μ L of 500 mM imidazole in PTB. Nutate 4°C for half an hour and collect elution. Resin should return to pink.
- (8) Dialyze elution against PTB to remove imidazole. No more than 24 hours after labeling, aliquot and freeze labeled NTF2.
- (9) Run a sample of labeled NTF2 on a native PAGE gel along with a sample of fluorescein-NHS. Use the Typhoon to compare the concentration of free dye to labeled protein in the protein sample.

Appendix H

Hydrogel nuclear pore mimic dataset

This appendix gives the parameters calculated for each hydrogel in the FRAP dataset, organized by FSFG condition. The predicted values for bound diffusion constant D_B and bound to free diffusion ratio D_B/D_F assume that the only mechanism of bound diffusion is tethered diffusion, so that

$$\frac{D_B}{D_F} = \frac{L_c \ell_p k_{\text{off}}}{L_c \ell_p k_{\text{off}} + 3D_F}$$

The parameters used are given in Fig. H.1. The K_D values are average values from [27]. The on-rate k_{on} is assumed to be diffusion-limited. Diffusion constants have units of $\mu\text{m}^2/\text{s}$. Partition coefficients (γ) and fraction of NTF2 bound (p_B) are unitless.

	FSFG concat-1	FSFG concat-2
L_c (aa)	124	248
L_c (m)	4.96E-08	9.92E-08
Length per aa (m)	4.00E-10	4.00E-10
ℓ_p (m)	1.00E-09	1.00E-09
K_D (M)	0.000545	0.000395
k_{on} ($\text{M}^{-1} \text{s}^{-1}$)	1.00E+09	1.00E+09
k_{off} (s^{-1})	5.45E+05	3.95E+05

Figure H.1: Parameters used to predict the bound diffusion constant for NTF2-F in FSFG hydrogels. Binding data is from [27].

Figure H.2: Measured and calculated values for no-Nup hydrogels.

	Dataset index	Experiment ID	D _{obs} NTF2	D _{obs} mCherry	γ NTF2	γ mCherry	p _B
	1	'19-1-3_1'	41.6	26.7	0.64	0.52	0.19
	4	'19-2-6_1'	68.7	71.2	0.57	0.52	0.10
	7	'19-2-6_7'	25.3	26.4	0.52	0.52	-0.01
	10	'19-2-6_13'	177.3	126.3	0.60	0.69	-0.16
	13	'19-2-6_19'	72.0	71.5	0.66	0.61	0.07
	18	'19-2-12_7'	33.1	25.8	0.44	0.47	-0.08
	20	'19-2-12_11'	100.1	68.1	0.42	0.49	-0.16
	24	'19-2-15_1'	26.8	26.5	0.21	0.30	-0.45
	25	'19-2-15_7'	31.2	27.6	0.40	0.42	-0.05
	26	'19-2-15_13'	74.8	61.4	0.48	0.45	0.06
	28	'19-2-15_19'	10.9	15.2	0.42	0.42	-0.01
	30	'19-2-19_1'	37.8	32.0	0.53	0.52	0.02
	31	'19-2-19_7'	18.3	15.6	0.39	0.42	-0.07
	33	'19-2-19_19'	40.8	44.2	0.44	0.41	0.06
	41	'19-2-21_19'	82.9	57.9	0.45	0.47	-0.04
Mean			56.10	46.44	0.48	0.48	-0.04
Standard deviation			42.52	29.94	0.11	0.09	0.15
Standard error of the mean			11.36	8.00	0.03	0.02	0.04

Figure H.3: Measured and calculated values for FSFG concat-1 hydrogels, nominally containing 10 mg/mL FSFG.

	Dataset index	Experiment ID	D _{obs} NTF2	D _{obs} mCherry	γ NTF2	γ mCherry	p _B	D _B	using ITC data	Predicted D _{B/D_F}	Predicted D _B
	2	'19-1-3_3'	29.0	49.1	2.06	0.54	0.74	21.84	0.16	7.61	
	5	'19-2-6_3'	7.2	41.9	1.89	0.46	0.76	-3.91	0.18	7.41	
	8	'19-2-6_9'	13.9	22.9	1.31	0.54	0.59	7.71	0.28	6.47	
	11	'19-2-6_15'	13.4	36.1	1.53	0.42	0.72	4.76	0.20	7.21	
	14	'19-2-6_21'	20.2	46.0	1.77	0.41	0.77	12.48	0.16	7.54	
	16	'19-2-12_3'	12.5	22.3	1.77	0.56	0.69	7.95	0.29	6.42	
	19	'19-2-12_9'	10.9	41.4	1.63	0.47	0.71	-1.51	0.18	7.40	
	21	'19-2-12_13'	42.4	70.4	1.03	0.63	0.38	-2.78	0.11	7.99	
	27	'19-2-15_15'	10.0	19.4	1.65	0.36	0.78	7.41	0.32	6.16	
	32	'19-2-19_15'	4.8	35.9	2.20	0.39	0.82	-1.82	0.20	7.20	
	34	'19-2-19_21'	7.4	20.2	1.84	0.36	0.81	4.28	0.31	6.23	
	39	'19-2-21_15'	11.0	10.9	2.95	0.46	0.84	10.96	0.45	4.93	
Mean			15.23	34.71	1.80	0.47	0.72	5.62	0.24	6.88	
Standard deviation			10.71	16.55	0.48	0.09	0.13	7.52	0.10	0.86	
Standard error of the mean			3.23	4.99	0.14	0.03	0.04	2.27	0.03	0.26	

Figure H.4: Measured and calculated values for FSFG concat-2 hydrogels.

	Dataset index	Experiment ID	D _{obs} NTF2	D _{obs} mCherry	γ NTF2	γ mCherry	p _B	D _B	using ITC data	
									Predicted D _{B/D_F}	Predicted D _B
	6	'19-2-6_5'	12.78184	44.56024563	3.23	0.70	0.78	4.04	0.23	10.10
	9	'19-2-6_11'	10.307	43.18354162	2.82	0.66	0.77	0.24	0.23	10.03
	12	'19-2-6_17'	8.353138	30.91040114	3.24	0.50	0.85	4.22	0.30	9.18
	17	'19-2-12_5'	9.398679	42.56939841	4.41	0.67	0.85	3.49	0.23	9.99
	22	'19-2-12_15'	26.73285	39.71193071	2.64	0.68	0.74	22.25	0.25	9.83
	23	'19-2-12_17'	16.29925	53.36041486	2.89	0.73	0.75	3.88	0.20	10.49
	35	'19-2-19_23'	5.88424	34.98831302	2.78	0.57	0.80	-1.54	0.27	9.51
	37	'19-2-21_11'	27.91552	29.00498627	3.49	0.41	0.88	27.77	0.31	9.01
	40	'19-2-21_17'	2.634705	18.14683742	4.72	0.55	0.88	0.61	0.42	7.59
	43	'19-2-21_23'	0.534426	17.81107527	5.02	0.63	0.87	-1.95	0.42	7.54
	Mean				12.08	35.42	3.52	0.61	0.82	6.30
	Standard deviation				9.24	11.57	0.87	0.10	0.06	10.20
	Standard error of the mean				3.08	3.86	0.29	0.03	0.02	3.40
									0.03	0.34

Appendix I

FG124 aggregation condition p-values

Table I.1: Aggregation rate k p-values for all crowding agents, two-tailed t-test.

	10 mg/mL cell lysate	19% w/v serine	13% PEG	13% PVP
No crowder	0.031	1.2×10^{-6}	6.6×10^{-4}	0.41
10 mg/mL cell lysate	N/A	0.44	0.0010	0.022
19% w/v serine	N/A	N/A	4.4×10^{-9}	2.2×10^{-6}
13% PEG	N/A	N/A	N/A	0.019

Table I.2: Lag time T_ℓ p-values for all crowding agents, two-tailed t-test.

	10 mg/mL cell lysate	19% w/v serine	13% PEG	13% PVP
No crowder	5.4×10^{-6}	1.4×10^{-8}	0.77	0.0012
10 mg/mL cell lysate	N/A	0.0051	0.00041	0.0060
19% w/v serine	N/A	N/A	0.0052	0.53
13% PEG	N/A	N/A	N/A	0.039

Table I.3: Aggregation rate k p-values for PEG (% w/v) , two-tailed t-test.

	20%	13%	5%	0%
25%	0.0063	0.6167	0.0007	0.8344
20%	N/A	0.0131	0.7539	0.0815
13%	N/A	N/A	0.1196	0.6508
5%	N/A	N/A	N/A	0.0681

Table I.4: Lag time T_ℓ p-values for PEG (% w/v) , two-tailed t-test.

	20%	13%	5%	0%
25%	0.0071	0.0412	0.7726	0.0221
20%	N/A	0.5377	0.0206	0.1012
13%	N/A	N/A	0.1322	0.0927
5%	N/A	N/A	N/A	0.2833

Table I.5: Aggregation rate k p-values for PVP (% w/v) , two-tailed t-test.

	20%	13%	5%	0%
25%	0.8521	0.1327	0.4104	0.1880
20%	N/A	0.6607	0.6530	0.6815
13%	N/A	N/A	0.5991	0.8283
5%	N/A	N/A	N/A	0.6902

Table I.6: Lag time T_ℓ p-values for PVP (% w/v) , two-tailed t-test.

	20%	13%	5%	0%
25%	4.7×10^{-5}	0.0133	0.0012	0.0628
20%	N/A	0.2586	8.6×10^{-6}	0.0272
13%	N/A	N/A	0.0018	0.0709
5%	N/A	N/A	N/A	0.6774